

Die approbierte Originalversion dieser
Dissertation ist in der Hauptbibliothek der
Technischen Universität Wien aufgestellt und
zugänglich.

<http://www.ub.tuwien.ac.at>



The approved original version of this thesis is
available at the main library of the Vienna
University of Technology.

<http://www.ub.tuwien.ac.at/eng>



TECHNISCHE
UNIVERSITÄT
WIEN

VIENNA
UNIVERSITY OF
TECHNOLOGY

DISSERTATION

Double and Triple Entanglement in a Single Neutron System

ausgeführt zum Zwecke der Erlangung des akademischen Grades eines
Doktors der technischen Wissenschaften unter der Leitung von

Associate Prof. Dipl.-Ing. Dr. Yuji Hasegawa
E141 - Atominstitut der Österreichischen Universitäten

eingereicht an der Technischen Universität Wien
bei der Fakultät für Physik

von

Dipl.-Ing. Daniel Erdósi
Matrikelnummer: 9726165
Probusg. 5/3, 1190 Wien, Austria

Wien, im Februar 2015

Abstract

Single-neutron interferometry is used in various experiments to study the foundations of quantum mechanics. The drawback of this technique, however, is that the contrast of neutron interferometers is very prone to disturbances, in particular, temperature variations. In order to achieve very low degrading of the contrast, we develop new devices to manipulate the neutron's spin and energy in the interferometer. These devices open the door for quantum state generation with much higher fidelities than it has been possible so far in neutron interferometry. Spin rotators with time-dependent (radio-frequency (RF)) field change both spin and energy. We improve our RF spin-rotators for the interferometer by equipping them with miniature Helmholtz coils, which allows to adjust the energy shift due to each RF coil independently. This is essential for the generation of certain quantum states. This improvement is made possible by a new coil cooling method. Furthermore, we also develop new Larmor precession accelerators and decelerators that do not consume energy and hence do not produce heat at all. We demonstrate two applications of the new spin and energy manipulators by generating bi- and tripartite entanglement between the neutron's spin, energy and path degrees of freedom in the interferometer: we succeed in generating a Bell-like state and GHZ- and W-like states. For Bell state generation we also introduce a convenient spin preparation scheme that uses our Larmor precession manipulator. We achieve a considerably more significant violation of a Bell-like inequality than with the previous method, thus further confirming quantum contextuality. With our RF spin rotators we achieve for the GHZ- and W-like states fidelities between 95 and 99%.

Kurzfassung

Einzelneutroneninterferometrie wird gerne angewendet um die Grundlagen der Quantenmechanik zu studieren. Der Nachteil dieser Technik ist jedoch, dass der Kontrast der Neutroneninterferometer sehr anfällig auf Störungen ist, insbesondere auf Temperaturschwankungen. Um einen viel niedrigeren Kontrastverlust zu erreichen als bisher, entwickeln wir neue Apparate für die Spin- und Energiemanipulation von Neutronen im Interferometer. Diese Apparate ermöglichen die Erzeugung von Quantenzuständen mit deutlich höherer Treue (fidelity) als es bisher in der Neutroneninterferometrie möglich war. Spinrotatoren mit zeitabhängigem (Radiofrequenz (RF)) Feld ändern sowohl den Spin als auch die Energie. Wir verbessern unsere RF-Spinrotatoren für das Interferometer, indem wir sie mit Miniatur-Helmholtzspulen ausstatten, so dass die Energieverschiebungen durch die RF-Spulen voneinander unabhängig eingestellt werden können. Dies ist für die Erzeugung von bestimmten Quantenzuständen unabdingbar. Diese Verbesserung wird durch ein neues Kühlverfahren für die Spulen ermöglicht. Desweiteren entwickeln wir auch neue Larmorpräzessionsbeschleuniger und -verzögerer, die keine Energie verbrauchen und daher überhaupt keine Hitze erzeugen. Wir zeigen zwei Anwendungen der neuen Spin- und Energiemanipulatoren indem wir Zwei- und Dreifachverschränkung zwischen Spin, Energie und Weg des Neutrons im Interferometer erzeugen: die Erzeugung eines Bell-Zustandes und von GHZ- und W-Zuständen gelingt mit Erfolg. Für die Erzeugung des Bell-Zustandes führen wir auch eine passende Methode zur Spinaufbereitung ein, die unseren Larmorpräzessionsmanipulator verwendet. Wir erreichen eine deutlich signifikantere Verletzung einer Bellschen Ungleichung als mit der bisherigen Methode, und damit eine weitere Bestätigung der Quantenkontextualität. Mit unseren RF-Spinrotatoren erzielen wir für die GHZ- und W-Zustände Treuen zwischen 95 und 99%.

Acknowledgement

I would like to express my thanks to everybody who contributed to this work or supported me during my dissertation.

First of all, I want to thank my supervisor Associate Prof. Dipl.-Ing. Dr. Yuji Hasegawa, who gave me the opportunity to work as a PhD-student in the neutron interferometry group of the Atominstitut. I am grateful for his drive and patience in supporting me and for the countless critical and fruitful discussions.

Furthermore, I want to thank Dipl.-Ing. Dr. Stephan Sponar and Dipl.-Ing. Dr. Hartmut Lemmel for their assistance in the preparation of and during the experiments. Without their help this work could not have come to a successful end. Also, I owe thanks to Mag. Dr. Marcus Huber for providing important theoretical insights and his engagement in the publication process of our second experiment. Entitled to my gratitude is also Dipl.-Ing. Dr. Jürgen Klepp for many enjoyable hours and technical discussions during my experiments. Last but not least, my thanks go to Ao. Univ.-Prof. Mag. Dr. Martin Fally for his very thorough final review of this thesis in the role of the second referee.

This work was financially supported by the Austrian Science Fund (FWF), project number P21193.

Contents	
Abstract	i
Kurzfassung	ii
Acknowledgement	iii
1. Preface	1
2. Background of the study	4
2.1. Neutron interferometry	4
2.1.1. Perfect crystal neutron interferometer	4
2.1.2. Dynamical theory of diffraction	7
2.2. Entanglement: theory and experiments	9
2.2.1. Einstein-Podolsky-Rosen (EPR) paradox, entangled states, and joint measurements	9
2.2.2. Bell's inequality	13
2.2.3. Quantum non-locality vs. contextuality	14
2.2.4. Experimental tests	15
3. New neutron optical devices	16
3.1. Manipulation of neutron's $\frac{1}{2}$ -spin	16
3.1.1. Adiabatic and non-adiabatic spin manipulation	16
3.1.2. Radio frequency spin flipper	16
3.2. RF coil equipped with mini guide field for operation in an interferometer	17
3.2.1. Optimization of the miniGF	19
3.2.2. Development of the water box	25
3.3. Larmor accelerators and decelerators for the Interferometer	29
3.3.1. Motivation: generation of a Bell-like state in neutron interferometry	29
3.3.2. Drawback of the previous methods to generate a Bell-like state in neutron interferometry	29
3.3.3. New method to generate a Bell-like state in neutron interferometry	30
3.3.4. Mini guide field (miniature Helmholtz coil)	32
3.3.5. Mu-metal tube	33
3.3.6. Iron rings	42
3.3.7. Iron pole pieces	44

4. Experiment 1: Violation of a Bell-like inequality	47
4.1. Background of the study	47
4.2. Theory	48
4.3. Interferometer experiment to violate a Bell-like inequality	49
4.3.1. Adjustments	52
4.3.2. Measurement and data-analysis	54
5. Experiment 2: Generation of GHZ- and W-like neutron states in interferometry	58
5.1. Background of the study	58
5.2. Theory	58
5.3. Experimental generation of W- and GHZ-like states	60
5.4. Measurement and data-analysis	62
5.5. Relations between the measured contrasts/intensities and the coefficients for the <i>W</i> -state	64
5.5.1. Determination of $ ab $	65
5.5.2. Determination of $ ac $	66
5.5.3. Determination of $ bc $	67
5.5.4. Determination of $ a ^2$	68
5.5.5. Determination of $ b ^2$ and $ c ^2$	68
5.6. Relations between the measured contrasts/intensities and the coefficients for the GHZ-state	69
5.6.1. Determination of $ de $, $ e ^2$, and $ d ^2$	70
5.7. Adjustments of the spin flippers	71
5.8. Results: determination of entanglement witness	74
6. Conclusions and outlook	77
Bibliography	78
Curriculum Vitae	87

1. PREFACE

Quantum mechanics is one of the most successful theories of physics, giving the most accurate description of our world on the microscopic scale. It has continued to provide us with new theoretical and experimental challenges since the beginning of the previous century. As experimental methods and technologies become more and more developed, the often counterintuitive predictions of quantum mechanics become more and more confirmed, keeping physicists attracted to explore the rich variety of possibilities to experimentally verify predictions by the theory and also to pursue the engineering of ambitious practical applications like a quantum computer. With the acceptance of quantum mechanics we have to give up the deterministic world view of classical physics in favor of an approach that allows only probabilistic predictions on the outcome of observations.

Interference experiments play a central role in the research of the fundamentals of quantum mechanics by making the wave nature of matter accessible to observation. In particular we are interested in the Mach-Zehnder type interferometer, which splits a collimated particle beam into two relatively widely separated coherent sub beams, which can be manipulated in several ways. By changing the optical path length of the beams relative to each other, interference effects, more exactly, intensity modulations, can be observed after the beams' coherent recombination. The first such interferometers were designed for light [Zehnder, 1891, Mach, 1892] and the technique was successively implemented for massive particles, e.g., electrons [Marton et al., 1953, Möllenstedt, 1959], neutrons [Rauch et al., 1974], atoms [Berman, 1997], and even molecules [Arndt, 1999], thus demonstrating that also massive particles have wave properties and that the superposition principle applies to them.

Neutron interferometric experiments have been established as an ideal method for quantum mechanical studies with massive particles, and to this day these experiments serve as an elegant way to demonstrate quantum mechanical phenomena. Using interferometry, phenomena due to the neutron's interaction with nuclear forces [Rauch et al., 1974], magnetic forces [Rauch et al., 1975], gravitational potentials [Colella et al., 1975], and electric fields [Cimmino et al., 1989] could be demonstrated. In this work, the neutron's interaction with magnetic fields is exploited. An oscillating magnetic field orthogonal to the guide field may change the neutron's spin and total energy. Applying magnetic fields with different strength or with different oscillation frequencies in the two sub beams of the interferometer, entanglement between the path and spin or between the path, spin, and energy degrees of freedom of the neutron can be achieved, which has been experimentally realized in this study.

Such phenomena as entanglement and non-local correlation predicted by quantum mechanics led Einstein, Podolsky, and Rosen [Einstein et al., 1935] to the view that quantum mechanics does not provide a

complete picture of the phenomena it aims to describe. By assuming local realism they proposed a description from that the so-called hidden variable theories were derived. The mutual incompatibility of quantum mechanics and hidden variable theories, which use the joint assumption of locality and reality, was shown by Bell [Bell, 1964]. Accordingly, hidden variable theories cannot reproduce the predictions of quantum mechanics. Bell proposed inequalities that are obeyed by hidden variable theories but are violated by quantum mechanics, more exactly, a violation of a Bell inequality proves the presence of entanglement, i.e., the non-local or even contextual characteristic of the observed quantum system. Thus a Bell inequality provides a tool to decide on the basis of experiment whether hidden variable theories or quantum mechanics is applicable.

Noncontextuality implies that the value of a dynamical variable is pre-determined and independent of the experimental context, more exactly, of previous and simultaneous measurements of a commuting variable [Bell, 1966, Mermin, 1993]. As such, noncontextuality is a more stringent demand than locality, since it requires commuting observables to be independent of each other even if the events of their measurements are not spacelike separated [Simon et al., 2000]. Accordingly, local hidden variable theories can be considered as a subset of the noncontextual hidden variable theories. A single-neutron system offers a nice possibility to study quantum contextuality, because entanglement occurs between different degrees of freedom of the single neutron, rather than between different (spatially separated) particles.

Single-neutron interferometry [Rauch and Werner, 2000] has already been shown to be a useful tool in generating entanglement between the spinor and spatial part of the neutron's wave function [Hasegawa et al., 2003], in conducting full tomographic measurement of the neutron's entangled state [Hasegawa et al., 2007], and in demonstrating contextuality [Hasegawa et al., 2006, Bartosik et al., 2009]. Also a tripartite (spin-energy-path) entangled state was successively generated to demonstrate a coherent energy manipulation scheme [Sponar et al., 2008] and hereafter some characteristics of so-called Greenberger-Horne-Zeilinger (GHZ) triplets [Hasegawa et al., 2010].

In the first part of this thesis we explain the development of new devices to manipulate the spin and energy of the neutron in the interferometer. Spin flippers with time-dependent field (radio-frequency (RF) coils) change both spin and energy. We improve our RF coils for the interferometer by equipping them with miniature Helmholtz coils, which allows to adjust the energy shift of each RF coil independently. This is essential for the generation of certain quantum states. This improvement is made possible by a new coil cooling system. Furthermore, we also develop new Larmor precession manipulators for the interferometer. Our new devices cause very low degrading of the interferometer contrast compared to previous devices, and thus enable state generation with much higher fidelities than it has been possible so far. The second part of this thesis is about some applications of the newly developed spin manipulators. We generate bi- and

tripartite entanglement in the interferometer, more exactly, a Bell-like state and W- and GHZ-like states. For Bell state generation we apply a new spin preparation scheme together with our Larmor precession manipulator, by which we achieve a considerably more significant violation of a Bell-like inequality than with the previous method, thus further confirming quantum contextuality. With our RF spin flippers we are able to achieve for the W- and GHZ-like states fidelities between 95 and 99%. For the detection of these two states we also employ two distinct nonlinear entanglement witnesses, which are optimally suited to detect GHZ- and W-like entanglement. We also analyze the robustness of these states by controlled decoherence, thus studying the influence of noise.

2. BACKGROUND OF THE STUDY

2.1. Neutron interferometry

As a part of neutron optical research, neutron interferometry has become a powerful tool for fundamental quantum mechanical studies as well as studies of neutron physics [Rauch et al., 1974, Rauch and Werner, 2000]. Our focus is on the Mach-Zehnder type interferometer, which produces spatially widely separated coherent sub beams of matter waves by amplitude division due to dynamical Bragg diffraction. A silicon single-crystal interferometer was initially developed for X-rays [Bonse and Hart, 1965]. For neutrons such an interferometer was first realized in 1974 by Rauch, Treimer, and Bonse [Rauch et al., 1974], who first obtained the resulting interference fringes, thus demonstrating the wave nature of neutrons, at the TRIGA research reactor of the Atominstitut in Vienna. Since then the perfect-crystal interferometer has been established as a standard tool in neutron optics. Several notable experiments to examine fundamental questions of quantum mechanics have been carried out using neutron interferometry, some of them listed here: verification of the 4π -spinor symmetry [Rauch et al., 1975], studies of gravitational effects on the neutron's wave function [Zych et al., 2011] and of spin-superposition [Summhammer et al., 1983, Badurek et al., 1983, Badurek et al., 1986], generation of entanglement between the spin and the spatial degrees of freedom of single particles [Hasegawa et al., 2003], accomplishment of a full state tomography [Hasegawa et al., 2007], and demonstration of quantum contextuality [Hasegawa et al., 2006, Bartosik et al., 2009].

2.1.1. *Perfect crystal neutron interferometer*

A Mach-Zehnder type silicon perfect-crystal neutron interferometer [Rauch et al., 1974, Rauch and Werner, 2000] is an apparatus consisting of a beam splitter, mirrors, and analyzer, which are realized, e.g., by three beam splitter plates (interferometer plates) on a common basis as depicted in Fig. 1. Diffraction of the neutron beam may take place due to the comparable values of the lattice parameter and the wavelength of thermal neutrons.

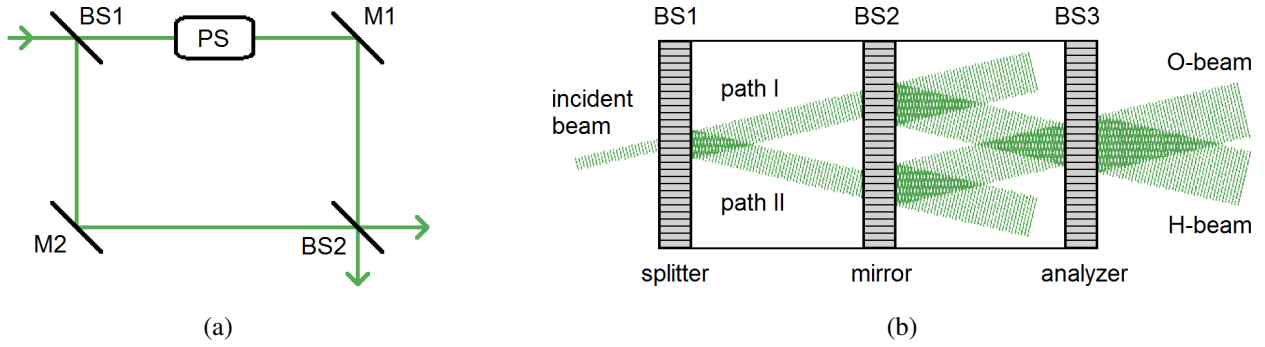
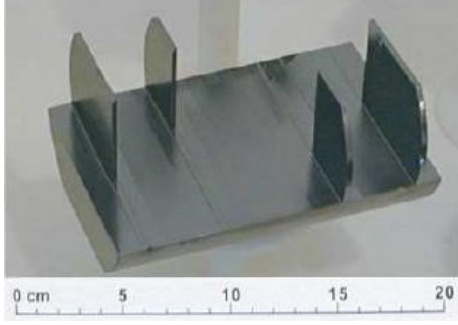
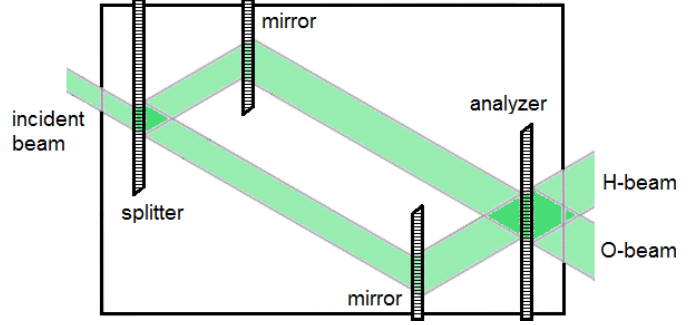


Fig. 1: (a) Design of an optical Mach-Zehnder interferometer (BS: beam splitter, M: mirror, PS: phase shifter) (the beam splitters' thickness is ignored). (b) Design of a Mach-Zehnder type perfect-crystal neutron interferometer in Laue geometry (LLL), with the beam and its widening indicated.

The Bragg diffraction at the perfect-crystal plates (with 3-5mm thickness) of our interferometers has only few arc seconds acceptance angle and also Moiré-fringes have to be avoided, requiring the interferometer plates to be aligned with a precision comparable to the lattice parameter. This is achieved by cutting the interferometer out of a single monocrystalline silicon ingot. Also vibrations and lattice fluctuations due to temperature changes have to be suppressed given the relatively low speed of thermal neutrons. We use interferometers with three plates in Laue geometry (LLL), which is shown in Fig. 1b, or in skew symmetric geometry (with split second plate), which is shown in Fig. 2. The surface of the interferometer plates is perpendicular to the reflecting net planes, so that the diffracted beam leaves the back surface of the crystal (Laue case). The incoming neutron beam splits at the first interferometer plate by amplitude division (similarly to the optical Mach-Zehnder interferometer and contrary to a wave front division interferometer) due to Bragg diffraction into two coherent sub beams. Then the sub beams are reflected by the second plate, pass through an adjustable phase shifter, and finally coherently recombine at the third plate. Turning the phase shifter changes the relative phase between the two sub beams, which yields a sinusoidal oscillation of the intensity behind the interferometer. The oscillation's contrast C (visibility) depends on the relative probability of the neutron to take either the one or the other path: maximum visibility can be achieved for equal probabilities of the two paths. The separation of the two sub beams amounts to 3-5cm, which allows neutron optical devices to be inserted into either of the sub beams.



(a)



(b)

Fig. 2: Skew-symmetric single-crystal neutron interferometer. The mirrors for the sub beams are placed at different beam lengths. In (a) we see a photograph, in (b) a sketch showing the widening of the beam (unmirrored beams are omitted). The distance between the long parallel parts of the sub beams is 33mm (distance between the axes of maximum intensity within the apertures). The width of this interferometer is 4", according to the diameter of the cylindrical silicon perfect crystal ingot of that it was cut out.

The sub beam in path I is transmitted at the first interferometer plate, at the second it is reflected, and at the third plate it is reflected again before it is detected in the so-called O-beam. For the sub beam in path II the sequence is reflection, reflection, transmission. The transmission and reflection coefficients we denote by t and r , respectively, where in the case of a non-absorptive 50:50 beam splitter the equations $|t|^2 + |r|^2 = 1$ and $|t| = |r| = \sqrt{0.5}$ apply. (Silicon has practically no absorption for thermal neutrons). Now a phase shifter is inserted by which the relative phase shift between the two sub beams can be varied. The intensity in the O-beam for an ideal interferometer (100% visibility) is given by: $I_O = |trr\Psi_0 + rrt\Psi_0 e^{i\chi}|^2$, where Ψ_0 is the incident wave function and χ is the phase of the beam in path II relative to that in path I. This equation can be written as

$$I_O(\chi) = A(1 + \cos \chi), \quad (1)$$

where $A = |\Psi_0|^2 |r|^4 |t|^2$. The intensity in the H-beam is

$$I_H(\chi) = |trt\Psi_0 + rrr\Psi_0 e^{i\chi}|^2 = B - A \cos \chi, \quad (2)$$

where $B = |\Psi_0|^2 (|t|^4 |r|^2 + |r|^6)$ and the cosine term is negative because of the odd number of reflections in each of the two sub beams. According to particle conservation, $I_O + I_H$ is constant. While for the above, ideal situation $C = 1$ has been assumed for the contrast, in a real interferometric setup we always have $C < 1$, the O-intensity given by:

$$I_O(\chi) = A(1 + C \cos \chi). \quad (3)$$

The phase shifter is a parallel sided plate that shifts the phase of the neutrons going through according to the formula $\chi_{\text{PS}} = -Nb_c\lambda D_{\text{eff}}$, where χ_{PS} is the phase shift a neutron suffers, N is the particle density, b_c is the coherent scattering length, λ is the neutron wavelength, and the effective thickness D_{eff} is the distance the neutron covers while going through the plate. (Going through our aluminium phase shifter with 5mm thickness, the thermal neutrons with a wavelength of 1.92Å suffer a phase shift of 201.6 radians). The two sub beams go through the phase shifter in different angles, so that by rotating this plate, its effective thickness for each sub beam is changed differently, resulting in a variable relative phase shift between the two sub beams.

2.1.2. Dynamical theory of diffraction

The dynamical theory of diffraction [Rauch and Werner, 2000, Rauch and Petrascheck, 1978], as opposed to the kinematic theory of diffraction, considers the (long enough) spatial periodicity of the (time-independent) interaction potential in a perfect single crystal. Therefore, to obtain the neutron's wave function $\psi(\mathbf{r})$ in the crystal, we have to solve the stationary Schrödinger equation taking into account the crystal potential $U(\mathbf{r})$, which is made up by all scattering centers:

$$\left[-\frac{\hbar^2}{2m_n} \nabla^2 + U(\mathbf{r}) \right] \psi(\mathbf{r}) = E \psi(\mathbf{r}), \quad (4)$$

with

$$U(\mathbf{r}) = \frac{2\pi\hbar b_c}{m_n} \sum_{j,l} \delta(\mathbf{r} - \mathbf{r}_{jl}), \quad (5)$$

where m_n is the neutron mass, \mathbf{r}_{jl} are the positions of the scattering centers, and b_c is the coherent scattering length. The solution of the stationary Schrödinger equation is given by the Bloch-Ansatz:

$$\psi(\mathbf{r}) = e^{i\mathbf{K}\mathbf{r}} u(\mathbf{r}), \quad (6)$$

where $\mathbf{K} = \mathbf{k} - \mathbf{k}_0$ is the wave vector inside the crystal, with \mathbf{k}_0 as the incoming and \mathbf{k} as the diffracted wave vector, and $u(\mathbf{r})$ is the amplitude of this wave. Due to the periodicity of the potential, we can transform these equations into reciprocal space and use the ansatz

$$u(\mathbf{r}) = \sum_{\mathbf{G}} u(\mathbf{G}) e^{i\mathbf{G}\mathbf{r}}, \quad (7)$$

together with the potential's Fourier transform

$$U(\mathbf{G}) = \frac{1}{V} \int V(\mathbf{r}) e^{-i\mathbf{G}\mathbf{r}} d\mathbf{r} = \frac{2\pi\hbar b_c}{Vm_n} \sum_{j,l} e^{-i\mathbf{G}\mathbf{r}_{jl}}, \quad (8)$$

where $V = N_c V_c$ is the volume of the crystal, with V_c being the volume of an elementary cell and N_c the number of elementary cells, and $\mathbf{G} = h\mathbf{g}_h + k\mathbf{g}_k + l\mathbf{g}_l$ is the reciprocal lattice vector with the Miller indices h, k, l . Considering \mathbf{r}_{jl} as the sum of the vector \mathbf{R}_j to the elementary cell j and the vector \mathbf{a}_l pointing from the origin of cell j to the position of the scattering center (atom) l in cell j , we can write:

$$U(\mathbf{G}) = \frac{2\pi\hbar b_c}{V_c m_n} \frac{1}{N_c} \underbrace{\sum_j e^{-i\mathbf{G}\mathbf{R}_j}}_{:=F_L} \underbrace{\sum_l e^{-i\mathbf{G}\mathbf{a}_l}}_{:=F_{hkl}}, \quad (9)$$

where F_L and F_{hkl} are factors associated with the lattice of the crystal and the atomic structure of an elementary cell, respectively. If the Bragg condition $\mathbf{G} = \mathbf{K}$ is satisfied, then $F_L = 1$, otherwise $F_L = 0$. Silicon crystallizes in a diamond cubic crystal structure. In terms of Miller indices, the Bragg condition reads $n\lambda = 2d_{hkl} \sin \theta_B$, where d_{hkl} is the lattice plane distance, which for (diamond) cubic structure is given by $d_{hkl} = a/\sqrt{h^2 + k^2 + l^2}$ with a being the lattice constant. For diamond cubic structure, the structure factor F_{hkl} is equal to 8 if $h + k + l = 4n$, where n is an integer, $4(1 \pm i)$ if $h + k + l$ is odd, and $F_{hkl}^2 = 0$ if $h + k + l$ is even but not exactly divisible by 4 and if h, k, l have mixed parity.

Inserting (7), (6), and (9) in (4), we get the basic equation of the dynamical theory of diffraction:

$$\left[\frac{\hbar^2}{2m_n} (\mathbf{K} + \mathbf{G})^2 - E \right] u(\mathbf{G}) = - \sum_{\mathbf{G}'} U(\mathbf{G} - \mathbf{G}') u(\mathbf{G}'), \quad (10)$$

where the amplitude $u(\mathbf{G})$ is to be determined. A detailed discussion of how to solve this equation can be found, e.g., in [Rauch and Petrascheck, 1976a, Rauch and Petrascheck, 1976b].

In the so-called one-beam approximation only a single lattice vector ($\mathbf{G} = 0$) is assumed to be effective (i.e., periodic structures are not considered) and so the beam is only refracted. The reflected beam may be neglected if the optical potential $U(0)$, which for silicon amounts to $\sim 54\text{neV}$, is very small compared to the neutron beam's kinetic energy, which for a thermal beam with $\lambda = \sim 2\text{\AA}$ is $E_{kin} = \sim 20\text{meV}$. The one-beam approximation holds for a single-crystal far off any Bragg condition as well as for homogeneous non-crystalline materials and is suitable to describe the phase shifter in a neutron interferometric setup. The refracted beam in general changes both direction and magnitude, however, for neutrons the refraction index n is very close to one, for instance, the refraction index of silicon is 0.99999903 and of aluminium 0.9999978.

In the two-beam approximation two lattice vectors ($\mathbf{G} = 0$ and another one $\mathbf{G} \neq 0$) are considered, whereas all other lattice points are assumed to be far off Bragg condition. Equation (10) implies two coupled equations for this case:

$$\mathbf{G} = 0: \quad \left[\frac{\hbar^2}{2m_n} \mathbf{K}^2 - E \right] u(0) = -U(0)u(0) - U(-\mathbf{G})u(\mathbf{G}), \quad (11)$$

$$\mathbf{G} \neq 0: \quad \left[\frac{\hbar^2}{2m_n} (\mathbf{K} + \mathbf{G})^2 - E \right] u(\mathbf{G}) = -U(\mathbf{G})u(0) - U(0)u(\mathbf{G}), \quad (12)$$

where the amplitudes $u(0)$ and $u(\mathbf{G})$ belong to the forward and reflected beam direction, respectively. In the case of a triple Laue (LLL) interferometer, where the beam passes through three crystal plates with parallel surfaces, each with thickness D and the crystal planes being perpendicular to the surfaces (Laue-case), the two above equations yield for the intensities of the O- and H-beam (behind the interferometer, after transmissions and reflections at its plates):

$$|\psi_O|^2 = 4 \sin^4 A (1 - \sin^2 A), \quad (13)$$

$$|\psi_H|^2 = \sin^2 A (1 - 2 \sin^2 A)^2, \quad (14)$$

where we assumed the beam to have negligible deviation from the Bragg angle θ_B and $A = b_c |F| \lambda D / (V_c \cos \theta_B)$.

The silicon 220 lattice spacing ($a_{\text{Si}} = 5.431 \text{ \AA}$ and so $d_{220} = 1.920 \text{ \AA}$) is in the range of the wave lengths of thermal neutrons, which are between 1.9 and 2.7 \AA (with kinetic energies of 22 to 11 meV), corresponding to Bragg angles of 30 to 45°. During the dynamical diffraction at the silicon perfect crystal, deformation of the wave-front and dephasing effects are negligible, therefore coherency of the beam is kept.

2.2. Entanglement: theory and experiments

2.2.1. Einstein-Podolsky-Rosen (EPR) paradox, entangled states, and joint measurements

Entanglement can exist between two or more quantum (sub-)systems, which can be space-like separated or be different degrees of freedom of a single particle. The state of an entangled system cannot be factorized, i.e., it cannot be written as a tensor product of the states of its components. Einstein, Podolsky, and Rosen (EPR) masterminded their famous paradox [Einstein et al., 1935] to demonstrate that (the Copenhagen interpretation of) quantum mechanics is incomplete. Their thought experiment considered two entangled particles and claimed that in this system conjugate quantities, namely, position and momentum, could be simultaneously determined with arbitrary accuracy due to conservation laws, whereas according to quantum mechanics these conjugate quantities could not be simultaneously determined with arbitrary accuracy. They assumed that the elements of reality are local in the sense that an element can only be influenced by events whose light cone includes that element, which they expressed by “... since at the time of measurement the two systems no longer interact, no real change can take place in the second system in consequence of anything that may be done to the first system” [Einstein et al., 1935]. This so-called *local realism* is the main assumption in the EPR claim. Bohm reformulated the EPR argument for the spin of two spatially separated entangled systems to make the EPR paradox mathematically easier to treat and thus to focus on its basic features [Bohm, 1951]. He considered a spin zero system (molecule) of two entangled spin-half atoms.

Then this system is disintegrated by a process that conserves the system's angular momentum, thus the two atoms separating and ceasing to interact while their total spin remains zero. Since the spins of the atoms are correlated, we can (indirectly) determine the spin of one atom by measuring the spin of the other atom. This provides us with a method of determining one atom's spin without disturbing this atom. According to EPR, if we can predict the value of a physical quantity (even without disturbing the system in any way), then there exists a corresponding "element of reality". The spin of atom 2 represents such an element of reality after the spin of atom 1 was measured, and, since the spin of atom 2 was determined without affecting this atom in any way, the said element of reality must have existed in atom 2 also before the spin measurement, having represented a so-called "hidden variable". That the world consists of precisely defined and separately existing "elements of reality" is a tacit assumption by EPR, and is actually in disagreement with quantum theory, which explains the EPR experiment in a perfectly consistent way within its own framework, without the assumption of hidden variables.

According to the quantum mechanical mathematical analysis of the experiment, the system of the spins of two atoms can be described by four wave functions (the dimension of bi-partite two-level quantum systems is four and a complete wave function would be the product of a spin wave function and a wave function for the space coordinates of the atoms):

$$\psi^{\uparrow\downarrow} = \phi_1^{\uparrow}\phi_2^{\downarrow}, \quad \psi^{\downarrow\uparrow} = \phi_1^{\downarrow}\phi_2^{\uparrow}, \quad (15)$$

$$\psi^{\uparrow\uparrow} = \phi_1^{\uparrow}\phi_2^{\uparrow}, \quad \psi^{\downarrow\downarrow} = \phi_1^{\downarrow}\phi_2^{\downarrow}, \quad (16)$$

where ϕ is a spin wave function of atom 1 or 2 with spin up or down as given in the indices. The wave function of a spin zero system before measurement is a superposition of $\psi^{\uparrow\downarrow}$ and $\psi^{\downarrow\uparrow}$. These two wave functions can be combined with same or opposite signs, i.e., as a sum or a difference of the wave functions. In the former case we obtain a state that is symmetric whereas in the latter case a state that is anti-symmetric with respect to interchange of atoms 1 and 2. In both cases the z component of the angular momentum is zero. However, the other components have a non-zero value in the symmetric case whereas in the anti-symmetric case they vanish. Hence the desired superposed wave function is the anti-symmetric one, which is given by

$$\psi_0 = \frac{1}{\sqrt{2}} (\psi^{\uparrow\downarrow} - \psi^{\downarrow\uparrow}). \quad (17)$$

If the total spin is definite, then neither of the individual atoms has a definite spin, i.e., there are definite phase relations between $\psi^{\uparrow\downarrow}$ and $\psi^{\downarrow\uparrow}$, which allows for interference. These definite phase relations also imply a correlation between the same spin components of the atoms. The spin wave function after the

measurements, i.e., after the definite phase relations between $\psi^{\uparrow\downarrow}$ and $\psi^{\downarrow\uparrow}$ are destroyed, is

$$\psi'_0 = \frac{1}{\sqrt{2}} \left(\psi^{\uparrow\downarrow} e^{i\alpha} - \psi^{\downarrow\uparrow} e^{i\beta} \right), \quad (18)$$

where α and β are uncontrollable phase factors that are independent of each other. The state before measurement corresponds to both $\psi^{\uparrow\downarrow}$ and $\psi^{\downarrow\uparrow}$ simultaneously, whereas after measurement the system is either in the state $\psi^{\uparrow\downarrow}$ or in $\psi^{\downarrow\uparrow}$. The measurement transforms the system from one with definite total spin and indefinite spins of each atom into one with definite spins of each atom but indefinite total spin. The measurements of the z component σ_z (or x component σ_x) of the spin of each atom yield values that are opposite to each other. Furthermore, the σ_z (or σ_x) value of each atom is not deterministically related to the state of the system before the measurement, but only statistically. Also, the existence of correlations between the same spin components of the atoms does not require either atom to be affected by what happens to the other. The correlation between the atoms' σ_z values, for example, can be shown by guiding each atom through a Stern-Gerlach apparatus. If a spin component of atom 1 becomes definite (due to measurement), the wave function of atom 2 automatically gets the potentiality to develop the opposite spin value if the same spin component of atom 2 is measured (antiparallel spin correlation).

Now let us consider two entangled photons v_A and v_B that propagate in opposite directions along the z -axis in a rotationally symmetric Bell-state $|\Phi_{AB}\rangle = (|x_A, x_B\rangle + |y_A, y_B\rangle)/\sqrt{2}$, where $|x\rangle$ and $|y\rangle$ denote the polarizations in x and y direction. Two detectors with analyzers for the photons' linear polarization are placed along the photons' trajectories. The analyzers can be rotated around the propagation direction by an angle α for v_A and β for v_B to measure the polarization, where a polarization in x direction yields the value $+1$ whereas in y direction -1 . The projection operators $\hat{P}_x(\alpha) = |\alpha_x\rangle\langle\alpha_x|$ and $\hat{P}_y(\alpha) = |\alpha_y\rangle\langle\alpha_y|$, with $|\alpha_x\rangle = \cos\alpha|x\rangle + \sin\alpha|y\rangle$ and $|\alpha_y\rangle = -\sin\alpha|x\rangle + \cos\alpha|y\rangle$, define the observables for the local polarization measurements. With these we obtain for the probability W to find a photon in a certain polarization state when measuring only one of the photons:

$$W_+(\alpha) = \langle\Phi_{AB}|\hat{P}_x(\alpha)|\Phi_{AB}\rangle = \frac{1}{2}, \quad W_-(\alpha) = \langle\Phi_{AB}|\hat{P}_y(\alpha)|\Phi_{AB}\rangle = \frac{1}{2}, \quad (19a)$$

$$W_+(\beta) = \langle\Phi_{AB}|\hat{P}_x(\beta)|\Phi_{AB}\rangle = \frac{1}{2}, \quad W_-(\beta) = \langle\Phi_{AB}|\hat{P}_y(\beta)|\Phi_{AB}\rangle = \frac{1}{2}, \quad (19b)$$

i.e., in each case we obtain a completely random result: fifty-fifty chance to find v_A to be polarized in x or in y direction, and the same is true for v_B . On the other hand, for joint measurements of the photons we

obtain:

$$W_{++}(\alpha, \beta) = \langle \Phi_{AB} | \hat{P}_x(\alpha) \hat{P}_x(\beta) | \Phi_{AB} \rangle = \frac{1}{2} \cos^2(\beta - \alpha), \quad (20a)$$

$$W_{--}(\alpha, \beta) = \langle \Phi_{AB} | \hat{P}_y(\alpha) \hat{P}_y(\beta) | \Phi_{AB} \rangle = \frac{1}{2} \cos^2(\beta - \alpha), \quad (20b)$$

$$W_{+-}(\alpha, \beta) = \langle \Phi_{AB} | \hat{P}_x(\alpha) \hat{P}_y(\beta) | \Phi_{AB} \rangle = \frac{1}{2} \sin^2(\beta - \alpha), \quad (20c)$$

$$W_{-+}(\alpha, \beta) = \langle \Phi_{AB} | \hat{P}_y(\alpha) \hat{P}_x(\beta) | \Phi_{AB} \rangle = \frac{1}{2} \sin^2(\beta - \alpha). \quad (20d)$$

Accordingly, the probabilities to find the photons in a parallel or in an orthogonal polarization state are

$$W_{\parallel} = W_{++}(\alpha, \beta) + W_{--}(\alpha, \beta) = \cos^2(\beta - \alpha), \quad (21a)$$

$$W_{\perp} = W_{+-}(\alpha, \beta) + W_{-+}(\alpha, \beta) = \sin^2(\beta - \alpha). \quad (21b)$$

If $\alpha = \beta$, then the joint measurements yield $W_{\parallel}(\alpha, \alpha) = 1$ whereas $W_{\perp}(\alpha, \alpha) = 0$. In other words, though the outcome of each individual measurement is random, there is full correlation and anti-correlation between these random results. To indicate the amount of correlation, it is useful to define a correlation coefficient (also called expectation value), which in the case of photon polarization is given by

$$E(\alpha, \beta) = W_{\parallel}(\alpha, \beta) - W_{\perp}(\alpha, \beta) = \cos[2(\beta - \alpha)]. \quad (22)$$

For entangled spin 1/2 particles similar formulas can be used as for the photon case above. Let us consider a state $|\Phi_{AB}\rangle = (|\uparrow_A, \uparrow_B\rangle + |\downarrow_A, \downarrow_B\rangle)/\sqrt{2}$. Here, we have $\hat{P}_+(\alpha) = |\alpha_+\rangle\langle\alpha_+|$ and $\hat{P}_-(\alpha) = |\alpha_-\rangle\langle\alpha_-|$, with $|\alpha_+\rangle = \cos\frac{\alpha}{2}|\uparrow\rangle + \sin\frac{\alpha}{2}|\downarrow\rangle$ and $|\alpha_-\rangle = -\sin\frac{\alpha}{2}|\uparrow\rangle + \cos\frac{\alpha}{2}|\downarrow\rangle$. Accordingly,

$$W_{++} = W_{--} = \frac{1}{2} \cos^2 \frac{\beta - \alpha}{2} \quad \text{and} \quad W_{+-} = W_{-+} = \frac{1}{2} \sin^2 \frac{\beta - \alpha}{2} \quad (23)$$

and

$$W_{\text{parallel}} = \cos^2 \frac{\beta - \alpha}{2} \quad \text{and} \quad W_{\text{antiparallel}} = \sin^2 \frac{\beta - \alpha}{2}, \quad (24)$$

which yields for the correlation coefficient:

$$E(\alpha, \beta) = W_{\text{parallel}} - W_{\text{antiparallel}} = \cos(\beta - \alpha). \quad (25)$$

The postulate of ‘‘wave function collapse’’, introduced in [Heisenberg, 1927, von Neumann, 1932], provides an insight into what happens when measuring the above, entangled states. If we split the joint measurement into two steps and measure only the spin (or polarization) of particle A for now, it appears that by this measurement not only the spin of particle A takes a definite value but also the spin of the distant particle B, which has not yet been interacting with a measurement apparatus. Moreover, the spin of particle

B takes a definite value instantaneously when particle A is measured, no matter the distance between the two particles. Since this is in disagreement with signal transmission between the two particles, according to special relativity theory, it appeared reasonable to look for other explanations for the correlations in the EPR experiment. An explanation could have been that the value of the measured quantity is determined from the time of state creation, independently of any measurement, and the value is independent of any interventions that a spatially separated system is subject to (assumption of so-called *local realism* [Einstein et al., 1935]). However, such pre-determined information is not part of quantum mechanics. So, according to EPR, there are elements of reality that are not included in quantum mechanics and hence represent *hidden variables*. This was the situation before Bell provided his inequality, which showed that hidden variable theories and quantum mechanics lead to distinguishable predictions about the outcomes of experiments.

2.2.2. Bell's inequality

We present here a derivation of Bell's inequality on the basis of the above spin measurements. We assume that the spin of the particles A and B is pre-defined by a variable λ , with a probability $\rho(\lambda)$, where $\int \rho(\lambda)d\lambda = 1$. We introduce the observables $M_A(\alpha, \lambda)$ and $M_B(\beta, \lambda)$, each of which can take the value $+1$ or -1 , while they are given by the same function of the angles. With these the classical correlation coefficient can be written as

$$E_{cl}(\alpha, \beta) = \int \rho(\lambda)M(\alpha, \lambda)M(\beta, \lambda)d\lambda. \quad (26)$$

Now we consider three pairs of angles (α_1, α_2) , (α_1, α_3) , and (α_2, α_3) for the analyzers of particles A and B, and establish the identity

$$M(\alpha_1, \lambda)M(\alpha_2, \lambda) - M(\alpha_1, \lambda)M(\alpha_3, \lambda) = M(\alpha_1, \lambda)M(\alpha_2, \lambda)[1 - M(\alpha_2, \lambda)M(\alpha_3, \lambda)]. \quad (27)$$

From this follows:

$$\begin{aligned} \left| \int \rho(\lambda)[M(\alpha_1)M(\alpha_2) - M(\alpha_1)M(\alpha_3)]d\lambda \right| &= \left| \int \rho(\lambda)M(\alpha_1)M(\alpha_2)[1 - M(\alpha_2)M(\alpha_3)]d\lambda \right| \\ &\leq \int \rho(\lambda)|[1 - M(\alpha_2)M(\alpha_3)]|d\lambda = 1 - \int \rho(\lambda)M(\alpha_2)M(\alpha_3)d\lambda, \end{aligned} \quad (28)$$

where M is also a function of λ . Inserting Eq. (26), we obtain Bell's (original) inequality in terms of classical correlation coefficients [Bell, 1964]:

$$|E_{cl}(\alpha_1, \alpha_2) - E_{cl}(\alpha_1, \alpha_3)| \leq 1 - E_{cl}(\alpha_2, \alpha_3). \quad (29)$$

While this inequality is consistent with the assumption of hidden variables, it conflicts with quantum mechanics: replacing the classical correlation coefficients by the quantum mechanical ones defined in (25),

where we insert for the angles, e.g., $\alpha_1 = \pi/3$, $\alpha_2 = 2\pi/3$, and $\alpha_3 = \pi$, we obtain $1 \leq 1/2$, violating Bell's inequality. A more advanced method to exclude theories that are based on the assumption of local realism, so-called local hidden variable theories or (LHVTs), is the Clauser-Horne-Shimony-Holt (CHSH) inequality [Clauser et al., 1969], which considers an additional (fourth) angle for analyzer adjustment. We will come back to this inequality in more detail for a special application in Sec. 4. All inequalities for correlation measurements in LHVTs, which are collected under the term *Bell inequalities*, are violated by quantum mechanics. LHVTs cannot account for quantum mechanical measurement results—this has been experimentally demonstrated many times [Bertlmann and Zeilinger, 2002], since the first sufficiently precise experiment to violate a Bell inequality [Freedman and Clauser, 1972].

The disagreement between quantum mechanics and LHVTs can also be shown for tripartite entanglement by means of a Greenberger-Horne-Zeilinger (GHZ) state [Greenberger et al., 1989, Greenberger et al., 1990]. This is independent of Bell's approach and shows not a statistical violation but a contradiction between quantum mechanics and LHVTs that is independent of the choice of the parameters in the analysis of the experimentally generated quantum system. Also here, the experimental evidence [Bouwmeester et al., 1999, Zhao et al., 2004, Walther et al., 2005, Lu et al., 2007, Leibfried et al., 2005, Häffner et al., 2005] speaks in favor of quantum mechanics and refutes LHVTs. The experimental generation of a GHZ-like state with neutrons we will discuss later in Sec. 5.

Despite the success of quantum mechanics, there are researchers who see possible loopholes in the experiments and there are also experimental implementations to close these loopholes: noteworthy are the detection loophole [Clauser et al., 1969, Garg and Mermin, 1987, Larsson, 1998, Grangier, 2001, Rowe et al., 2001], pertaining to detector efficiency and particles propagating in weakly correlated directions, and the locality or light-cone loophole [Aspect et al., 1982a, Zeilinger, 1986, Weihs et al., 1998, Aspect, 1999].

2.2.3. *Quantum non-locality vs. contextuality*

While quantum mechanics violates Bell's inequalities due to its non-local characteristics, it also predicts the conflict between measurements on a single-particle system, as was first stated by Kochen and Specker [Kochen and Specker, 1967]: they analyzed sets of measurements of compatible observables and found the impossibility of the consistent coexistence of these measurements. They claimed the incompatibility of quantum mechanics with a larger class of hidden-variable theories, known as noncontextual hidden variable theories (NCHVTs). Noncontextuality is the assumption that the values of commuting observables are pre-defined and mutually independent, no matter the experimental context, even if the events of measurement are not space-like separated, unlike the concept of locality, in which this separation has to be space-like

[Mermin, 1993, Simon et al., 2000]. Accordingly, local hidden variables are a special case of noncontextual hidden variables, and therefore LHVTs are a subset of NCHVTs.

It is also possible to establish a Bell inequality on the basis of noncontextuality rather than locality [Home and Sengupta, 1984, Basu et al., 2001]: We consider two pairs of noncommuting dynamical variables, A_1, A_2 and B_1, B_2 , which pertain to a spin-1/2 particle such that A_i ($i = 1, 2$) commute with B_j ($j = 1, 2$), where A_i and B_j belong to mutually disjoint Hilbert spaces corresponding to mutually commuting degrees of freedom (say, spin and position/momentum). The value of each of A_1, A_2 and B_1, B_2 shall be either $+1$ or -1 . For the outcomes of joint measurements of four commuting pairs we have $A_1B_1 - A_1B_2 + A_2B_1 - A_2B_2 = \pm 2$, which, by taking the ensemble averages, yields:

$$|\langle A_1B_1 \rangle - \langle A_1B_2 \rangle + \langle A_2B_1 \rangle - \langle A_2B_2 \rangle| \leq 2. \quad (30)$$

This is a CHSH-Bell-like inequality that can be considered as a testable consequence of noncontextuality.

2.2.4. *Experimental tests*

Numerous experiments with photons have been carried out to test CHSH-Bell inequalities, e.g., using one-channel polarizers [Freedman and Clauser, 1972, Clauser, 1976, Fry and Thompson, 1976, Pipkin, 1978, Aspect et al., 1981], two-channel polarizers (to distinguish photons blocked by the polarizer from those missed by the detector) [Aspect et al., 1982b], polarization switching setups (closing the locality loophole) [Aspect et al., 1982a, Weihs et al., 1998], or spontaneous parametric down-conversion (closing the detection loophole) [Tapster et al., 1994, Kwiat et al., 1995, Tittel et al., 1998], and to test quantum non-locality in a GHZ state [Bouwmeester et al., 1999, Pan et al., 2000]. Bell inequalities have also been tested with other quantum systems [Rowe et al., 2001, Moehring et al., 2004, Sakai et al., 2006, Matsukevich et al., 2008], including neutrons [Hasegawa et al., 2003]. Experimental testability of quantum contextuality has also been extended to state-independent cases [Cabello, 2008b] and on this basis an experiment using trapped ions has been carried out [Kirchmair, 2009].

In a single-neutron system the entanglement is achieved between different degrees of freedom of one particle and not between different particles. As such, this system is optimal for testing NCHVTs [Cabello et al., 2008a].

3. NEW NEUTRON OPTICAL DEVICES

3.1. Manipulation of neutron's $\frac{1}{2}$ -spin

3.1.1. Adiabatic and non-adiabatic spin manipulation

Let us assume a neutron that travels along the y -axis with velocity $v_n = dy/dt$ through a magnetic field \mathbf{B} directed approximately along the z -axis. If the field's direction varies by an angle β in dependence of the position y along the beam trajectory, which is seen in the neutron's rest frame as a dependence on time, the adiabaticity parameter k has to be considered to estimate how well the precession cone of the spin can follow the direction changes of the field [Kraan et al., 2003]:

$$k = \frac{\omega_L}{\omega_B} = \frac{\mu_n |B| / \hbar}{v_n |d\beta/dy|}, \quad (31)$$

where $\omega_L = \mu_n |B| / \hbar$ is the neutron's Larmor precession frequency at position y , with μ_n as the neutron's magnetic moment, and $\omega_B = |d\beta/dt| = v_n |d\beta/dy|$ is the local rotation frequency of the field as seen by the neutron. There are two limiting cases of this equation (31): (i) the adiabatic limit, given if $k \rightarrow \infty$, in which case the periods $T_L = 1/\omega_L$ and $T_B = 1/\omega_B$ satisfy $T_L \ll T_B$ so that the precession cone follows the direction changes of the field while the cone angle remains constant (adiabatical following), more exactly, the probabilities in the superposition of an up- and down-spin state in the single-neutron system remain constant, and (ii) the non-adiabatic limit, given if $k \rightarrow 0$, in which case $T_L \gg T_B$, so that the precession cone does not follow the field's direction changes and the cone angle does not remain constant, i.e., the probabilities in the superposition of an up- and down-spin state change. (The technique of adiabatical following is used for the guide magnetic field to keep a polarized neutron beam).

3.1.2. Radio frequency spin flipper

A radio frequency spin flipper (RF flipper) is a solenoid (tube-shaped coil) operated with an AC current in the radio frequency range, generating a time-dependent magnetic field $B_{\text{rf}} \cos \omega t$. While the magnetic guide field B_0 is perpendicular to the neutron beam, B_{rf} is directed along the beam axis, i.e., the beam passes the tube shaped coil in axial direction (without touching any material). The efficiency of spin flipping by an RF flipper is given by [Williams, 1988, Suda, 2006]:

$$f = \frac{\sin^2 \left[\frac{\gamma}{2v_n} L_{\text{rf}} B_{\text{rf}} \sqrt{1 + (2\delta B_0/B_{\text{rf}})^2} \right]}{1 + (2\delta B_0/B_{\text{rf}})^2}, \quad (32)$$

where γ is the gyromagnetic ratio, v_n is the neutron's velocity, L_{rf} is the effective length of the RF flipper, and $\delta B_0 = B_0 - B_0^*$ is the deviation of the guide field's strength from the calculated field $B_0^* = -\omega/\gamma$ at that the Larmor frequency of the neutron spin is in resonance with the RF coil's frequency. As we see from the above formula, in order to achieve the highest possible flipping efficiency $f = 1$, we need to satisfy (i) $B_{\text{rf}} = \pi(j + \frac{1}{2})2v_n/(\gamma L_{\text{rf}})$, where j is an integer number, and (ii) $\delta B_0 \rightarrow 0$. The first requirement is easily satisfied by adjusting the current through the RF flipper. The second and more critical requirement means that the applied guide field should be as homogeneous as possible over the effective region of the RF flipper. The flipping efficiency is reduced if there are variations in the guide field across this effective region. The relation between such field variations and f is illustrated in Fig. 3. (The flip efficiency, when many neutrons with slightly different properties have to be spin flipped, is also affected, e.g., by the monochromaticity $\Delta\lambda_n/\lambda_n$, i.e., the neutron velocity range, of the beam, but this parameter is not subject to adjustment in our setups). An important property of the time-dependent field of an RF coil, as opposed to the time-independent field of a DC current coil, is that photon exchange takes place during spin flip, changing the total energy (together with the potential energy, more exactly, the Zeeman energy) of the neutron by an amount of $-\hbar\omega$ (for a flip from spin-up to down).

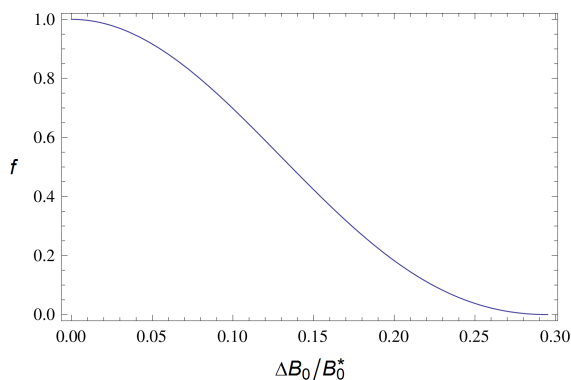


Fig. 3: Flip efficiency of an RF coil versus variation of the guide field. The RF coil has 5cm length and its operating frequency corresponds to a resonance field of $B_0^* = 20\text{G}$.

3.2. RF coil equipped with mini guide field for operation in an interferometer

For the preparation of certain neutron states it is necessary to manipulate energy by different amounts within the same setup. An energy shift, together with a spin flip, is accomplished by an RF coil and depends on the coil's operating frequency. In order to achieve the maximum flipping efficiency, the strength of the magnetic guide field has to be adjusted so that the neutron spin's Larmor frequency is equal to the coil's frequency. Therefore, for different energy shifts not only different operating frequencies but also different guide field strengths should be adjusted. Adjustment of the field strength for an RF coil to operate at its maximum efficiency at different frequencies can be achieved by installing a Helmholtz coil pair over the

RF coil, whose field adds to the beam line guide field. The handling of an RF coil equipped with its own Helmholtz coil pair represents a special challenge when this device shall operate in an interferometer (IFM). In an IFM, namely, one faces two problems: (a) handling of the heat due to the coils, in particular due to the Helmholtz coils, and (b) the very limited space in the IFM, which makes the homogeneity of the Helmholtz coil pair's field an issue. In order to develop an RF coil equipped with its own Helmholtz coil pair for the IFM experiments, we need to address these two problems.

The usual method to dissipate the heat produced by an RF coil in an IFM has been to use a water-cooled coil body [Sponar, 2011]. The drawback of this method is that it has to rely on heat conduction between the heat producing coil wire and the cooled body, which results in unwanted temperature gradients. While this method is sufficient for "bare" RF coils, the cooling of RF coils equipped with a small Helmholtz coil pair (with diameter $\sim 40\text{mm}$) is not feasible due to the considerable heating power of the Helmholtz coils ($\sim 8\text{W}$) when producing a field with the needed strength ($\sim 20\text{G}$). Such individually adjustable guide field manipulators or miniature guide fields (miniGF), each of which locally changes the overall guide field only for a given RF coil, are required so that the frequency of each RF coil in the IFM, and therefore the associated energy shifts, can be adjusted independently of the strength of the guide field. This is essential for the corresponding experiments described in Sec. 5. This now became feasible due to our new cooling method: we integrate the coil wires directly into the water channel, so that the wires are submerged into the flowing medium. This is realized by a leakproof plastic box that contains the coils and is flooded with running water, where the box has an axial tunnel free from water for the neutron beam to pass through, as illustrated in Fig. 4. Since the wires are in direct contact with the water, the new cooling method does not require good heat conducting materials, e.g., copper, which could allow for unwanted eddy currents due to the RF coil. We may use for the coil body a material with low thermal and electric conductance. An estimation of temperature increase due to an 8W Helmholtz coil pair if the water flow is 12.5l/min (maximum flow rate of a "Thermo Haake DC10") yields only 0.008°C , which is acceptably small. Since this new coil cooling method seemed promising, we started to optimize a miniGF for an RF coil.

After development and optimization, this new RF spin flipper equipped with a miniGF was integrated into a water-box and was used in the experiment [Erdősi et al., 2013], which is described in this dissertation. This method of mini guide fields with water-box was also used in further experiments [Denkmayr et al., 2014, Geppert et al., 2014, Sponar et al., 2014] afterwards.

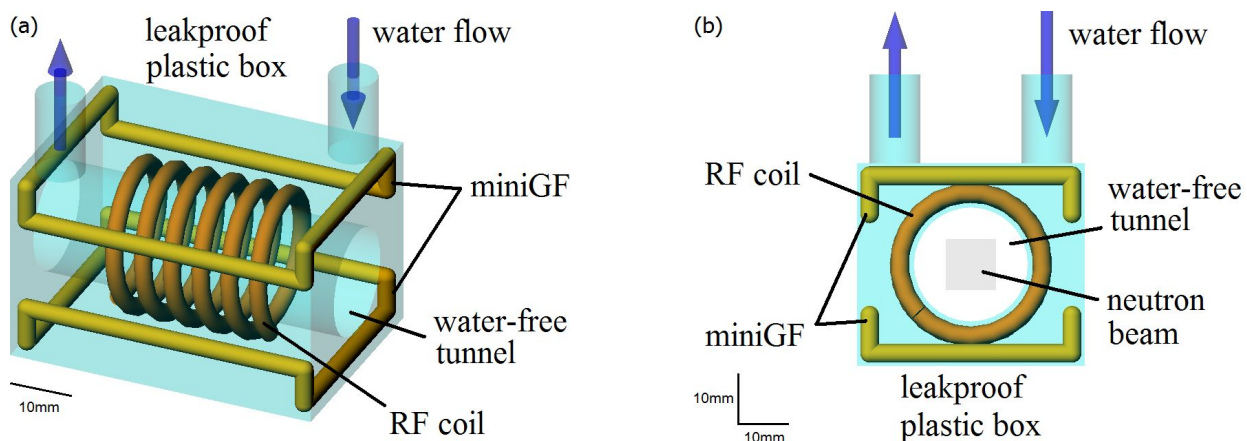
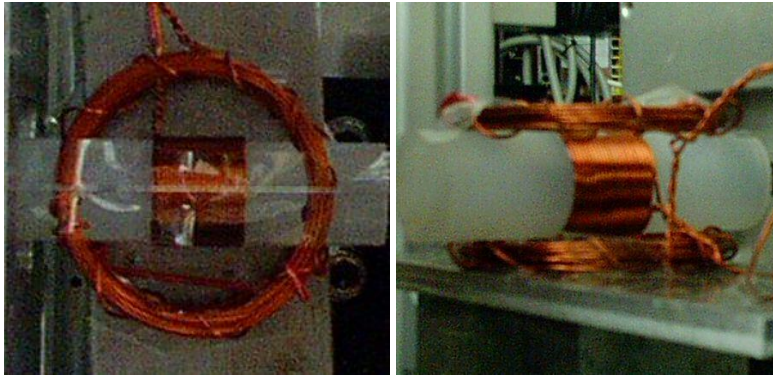


Fig. 4: RF coil with miniGF in flowing water, (a) three-dimensional view and (b) front view. The length of the box is 4-5cm.

3.2.1. Optimization of the miniGF

After having a promising solution for the heat dissipation problem with the coils, the first question was whether it is possible at all to achieve a reasonable flip ratio for an RF coil equipped with a miniGF. (The flip ratio of a spin flipper is defined as the ratio of the counts measured while the flipper is switched off to the counts measured while the flipper operates at its highest efficiency in the given situation). An RF coil achieves its highest flipping efficiency in a homogeneous field, which can be provided by a miniGF only in a limited spatial region and the maximum size of the miniGF is limited by the IFM. On the other hand, the longer an RF coil is the higher is its efficiency. For the first attempt of a miniGF a circular Helmholtz coil pair was prepared with mean diameter 40mm (and mean coil distance equal to the coils' radius, according to the definition of a Helmholtz pair) with 16 windings each. In this miniGF an RF coil with length 15mm was placed, using the maximum of the homogeneous region of the field provided by the miniGF, as shown in Fig. 5. It should be tested whether this RF coil achieves a reasonably high flip ratio when the external magnetic field is provided in a fifty-fifty ratio by the beam line guide field and by the miniGF. In sum a 20G field was applied (in which the RF coil operated at 61kHz) while the RF coil's amplitude was scanned. The test was carried out at the neutron polarimeter with $\lambda = 1.99\text{\AA}$ of the Atominstitut, the beam line containing only the RF coil with miniGF between the polarizer and the analyzer. The RF coil achieved a flip ratio of 34, which was promising enough to go on with the optimization of this new spin flipping apparatus. The measurement result is plotted in Fig. 6. For comparison, a DC spin flipper (that was subject only to the beam line guide field) achieved a flip ratio of ~ 60 .



(a)

(b)

Fig. 5: Pictures of the first attempt of an RF coil combined with a miniGF. The miniGF's diameter is 40mm and the length of the RF coil is 15mm.

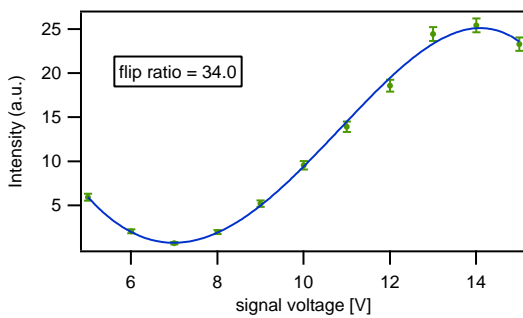
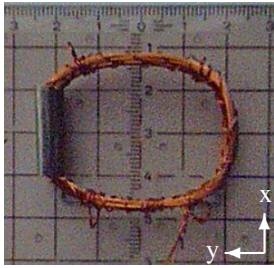
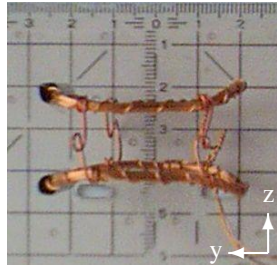


Fig. 6: First attempt of an RF coil combined with a miniGF. During an intensity vs. RF signal voltage (amplitude) scan the flip ratio achieved 34, which is reasonable.

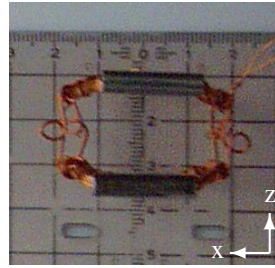
Though an ideal Helmholtz coil pair is circularly shaped, in the IFM a rectangular coil pair is more suitable due to the available space. Furthermore, the miniGF should be bent up at its entrances through that the neutron beam enters and leaves the miniGF for a rather smooth field transition and, more importantly, to put the wires away from the top and bottom part of the beam aperture in order to avoid non-adiabatic influences on these parts of the aperture. Also, the miniGF should offer a rather constant field profile along the beam axis for a region as long as possible. The Helmholtz coil pair's sufficiently homogeneous field region depends on the exact shape of the coils. In order to extend this region, the shape of the miniGF can be varied. To determine an optimal shape for the miniGF, four miniGFs with slightly different shapes were constructed (see Figs. 7-10, for their exact dimensions see Tab. I) and their field profiles were measured, as illustrated in Fig. 11. (The windings of each coil were held together by a piece of wire that was wrapped around helically).



(a) Top view.

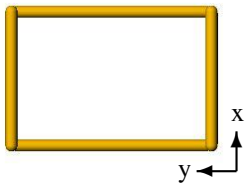


(b) Side view.

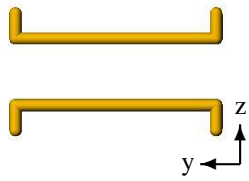


(c) Front view.

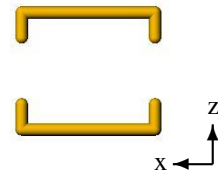
Fig. 7: Photos of miniGF2 with Mu-metal at one entrance.



(a) Top view.

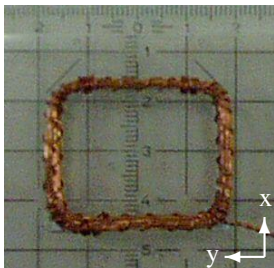


(b) Side view.

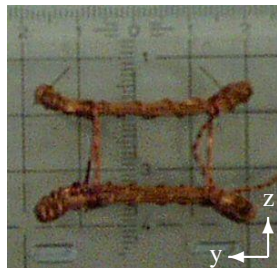


(c) Front view.

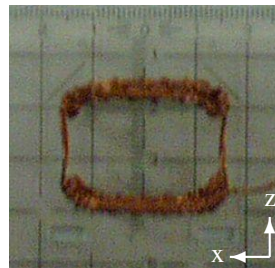
Fig. 8: Illustration of miniGF3. This miniGF yielded the best results and was later installed into the water box. (Unfortunately, no camera was available at the time before installation).



(a) Top view.

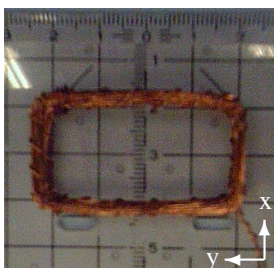


(b) Side view.

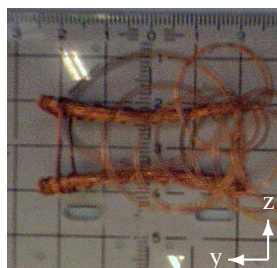


(c) Front view.

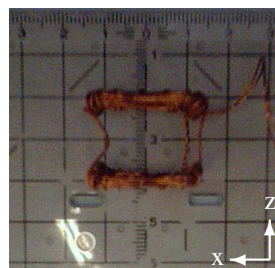
Fig. 9: Photos of miniGF4.



(a) Top view.



(b) Side view.



(c) Front view.

Fig. 10: This shows photos of miniGF5.

miniGF	l	w	h	b	n	I
2 (see Fig. 7)	45.0	28.0	14.0	2.0	12	1587
3 (see Fig. 8)	41.0	27.0	13.0	2.3	12	1439
4 (see Fig. 9)	33.6	26.7	14.0	3.2	10	1689
5 (see Fig. 10)	40.8	22.0	12.3	2.5	14	1163

TABLE I: Measured parameters of each miniGF. The cross section of each coil was round and had 2mm diameter, where a wire with 0.4mm thickness was used with winding numbers 10-14. The coils' dimensions are given for center to center of the cross sections. Legend: l , w , h (length, width, height of coils in mm), b (bending up at entrances in mm), n (number of windings per coil), I (current in mA for $B = 10\text{G}$ at center).

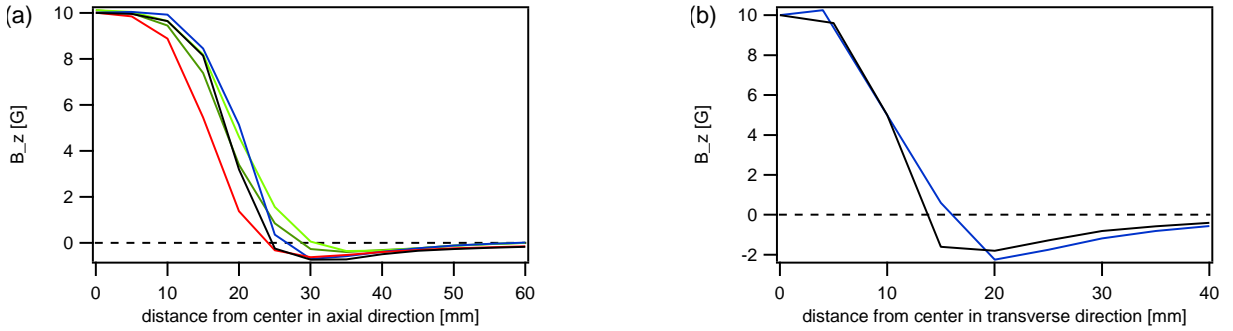


Fig. 11: Profiles of the field's z component, measured (a) along the longitudinal axis of each miniGF and (b) along the transverse axis of two miniGFs. Legend: miniGF2 (Fig. 7) (dark-green), miniGF2 with Mu-metal (Fig. 7) (green), miniGF3 (Fig. 8) (blue), miniGF4 (Fig. 9) (red), miniGF5 (Fig. 10) (black). miniGF3 had the widest homogeneous field region about its center.

The mini guide field with the widest homogeneous field region about its center, in which region the RF flipper should operate, was the one with the most abrupt bending up at its entrances (miniGF3 in Fig. 8), as was measured and plotted in Fig. 11. In this coil pair, the coils' distance from each other was half their width, in accordance with Helmholtz geometry, throughout the entire length of the coils. The other mini guide fields (miniGF2, 4, and 5 in Figs. 7, 9, and 10, respectively) were smoothly bent up, so that they did not satisfy the Helmholtz geometric requirement ($\text{height} = \text{width}/2$) for their entire lengths and so the field faded faster toward the entrances. Although with the abrupt bending up at the entrances of miniGF3 the field became a little more negative outside the miniGF, this negative field is well compensated by the overall guide field of the beam line and therefore is not problematic in practice.

The miniGF with optimal field profile, i.e., miniGF3, was installed into the water box (illustrated in Fig. 4). At first it should be tested whether the miniGF allows all neutrons to pass adiabatically; in the ideal case the miniGF should not cause a spin flip, i.e., its flipping efficiency should vanish. [The flipping efficiency is calculated from the intensities I_0 at switched off and I_{miniGF} at turned on miniGF by the formula $(1 - I_{miniGF}/I_0)/(1 + I_{miniGF}/I_0)$]. For this purpose the miniGF was operated with the maximum current possible in standing water (running water was not available), which allowed for 2.76A, and also the beam aperture was at its maximum size of $8 \times 8 \text{mm}^2$, resulting in distances of 3.8mm above and below the beam to the bent up coil entrances. Here the miniGF had a flip efficiency of 0.0910 ± 0.0076 , which was not acceptable. Since the coils, having 2mm cross section, already touched the top and bottom walls of the box, they were pressed flat to the wire thickness of 0.4mm, by which the minimum coil-neutron distances became 5.4mm, which was enough to achieve an acceptable flip efficiency of 0.0096 ± 0.0073 . Since also other parameters could have been changed in order to reduce the flip efficiency, the general rule, which is suggested here, is that the coils at the bent up entrances should be pressed flat to the minimum, so that maximum distance to the beam is accomplished.

Next, an RF coil was tested with the miniGF. According to the miniGF's measured field profile in Fig. 11, the miniGF offers $\sim 10 \text{mm}$ sufficiently homogeneous field ($\Delta B_0/B_0 < 0.05$) around its center. Tests of an RF coil with 19.8mm length and 21mm diameter placed in the center of the miniGF showed a flip ratio of 38.88 ± 0.16 in a 20G field provided in a fifty-fifty ratio by the miniGF and the beam line guide field, as plotted in Fig. 12. This flip ratio is at any rate sufficient for our experiments. For comparison, the same RF coil achieved a flip ratio of 39.87 ± 0.17 if the 20G field is solely provided by the beam line guide field, which shows that the miniGF does not significantly degrade the flip ratio. The flip ratios were determined by intensity vs. frequency measurements, with peaks found at 61.34kHz in both cases.

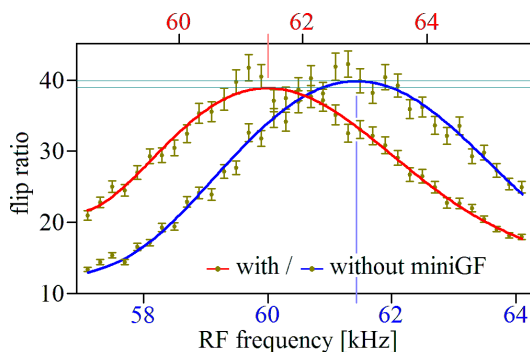


Fig. 12: Flip ratios of the RF coil with and without miniGF. The flip ratios are 38.88 ± 0.16 and 39.87 ± 0.17 , respectively (the peaks are both at 61.34kHz, but the peak with miniGF is shifted to the left in the illustration so that the curves do not overlap).

A further issue is the effect of the miniGF's stray field on nearby RF coils. The region that the beam passes after the miniGF was tested with an RF coil with 20.0mm length, 21mm diameter, and flip ratio of 43.0 in the beam line guide field (with 20G). While also the miniGF operated at 20G, the flip ratio of the RF

coil was measured at distances of 0.5mm, 7.0mm, and 15.0mm from the miniGF by means of a frequency scan, which resulted in flip ratios of 16.2, 21.9, and 26.4, respectively. The results of these measurements are plotted in Fig. 13. (The peaks are at frequencies of 62.1kHz, 61.3kHz, and 61.0kHz, respectively, and for the non-operating miniGF at 61.4kHz). The fact that the nearer the RF coil was placed to the miniGF the worse was the flip ratio is due to the low homogeneity of the stray field in the vicinity of the miniGF. In the IFM experiments described in Sec. 5 the RF coil that the beam passes after the miniGF shall operate in $\pi/2$ flip mode, which only requires a flip ratio of 2, therefore the miniGF's stray field does not matter there.

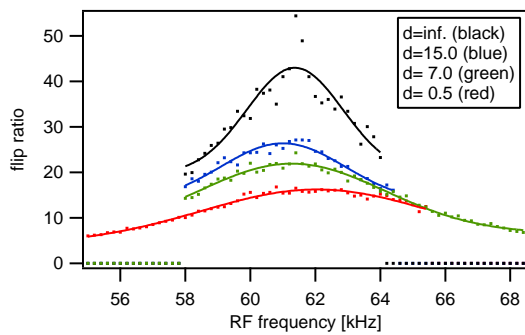


Fig. 13: Flip ratio of an RF coil with 20.0mm length when placed behind the operating miniGF. The RF coil's flip ratio of 43.0 reduces to 16.2, 21.9, and 26.4 at distances of 0.5mm, 7.0mm, and 15.0mm from the miniGF, respectively.

The effect of the miniGF's stray field next to the miniGF, in the way as the neighboring beam path in the IFM is affected, was tested in 33mm distance (according to the distance between path I and II in our skew symmetric IFM shown in Fig. 2) with a 51.3mm long RF coil with 21mm diameter. The flip ratio amounted to 85.4 in the beam line guide field with miniGF switched off and to 83.6 when the miniGF operated at 20G, i.e., no significant loss in the flip ratio due to the stray field could be seen. The corresponding scan is plotted in Fig. 14.

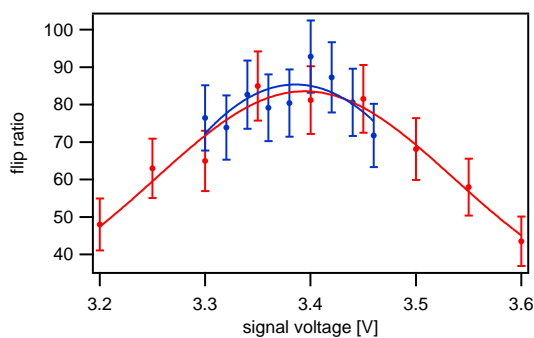


Fig. 14: Scans of the flip ratio of an RF coil with 51.3mm length in the beam line guide field with miniGF switched off (blue curve with peak of 85.4) and next to the miniGF operating at 20G in 33mm distance (red curve with peak of 83.6). The miniGF's stray field has practically no effect on the flip ratio of the RF coil.

It is worth noting here that a miniGF can also be used as a mere Larmor precession manipulator (see Sec. 3.3.4) (in which case no RF coil is needed).

3.2.2. Development of the water box

After having proved the applicability of a miniGF, the next step was the development of a water-proof box in that the heat producing coils can be integrated. Since we are not bound to use a good heat conductor with our new coil cooling method, we chose acrylic glass for the material of the box, which has the advantage of being an electric insulator, not allowing for eddy currents from RF operation. Acrylic glass, being transparent, also allows to look inside the box without having to open it. Furthermore, the workability of acrylic glass, its chemical resistance, the possibility of gluing it, and the existence of water-proof glue for acrylic glass make it an ideal material. As for the glue, we chose “ACRIFIX[®] 1R 0192 (ACRIFIX[®] 192)”, which was the only water-proof and gap filling glue for acrylic glass at the market at the time.

An important question was how much the box together with the miniGF affects the contrast of the IFM. The box was tested with the skew-symmetric IFM shown in Fig. 2, filling out the inside of the IFM with 1-3mm minimum distances between the box and the plates of the IFM and leaving space for the phase shifter. A sketch showing the basic position of the box with respect to the IFM and a picture of the actual situation are given in Figs. 15 and 16. The mean contrast of the empty IFM was $C = 0.625 \pm 0.004$, an interferogram is plotted in Fig. 17. Then, the contrasts of the interferograms of the IFM with the box were measured in dependence of the temperature (at each temperature six interferograms were recorded). The result is plotted in Fig. 18. The contrast at the ideal temperature was measured to be 0.664 ± 0.016 . After this, the miniGF with $\sim 8\text{W}$ heating power was switched on and again a temperature scan was made to test the miniGF's influence on the contrast. The result is plotted in Fig. 19, the contrast at the ideal temperature being 0.640 ± 0.004 . These results show that the box allows for very good temperature control of the IFM and that no contrast loss occurs if the ideal temperature is adjusted, compared to the contrast of the empty IFM, not even with the mini guide field switched on. The miniGF touched the walls of the box in one corner and filled out one third of the box's volume. The way of the water was defined by walls within the box, so that the water passed the miniGF and the RF coils one after the other. The water should pass the coil with highest (heating) power first, i.e., the miniGF, otherwise significant contrast losses are the result.

While being in use, the main problem of the water box turned out to be its watertightness. The box got leaks at random spots in time intervals of some days to 1-2 weeks, times with running, times with standing water. This demanded further developments in the construction of such a box. The first version was made of acrylic glass with 1mm thickness. Given the fact that the hardened glue is more brittle than acrylic glass, the first explanation of water leaks was that the 1mm thick plates give in due to the pressure while water is pumped through the box, so that the walls of the box slightly deform. The glue does not follow these deformations, thus the glued joints becoming weaker with time. Accordingly, for the second version of the

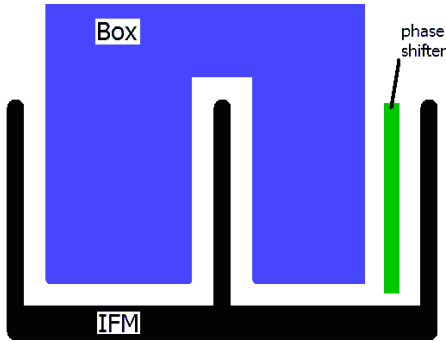


Fig. 15: Sketch of the IFM with water box. The box fills out the inside of the IFM (here an LLL-IFM), leaving space for the phase shifter.

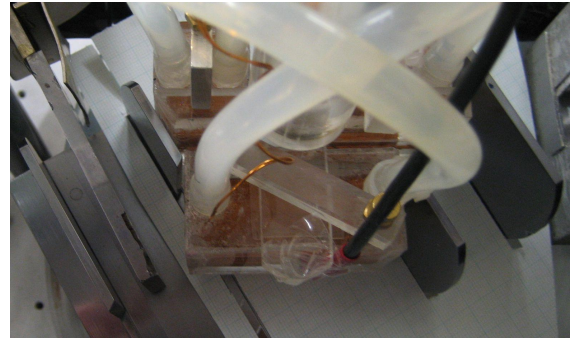


Fig. 16: Photo of the actual situation in the skew symmetric IFM. The box is between the IFM plates, with 1-3mm distances to their edges.

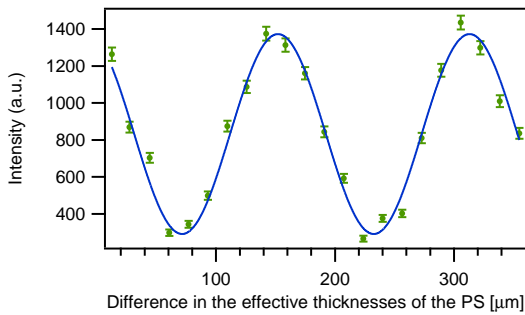


Fig. 17: Interference oscillation with the empty IFM. The average contrast was $C = 0.625 \pm 0.004$, one of the contrast scans shown on the left.

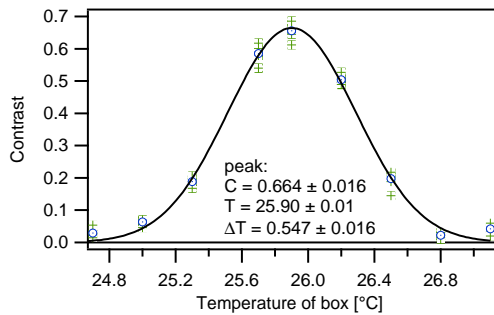


Fig. 18: Contrast vs. temperature scans with the box with running water in the IFM, while all coils are switched off. At each temperature 6 contrast scans were made. The ideal temperature was found at 25.90°C, with a mean contrast of 0.664 ± 0.016 , according to the Gauss fit, and the best measured contrast was 0.685.

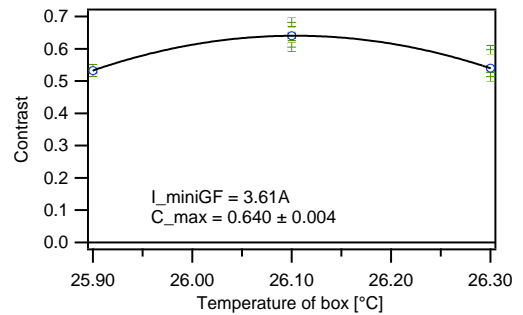


Fig. 19: Contrast vs. temperature scans with the box with running water in the IFM and with the miniGF switched on. The miniGF with $R = 0.6\Omega$ was operated with $I = 3.61A$, which meant a heating power of $\sim 8W$. The mean contrast at the ideal temperature amounted to 0.640 ± 0.004 , according to the polynomial fit, and the best measured contrast was 0.682.

box we used acrylic glass with 3mm thickness. Despite the stiffer box walls and the larger glued joints, this did not solve the problem with the watertightness. Therefore, the problem does not seem to be with the mechanical properties of the glue. We assume there is a problem with the drying of the glue, or its aging, or it is not absolutely water-proof, contrary to the claims of the manufacturer. Knowing this, in the third version of the box we greased the inner edges with silicone sealant (a sealing mass usually used in sanitary installations). The sealed edges of the box indeed remained water-proof for at least 28 days while exposed to running water almost all time.

Concerning the shape of the box, to achieve an even better temperature control we produced a box that completely surrounds the IFM, as depicted in Fig. 20. The gaussian “contrast vs. temperature” curve was measured with this box, the result plotted in Fig. 21. The width of the gaussian curve was significantly expanded compared to the result with the previous box, as we see when we compare Figs. 18 and 21: the gauss curves’ sigma coefficients (ΔT in $^{\circ}\text{C}$) were 0.547 ± 0.016 and 0.77 ± 0.05 , respectively. When comparing these results, it should also be mentioned that two different IFMs were used, with different maximum contrasts of the empty IFMs; the completely surrounding box was used in an IFM with much higher empty contrast, namely, the average contrast of the empty IFM was measured to be $C = 0.804 \pm 0.005$, one of the interferograms plotted in Fig. 22. Such an IFM is more sensitive to environmental effects. In spite of this, a significantly better contrast stability could be achieved with the completely surrounding box, which is important for some experiments requiring high contrasts. Disadvantages of such a box are clearly the higher production effort and sometimes bulkiness and inaccessibility during handling in the IFM. Of course, also this box did not cause any contrast loss with the ideal temperature being adjusted, at which the average contrast was 0.80 ± 0.03 , as shown in Fig. 21.

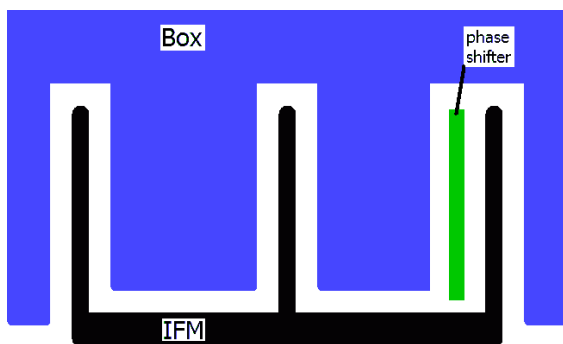


Fig. 20: Sketch of the IFM with full-surrounding water box. While the box completely surrounds the IFM, there is enough space left for the phase shifter. In the real model the lowest distances between the box and the IFM plates amounted to 2mm.

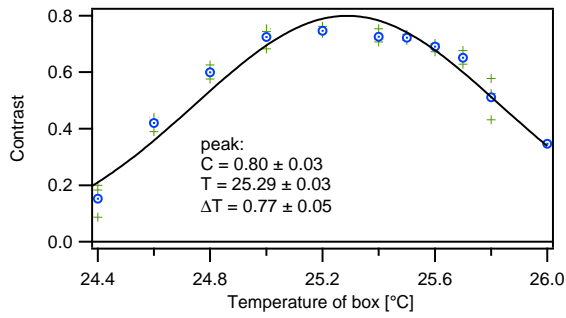


Fig. 21: Contrast vs. temperature scans with the box completely surrounding the IFM with running water. At each temperature 3 contrast scans were made. The ideal temperature was found at 25.29°C, with a contrast of 0.80 ± 0.03 , according to the Gauss fit.

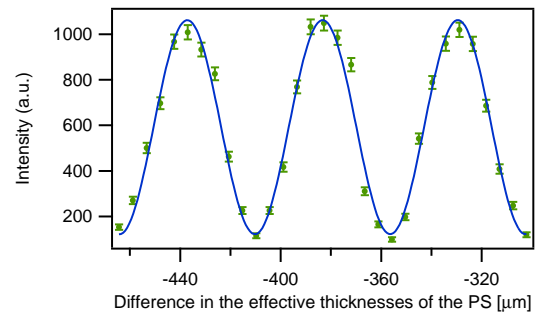


Fig. 22: Interference oscillation with the empty IFM. An average contrast of $C = 0.804 \pm 0.005$ was achieved, one of the contrast scans plotted.

A phenomenon worth to be mentioned is the oxidation of the copper wires in water, which becomes visible after 1-2 weeks of operation. Though enameled copper wire is used, the coating gets tiny cracks (hardly visible with the naked eye) during spooling. Through these cracks the water runs under the coating, thus having direct contact with the copper wire. Thus the surface of the wire is transformed into copper(II) oxide, CuO (black colored), and copper(II) hydroxide, Cu(OH)₂ (turquoise colored), around the coating cracks, which is shown in the picture of the coils in Fig. 23. This has no effect on the operation at all. Nevertheless, a problem may appear if the enamel coating is damaged over an area large enough that the water does not just stand under the coating but can bypass the wire surface while flowing, sponging away the porous oxides and hydroxides. If this occurs, the process of wire material loss is significantly accelerated. With such a coating damage the life time of a wire with 0.4mm thickness is limited to ~7 weeks of (constant) operation in flowing water.

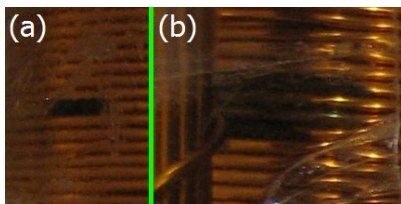


Fig. 23: Oxidization of the enamel coated copper wire. The oxidization took place around tiny cracks in the coating, where the water could go under the coating.

3.3. Larmor accelerators and decelerators for the Interferometer

3.3.1. Motivation: generation of a Bell-like state in neutron interferometry

The need for a manipulator of Larmor precession frequency in the interferometer (IFM) arose in connection with the generation of a Bell-like state of the form

$$|\Psi\rangle = \frac{1}{\sqrt{2}} (|\leftarrow\rangle \otimes |I\rangle + |\rightarrow\rangle \otimes |II\rangle), \quad (33)$$

which represents the entanglement between the spinor part and the spatial part of a neutron's (normalized total) wave function [Sakurai, 1994], where $|\leftarrow\rangle$ and $|\rightarrow\rangle$ denote the two spin states and $|I\rangle$ and $|II\rangle$ denote the two beam paths in the IFM. For the experiment [Hasegawa and Erdős, 2011], which we will describe in detail in Sec. 4, we have introduced a new method to generate the above Bell-like state: this method allows and/or requires the use of a Larmor precession manipulator in the IFM. There are two methods previously used, the first using a Mu-metal DC spin flipper in the IFM and the second using an RF spin flipper in the IFM. We discuss these two methods first, in order to show the advantages of the new method.

3.3.2. Drawback of the previous methods to generate a Bell-like state in neutron interferometry

The first method used a spin-up polarized neutron beam with spinor $|\uparrow\rangle$ that entered the IFM and split into two partial beams I and II at the first plate, e.g., [Hasegawa et al., 2003, Hasegawa et al., 2007], as depicted in Fig. 24. In one beam path the spin was flipped by $\pi/2$ and in the other path by $-\pi/2$, so that the spinor in path I became to $|\leftarrow\rangle$ while in path II to $|\rightarrow\rangle$, thus yielding the Bell-like state in Eq. (33). (A so-called $\pi/2$ flip yields a 50% probability that the spin flips from up to down or vice versa, i.e., a $\pi/2$ flip produces a fifty-fifty superposition of an up- and down-spin state in the single-neutron system). Given the guide field B_0 in z -direction, the $\pi/2$ and $-\pi/2$ flips mean that the spin was flipped in both IFM paths from the z -direction into the x - y -plane and the spin in path I and II as a result had a precession angle difference of π , as shown in Fig. 25. These spin flips are equivalent to those performed by a usual DC spin rotator in $\pi/2$ flipping mode and one in $-\pi/2$ flipping mode. Spin flips due to a stationary field that the neutron goes through require direction changes of the field that satisfy the non-adiabatic limit of Eq. (31), which in the case of a DC flipper is given due to the sharp bounds of the field defined by the coils that the neutron goes through. To imitate this effect of DC flippers, a special spin flipper was developed, namely, a metal strap of high magnetic permeability (Mu-metal) across the IFM that guided the magnetic field of DC coils placed outside the IFM into the latter. The magnetic field in the strap was perpendicular to the guide field, similarly as the (idealized) field inside a usual DC spin flipper, and was sharply bounded by the surface of

the metal so that the non-adiabatic limit was satisfied. This method aimed to avoid temperature disturbance of the IFM due to the heat producing DC coils and to avoid small-angle scattering as well as dephasing of the neutron beam, which would have occurred when passing through coils; these effects would have caused considerable loss of contrast. So, in this previous setup, rather the coils were placed as far away from the IFM as possible and their magnetic field was guided by the metal strap to the beam in the IFM. The Mu-metal sheet, which the neutrons had to pass through, however, still reduced interference contrast by $\sim 19\%$ due to dephasing, as an unwanted side-effect—this was critical.

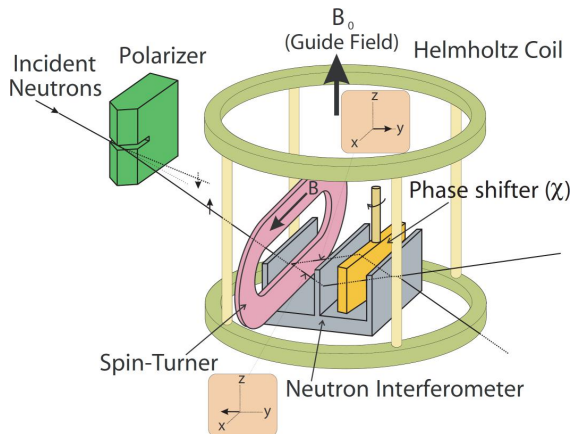


Fig. 24: Experimental setup using the first previous method of state generation from the previous experiment [Hasegawa et al., 2003].

After this experiment, another spin-path entanglement preparation scheme was introduced to circumvent the unwanted decrease of contrast due to the Mu-metal sheet. To avoid such loss, RF spin flippers were used instead of the Mu-metal spin flipper in the IFM [Bartosik et al., 2009, Sponar, 2011]. Accordingly, the neutrons did not touch any material, thus the main reason for contrast loss being eliminated. However, an RF flipper does not only change the spin but also the energy state of the neutron, which represents the drawback of this preparation scheme: the preparation of a Bell-like state cannot take place completely in the IFM, for which only two degrees of freedom should be entangled (spin and path), because with the RF coil in the IFM an entanglement with three degrees of freedom (spin, path, and energy) is generated, actually. The unwanted energy difference between the two partial wave functions has to be corrected after the recombination of the two IFM paths, in the analysis stage, by an additional RF coil, performing a spin flip with half the energy shift (plus and minus half for the spin-up and -down neutrons, respectively).

3.3.3. New method to generate a Bell-like state in neutron interferometry

Considering the above problems, the improvement of the above, established methods of Bell-state generation evolved step by step. After some unsuccessful attempts, the breakthrough came by recognizing that for the generation of the Bell-like state in Eq. (33) the spin flips do not need to take place in the IFM at all. A

schematic view of the previous methods is given in Fig. 25. The new method to generate the state in Eq. (33) is based on the fact that only the directions of the spin flips are different for the two IFM paths, whereas the absolute values of the flips are equal, viz. $\pi/2$. Therefore, spin preparation (not the state preparation) can be separated into two steps, as shown in Fig. 26: (i) In the first step the spin is flipped by $\pi/2$, which changes the spinor from $|\uparrow\rangle$ to $|\rightarrow\rangle$, i.e., inclines the spin from the z -direction into the x - y -plane. This step is carried out before the beam enters the IFM, so that the spinor of the neutron beam entering the IFM is given by $|\rightarrow\rangle$, rather than by $|\uparrow\rangle$ as in the previous methods. (ii) In the IFM the azimuthal angles of the spins in path I and II are turned by π relative to each other while the spins remain in the x - y -plane, so that in one path the spinor remains $|\rightarrow\rangle$ while in the other path it is changed to $|\leftarrow\rangle$. Only this step (ii) needs to be performed within the IFM. Indeed only step (ii) represents a part of state preparation, whereas the foregoing spin flip from $|\uparrow\rangle$ to $|\rightarrow\rangle$, together with the polarizer, is just a preliminary spin manipulation. Applying a spin rotator before the IFM is trivial, it is rather the combination of the two aforesaid spin manipulations (i) and (ii) that is new.

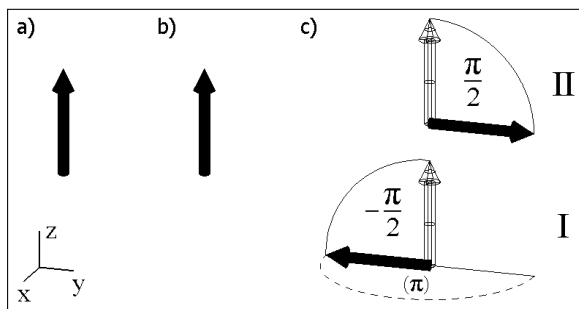


Fig. 25: Previous method of spin preparation.
a) Spin vector of a neutron after the polarizer,
b) spin vector when entering the first IFM plate,
and c) spin vectors when entering the second IFM plate, where the beam is already split up into path I and II.

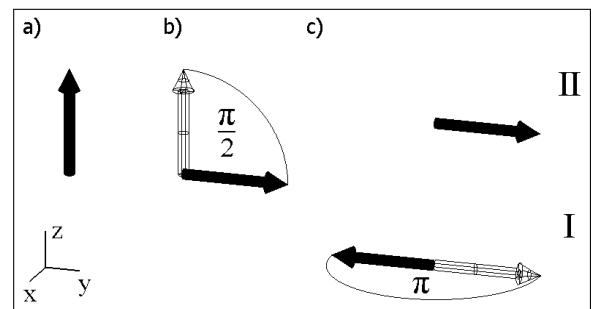


Fig. 26: New method of spin preparation.
a) Spin vector of a neutron after the polarizer,
b) spin vector when entering the first IFM plate,
after step (i) of the new spin preparation method
was performed by a DC flipper in $\pi/2$ flipping
mode, and c) spin vectors when entering the
second IFM plate, where the beam is already
split into two paths and step (ii) of the new spin
preparation method, representing the actual
state generation, has been performed, resulting
in a precession phase difference of π between
the spins in path I and II due to changing the
spin precession speeds relative to each other.

A change in the spin's azimuthal angle, as in step (ii) of the new spin preparation method (Fig. 26), naturally exists during Larmor precession in the guide field and the strength of the magnetic field determines the angular speed ω_L of the Larmor precession, according to the formula

$$\omega_L = -\frac{2\mu}{\hbar}B = B \times 1.833 \times 10^8 \text{rad/s}, \quad (34)$$

where the magnetic field strength B is given in Tesla. By changing the Larmor precession speeds in paths I and II relative to each other, the desired precession phase difference of π can be achieved. The crucial point is that for a change in the speed of Larmor precession, which keeps the z -component of the spin vector constant, no direction change $d\beta/dy$ in the magnetic field is needed but merely a change in the field strength. This means that the non-adiabatic limit of Eq. (31) does not need to be satisfied. In practical terms rather the adiabatic limit of spin guiding has to be respected in this case by avoiding abrupt changes in the direction of the field. Since no abrupt changes in the magnetic field are required, no sharp bounds in the field are necessary. This fact gives our new, two stepped spin preparation method its advantage over the previous method: since no sharp bounds are required in the field that the neutrons pass in the IFM, no material needs to be placed in the way of the neutrons in the IFM.

For the realization of the new spin preparation method a Larmor accelerator or decelerator as required for step (ii) has to be developed that can be placed in the IFM with as small as possible effect on its contrast. For step (i) a DC spin flipper is to be used. We developed several appropriate Larmor accelerators and/or decelerators, which devices can be classified as either active (which consume energy and therefore produce heat) or passive (which consume no energy). The active Larmor precession manipulators are coils that produce a magnetic field parallel to the guide field thus locally increasing or decreasing the strength of the guide field. The passive devices, on the other hand, produce no additional field but locally redistribute the guide field that is already there, thus locally increasing or decreasing its strength on the way of the neutrons. In the following we describe these Larmor precession manipulators and their development.

The new spin preparation method, shown in Fig. 26, has been used in the experiment [Hasegawa and Erdős, 2011] and also in several further experiments [Denkmayr et al., 2014, Geppert et al., 2014, Sponar et al., 2014] afterwards.

3.3.4. Mini guide field (miniature Helmholtz coil)

An active Larmor precession manipulator to perform step (ii) of the new spin preparation method (Fig. 26) for the Bell-like state (33) can be realized by using a miniature guide field manipulator (miniGF) introduced in Sec. 3.2. To keep possible field direction changes as small as possible, four miniGFs can be

used, i.e., one in each path in the front and in the back side of the IFM. For the housing a water box that encases the whole IFM is recommended to achieve as good as possible temperature stability.

3.3.5. *Mu-metal tube*

A passive Larmor decelerator for step (ii) of the new spin preparation method (Fig. 26) for the Bell-like state (33) can be realized by a local shielding of the guide field in one of the two beam paths of the IFM. This method was chosen for our experiment to violate a Bell-like inequality [Hasegawa and Erdős, 2011]. For the material of the shielding we have chosen Mu-metal, which is a standard material for magnetic shielding. The shape of this optical element is determined by the following requirements: (i) In order to achieve a shielding effect, the device must have some closed shape. (ii) The neutron beam should pass the shielding without having to touch any material. (iii) The field inside the shielding shall be still strong enough to keep the beam's polarization. (iv) The field inside and around the shielding should be sufficiently homogeneous so that spin can adiabatically follow possible direction changes of the field. These four requirements are well satisfied by a Mu-metal sheet bent to the shape of a circular cylinder with both ends open. Considering workability and price, we have considered Mu-metal sheets of thickness 0.05mm and 0.1mm. The homogeneity of the magnetic field inside and around the Mu-metal tube made of such a sheet was tested with iron powder in a homogeneous magnetic field of 45G produced by permanent magnets. The

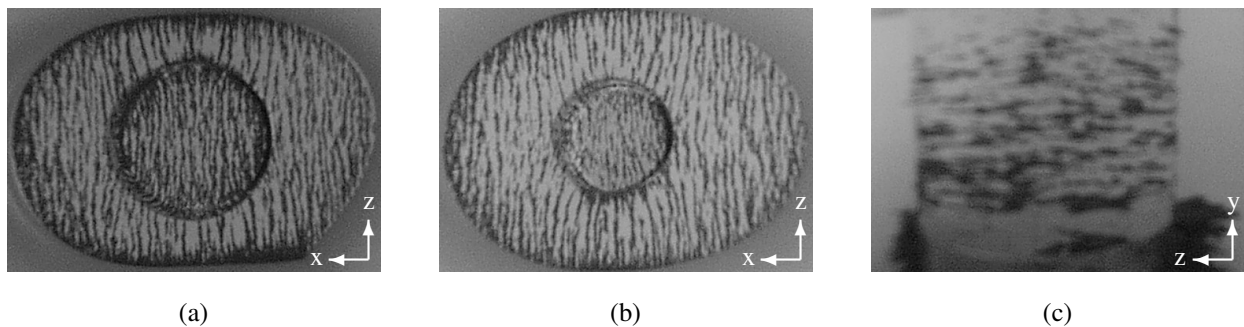


Fig. 27: Pictures of the iron powder test of the Mu-metal tube in the homogeneous field produced by permanent magnets. (a) The here tested Mu-metal tube has a diameter of $d = 30\text{mm}$, length of $l = 20\text{mm}$, and wall thickness of 0.1mm (the test area is confined by an elliptically bent sheet of paper). Inside the Mu-metal tube no inhomogeneous areas can be identified. (b) A similar test made with a $d = 20\text{mm}$ Mu-metal tube. Also here no inhomogeneous areas can be identified inside the tube. (c) The Mu-metal tube is at the bottom in this picture and its longitudinal axis lies vertically in the image plane. Here the sufficient homogeneity of the field at an opening of the tube shall be demonstrated.

results are shown in Fig. 27, which suggest the sufficient homogeneity of the field affected by the Mu-metal tube.

This soft-magnetic tube, through which the neutron beam passes in axial direction (going through the tube's open ends) without touching any material, as shown in Figs. 28 and 45, weakens the guide field inside and thus makes the Larmor precession slower within this region of the IFM path. The phase of the spin precessions in path I and II relative to each other has to be adjusted. In principle, this can be done by means of adjusting the tube's dimensions, which determine the tube's shielding effect, and by the strength of the (unshielded) guide field. So the next step is to determine the appropriate size range of the Mu-metal tube. Upper constraints are given by the IFM, in which the tube has to be placed, namely, by the distance between the beam paths I and II, and by the distance of the beam from the ground basis of the IFM, which is not exactly known in advance. Lower constraints are given by the aperture of the neutron beam.

The experiments to find out the amount of slow-down of Larmor precession by a Mu-metal tube of appropriate size in a magnetic field of appropriate strength were carried out at the neutron polarimeter with $\lambda = 1.99\text{\AA}$ (corresponding to a neutron velocity of $\sim 1988\text{m/s}$) of the TRIGA research reactor of the Atominstitut in Vienna. The experimental setup, which is depicted in Fig. 28, included two DC spin flippers both performing a $\pi/2$ -flip and the sample (the Mu-metal tube) placed between these flippers. The second DC coil (which the neutrons pass after the sample) was successively moved backwards and at each position the intensity was measured. These recorded intensities yield a sinusoidal oscillation curve, whose phase difference relative to the reference sinusoidal curve recorded without the Mu-metal tube was determined. This phase difference is equal to the retardation of spin precession due to the Mu-metal tube.

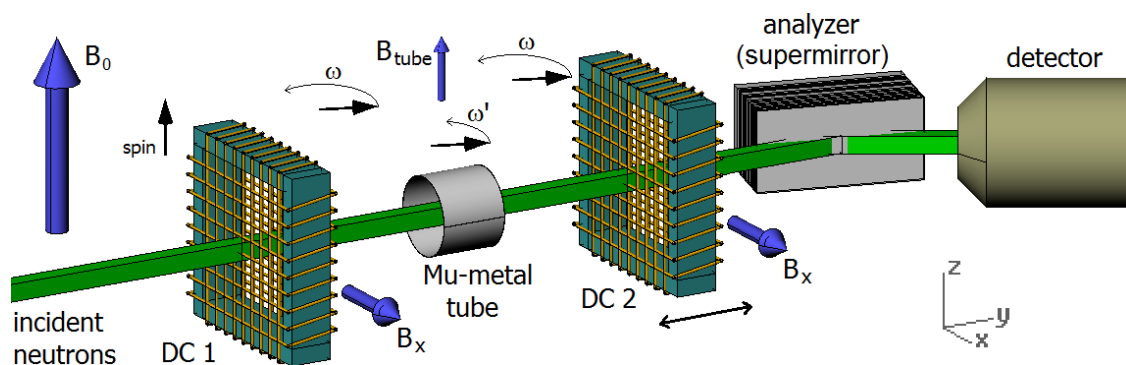


Fig. 28: Setup to determine the precession retardation by the Mu-metal tube. The DC spin flippers each perform a $\pi/2$ flip and the beam line guide field is denoted by B_0 . The precession speed is slower in the region of the tube, since $B_{\text{tube}} < B_0$.

For the first measurements a tube with diameter $d = 25\text{mm}$ and length $l = 20\text{mm}$ of a Mu-metal sheet

with thickness of 0.05mm was used. A field of $B\hat{z} = 10\text{G}$ was applied, which means that the neutron traveled a distance of $\sim 68\text{mm}$ during a period of Larmor precession, according to formula (34). The beam aperture had rectangular cross-section with $5\times 5\text{mm}$. Measurements with different tube positions were recorded, where the tube's axis was always parallel to the beam axis. The tube was displaced perpendicularly to the magnetic field lines. In the first set of such measurements the beam went through the tube. The results are shown in Fig. 29. If the beam axis coincides with the central axis of the tube, as shown in Fig. 28, then the precession is retarded with respect to the reference measurement without the tube by $(0.719 \pm 0.007)\pi$. This shows that the order of magnitude of the size of the tube and the strength of the guide field were chosen well. It is also important that the obtained contrast of $C = 0.965 \pm 0.010$ with the tube is not worse than that of the reference measurement with $C_{\text{ref}} = 0.947 \pm 0.10$ without the tube, which demonstrates that all neutrons within the aperture are affected to the same extent by the magnetic shielding and all neutrons go through the tube adiabatically. If the tube is displaced horizontally by 6.5mm from the beam axis (i.e., the distance between the beam axis and the inside lateral surface of the tube are 6mm), then the precession retardation with respect to the reference amounts to $(0.705 \pm 0.007)\pi$ and the contrast is $C = 0.934 \pm 0.010$. Also this contrast shows that all neutrons within the aperture are affected to the same extent by the magnetic shielding and all neutrons go through the tube adiabatically. The first standard deviations of the two above precession retardations just overlap, which means that the measurement with the 6.5mm displaced tube approximately defines the maximum possible (circular) aperture of the beam when it goes through the 25mm diameter tube and this maximum aperture is given by approximately 18mm. On the other hand, this also means that we could reduce the tube's diameter for the $5\times 5\text{mm}$ beam aperture to approximately $d = 13\text{mm}$.

In the second set of such measurements the Mu-metal is horizontally displaced so that the beam does not go through the tube but passes next to it, with the purpose to simulate the tube's effect on the neighboring beam path in the IFM. The results of these measurements are shown in Fig. 30. The tube was placed at distances of 3mm, 6mm, 8.5mm, 11mm, 16mm, and 21mm between the beam axis and the lateral surface of the tube. The precession retardations with respect to the reference measurement amounted to 0.406 ± 0.009 , 0.313 ± 0.007 , 0.270 ± 0.007 , 0.233 ± 0.007 , 0.176 ± 0.007 , and 0.118 ± 0.008 , respectively, all numbers given in units of π radians. A diagram of these precession retardations vs. the distances is shown in Fig. 31.

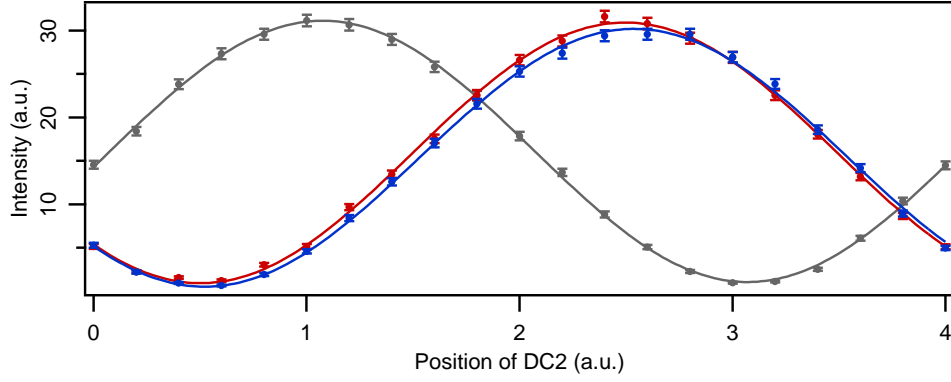


Fig. 29: Measurement of precession retardation of the neutron beam going through the Mu-metal tube. If the tube's central axis coincides with the beam axis, whose measurement is given by the blue curve, and if the tube's axis is displaced horizontally by 6.5mm (red curve), then the precession is retarded with respect to the reference measurement without the tube (grey curve) by $(0.719 \pm 0.007)\pi$ and $(0.705 \pm 0.007)\pi$, respectively.

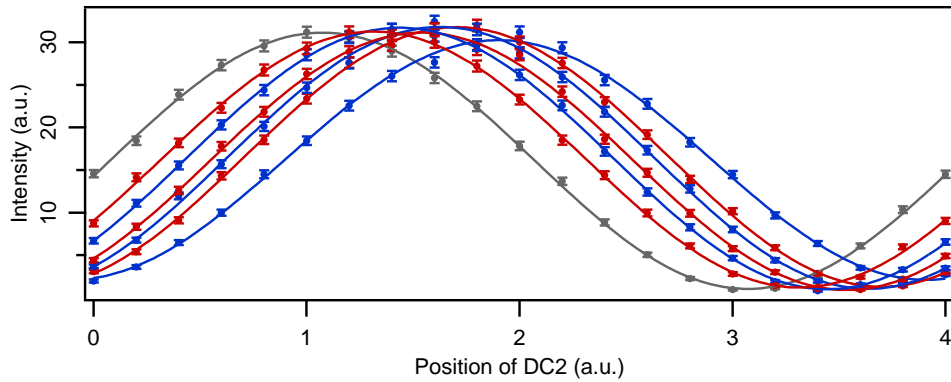


Fig. 30: Measurement of precession retardation of the neutron beam passing next to the Mu-metal tube, which is horizontally displaced relative to the beam. The distances between the beam axis and the lateral surface of the tube were 3mm, 6mm, 8.5mm, 11mm, 16mm, and 21mm, the corresponding measurement results given in the same order by the blue and red curves from right to left. The precession retardations with respect to the reference measurement, given by the grey curve, amount to 0.406 ± 0.009 , 0.313 ± 0.007 , 0.270 ± 0.007 , 0.233 ± 0.007 , 0.176 ± 0.007 , and 0.118 ± 0.008 , respectively, all numbers given in units of π radians.

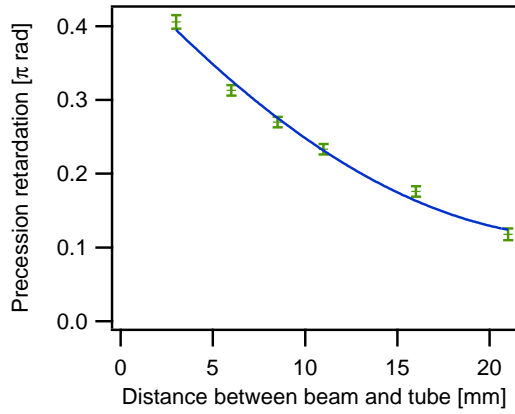


Fig. 31: Graphic illustration of the Larmor precession retardation vs. the distance between the beam axis and the lateral surface of the Mu-metal tube, as given by the results shown in Fig. 30. The measurement points are fitted with a polynomial.

A method to adjust the retardation in Larmor precession due to the Mu-metal tube consists in an adjustment of the length of the tube. This can be realized by a telescopic construction of several tubes resulting in a tube with continuously adjustable length. A test with such a construction consisting of two tube segments was carried out to analyze the efficiency of this way of Larmor precession retardation adjustment. The tube segments, each with wall thickness of 0.05mm, gave a tube with diameter $d = 25\text{mm}$ and a length l variable between 20 and 40mm. The experimental setup was the same as for the above measurements, but here only the tube's length was varied while the tube's axis coincided with the beam axis. The results of these measurements are plotted in Fig. 32. The precession retardations for the tube lengths of 20, 30, and 40mm were 0.932 ± 0.007 , 1.139 ± 0.008 , and 1.293 ± 0.010 , respectively, given in π radians. One sees here that the appropriate tube length is between 20 and 30mm.

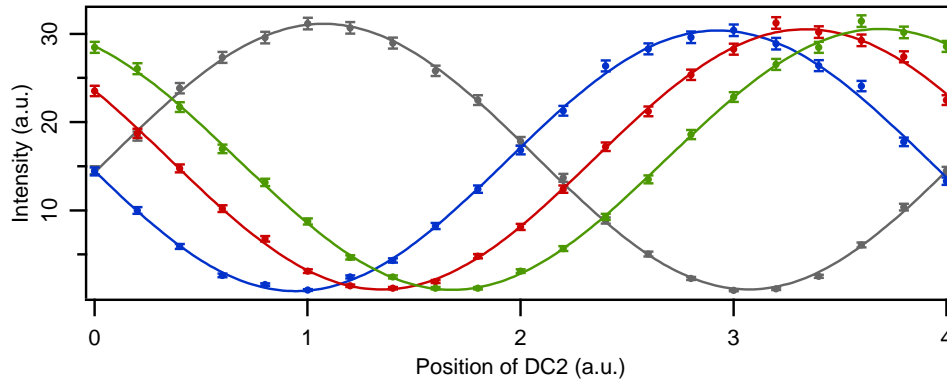


Fig. 32: Measurement of precession retardation under variation of the tube's length. The tested lengths were 20mm (blue), 30mm (red), and 40mm (green) and the precession retardation with respect to the reference measurement (grey) amounted to 0.932 ± 0.007 , 1.139 ± 0.008 , and 1.293 ± 0.010 , respectively, given in units of π radians.

The retardation in Larmor precession and the length of the tube are not directly proportional, according

to the results in Fig. 32. This is due to the fact that at the tube's openings the magnetic field lines are diverted to the tube well before the tube's material region, as shown in the approximative sketch in Fig. 33. This results in an additive component to the tube's shielding effect, a component that is independent of the tube's length (as long as the tube is not too short). Accordingly, the precession retardation due to the tube can be characterized by a formula of the form $A + B * l$, where the precession retardation consists of a contribution A due to the length-independent component of the shielding and a length-dependent contribution with B as the conversion factor between precession retardation and tube length l . Hence the efficiency of the tube in retarding precession in dependence of its length is described by $A/l + B$ and therefore decreases if the tube's length increases. For our typical tubes the decrease in efficiency with length is significant, as we see with the above, telescopic tube: if we define the efficiency at $l = 20\text{mm}$ as 100%, then at $l = 30\text{mm}$ we have 81%, and at $l = 40\text{mm}$ only 69%. Adjustment of precession retardation in the actual experiment by varying the tube's length is not recommended, because it can hardly be automated and also in consideration of the significant decrease of the tube's efficiency with increasing length and the limited amount of space in the IFM. The decision about the tube's length should be made during the preparation of the tube before its use in the actual experiment.

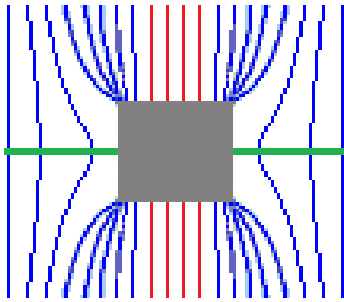


Fig. 33: Approximative illustration of the magnetic field lines in the effective region of the Mu-metal tube (grey colored rectangle with the green line as the beam axis) to show how the shielding effect in principle depends on the tube's length. The number of the red field lines depends on the tube's length, thus yielding a length-dependent contribution to the magnetic shielding, while the number of the blue field lines does not depend on the tube's length, thus yielding a length-independent contribution.

A more promising method to adjust the retardation in Larmor precession in the actual IFM experiment consists in adjusting the guide field. The advantages of this method are the adjustment by simply varying the electric current of the coils for the guide field, which can be easily automated. Roughly there is a linear correlation between the Larmor precession retardation (which is directly related to the tube's shielding effect) and the strength of the guide field with coincidence of zero field strength and zero precession retardation, provided that the shielding material has not reached magnetic saturation (which for Mu-metal is not reached until $\sim 8000\text{G}$) and it has no remanence magnetization. In practical terms this correlation means that a very accurate adjustment of precession retardation can be achieved already by calculation af-

ter only one measurement of precession retardation at an “arbitrary” field strength, though this initial field strength should be chosen, in practice, sufficiently near by the final value. To test this method of adjustment, the precession retardation by a Mu-metal tube with $d = 15\text{mm}$, $l = 21\text{mm}$ and wall thickness 0.1mm was compared at 10G and 20G guide field. Here the rectangular beam aperture had $9 \times 7\text{mm}^2$ (width x height) for more intensity and to simulate the increase in beam width due to the IFM plates. Which IFM is to be used was already known this time, namely the small LLL-IFM with distance of 35mm between its plates, at Bragg angle of 30° , which exhibits the highest contrast. Therefore the tube’s positioning with respect to the two beam paths in the IFM could be accurately simulated at the polarimeter by two consecutive scans. At each field strength three scans were made: a reference measurement without tube, a measurement with coinciding beam axis and tube axis, and a measurement imitating the tube’s position and effect with respect to the other (neighboring) beam path in the IFM. The precession retardation of the two latter measurements relative to each other is of interest and should be π if adjustment is correct (which is just approximately required in this phase of preparation). The results are plotted in Fig. 34.

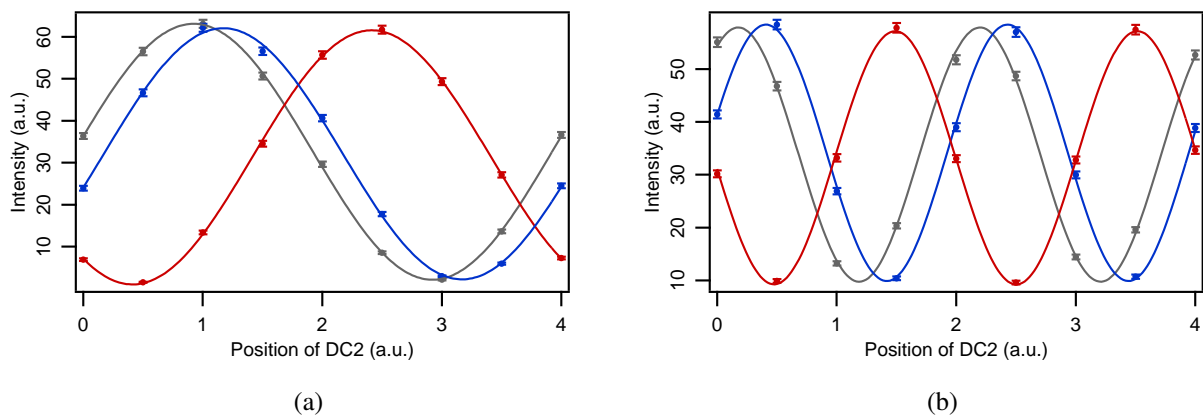


Fig. 34: Measurement of precession retardation simulating the situation in the IFM at (a) $B = 10\text{G}$ and (b) $B = 20\text{G}$. The beam going through the tube (red curves) showed a precession retardation of (a) 0.614π and (b) 1.067π with respect to the simulated neighboring IFM beam path (blue curves). The precession in the neighboring path is retarded by (a) 0.126π and (b) 0.231π with respect to the reference measurement (grey curves).

From these results a method to adjust precession retardation by adjusting the guide field is confirmed to work well. By the results of 0.614π and 1.067π precession retardation at $B = 10\text{G}$ and $B = 20\text{G}$, respectively, the direct proportionality between precession retardation and field strength could only be approximately verified, probably due to an unrecognized remanence magnetization of the tube. Unfortunately, there was no time to repeat these measurements.

On the basis of the above measurements shown in Figs. 29-34, we decided to continue our tests using tubes with $d = 15\text{mm}$ and wall thickness of 0.1mm and applying a guide field of 20G . We have chosen the higher value for the field strength in order to better approach the adiabatic limit around and in the tube. We seek for the length of the tube to cause a precession retardation of π between path I and II of the IFM at a field strength between 20 and 25G . Again the beam paths of the IFM are simulated by two consecutive scans with different tube positions relative to the test beam (at the polarimeter). Three tubes with lengths of 21.2mm , 17.9mm , and 12.1mm were tested. The precession retardations of the beam going through the tube relative to the neighboring beam were 1.268π , 1.244π , and 0.956π , respectively. The results of these measurements are plotted in Fig. 35.

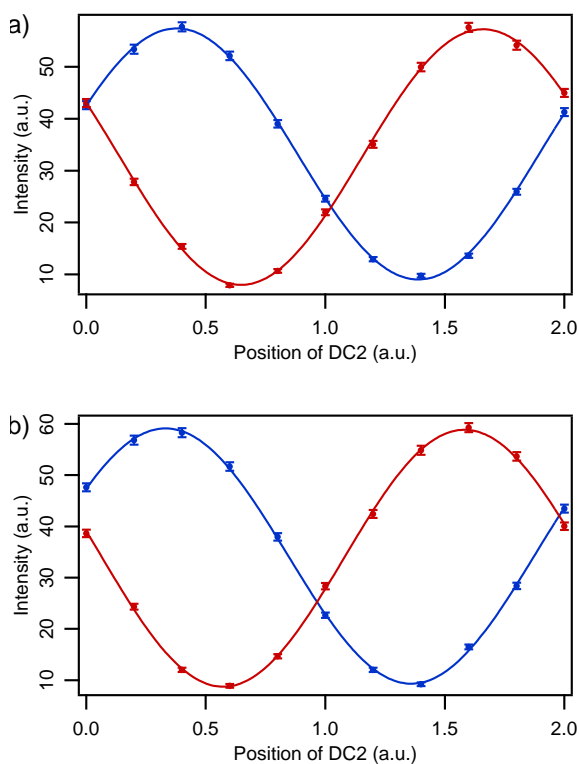


Fig. 35: Measurement of the precession retardation of the beam going through the tube (red curves) relative to the neighboring beam (blue curves) in a 20G field. The tested tubes had lengths of (a) 21.2mm , (b) 17.9mm , and (c) 12.1mm , causing precession retardations of 1.268π , 1.244π , and 0.956π , respectively.

On the basis of the above measurements plotted in Fig. 35, the appropriate tube length for a 20G guide field seems to be a little bit above 12mm . The final dimensions of the tube we chose to be $l = 13\text{mm}$ and $d = 15.5\text{mm}$ with wall thickness of 0.1mm . Then the precession retardation under variation of the distance of the tube to the “neighboring beam” was measured, which corresponds to a measurement under variation of the distance between the tube and the second plate of the IFM. The results are plotted in Fig. 36. The tube should have a distance between 1mm and 5mm to the second IFM plate. The results show that the Mu-metal tube with the chosen size will be appropriate for the intended IFM experiment to demonstrate the violation of a Bell-like inequality.

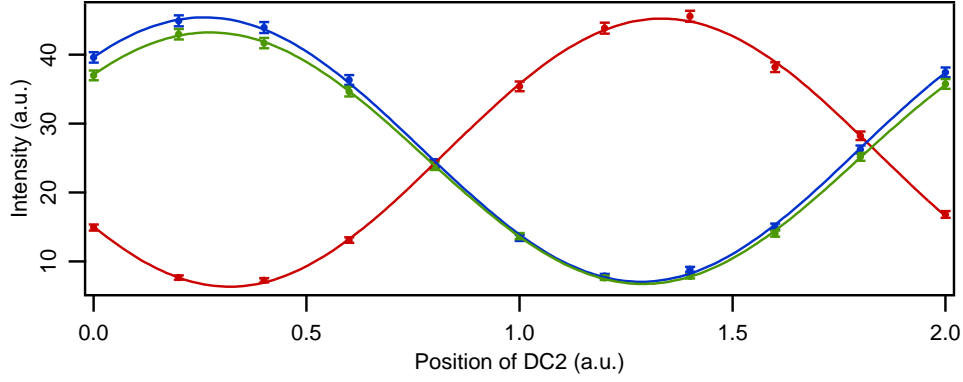


Fig. 36: Measurements of precession retardation under variation of the (simulated) distance between the edge of the tube and the second IFM plate. At distances of 1mm (blue curve) and 5mm (green curve) the precession retardations are 1.064π and 1.044π , respectively, relative to the beam going through the tube (red curve). In any case the adjustment to π is feasible by slight variation of the strength of the guide field.

The Mu-metal tube was brought to the perfect-crystal neutron optics beam line S18 at the high flux reactor of the Institute Laue-Langevin (ILL) [Kroupa et al., 2000] to be used in the IFM experiment. The tube was placed in path I of the IFM and the precession angle difference between path I and II was adjusted to be $(0.985 \pm 0.047)\pi$, the measurement result plotted in Fig. 37, which sufficiently approximates the desired difference of π . During the use of the tube in the IFM it could also be demonstrated that the tube causes no significant loss of interference contrast. The measured interferogram is plotted in Fig. 38.

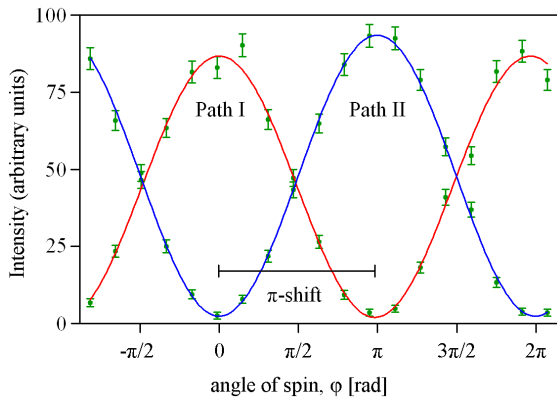


Fig. 37: Precession angle difference between IFM path I with Mu-metal tube and path II after adjustment to π {measured: $(0.985 \pm 0.047)\pi$ }.

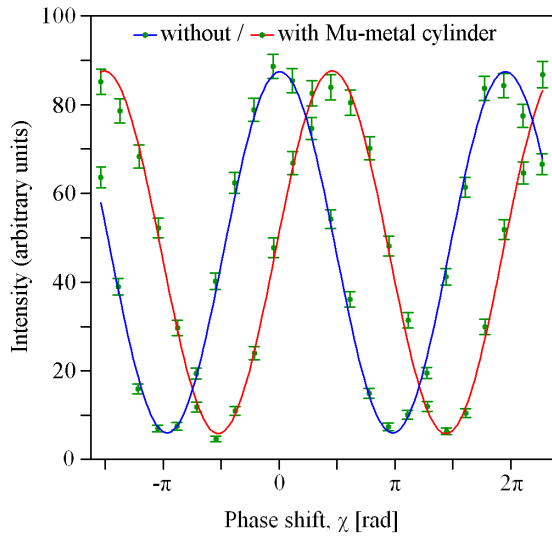


Fig. 38: Interferogram with the Mu-metal tube. The contrast-loss due to the tube is fairly low: without and with the tube the contrast was 0.8758 ± 0.0131 and 0.8754 ± 0.0131 , respectively.

3.3.6. Iron rings

A local guide field shielding similar to the Mu-metal tube described in Sec. 3.3.5 can be made by iron rings placed successively in a row, as shown in Fig. 41. The advantage of such consecutive rings compared to a continuous tube may be in lesser direction changes of the field inside and around the shielding, thus lowering the chance that spin fails to follow the field adiabatically. At the time when this Larmor decelerator should be tested the TRIGA reactor at the Atominstitut was shut down due to maintenance, therefore only magnetic field measurements and an iron powder test were carried out. For the tests we used demagnetized iron wire with thickness of 0.3mm, bent to circular shape giving rings of 24mm diameter. We applied a 10G field while the number of rings and the distance between them was varied. We measured the field in the center of each ring with a Hall effect magnetometer. In the first measurements we used 5 rings and aligned them once with 7mm and once with 8mm distances. The results are plotted in Fig. 39. Here, we can see that, though in the former case we obtain a shorter shielding, the field inside the shielding is more decreased than in the latter case.

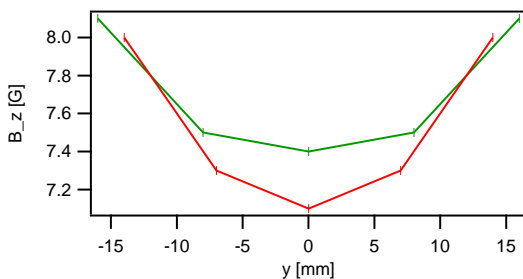


Fig. 39: Field measurement inside iron rings placed successively in a row. Shieldings using 5 rings with 7mm distances (28mm long shielding, red curve) and with 8mm distances (32mm long shielding, green curve) were compared. Though the former shielding is shorter, its shielding effect is stronger.

In the following measurements the number of the rings was varied while the length of the shielding was in each case 28mm. The results are plotted in Fig. 40. As we can see, the shielding effect increases significantly with the number of the rings.

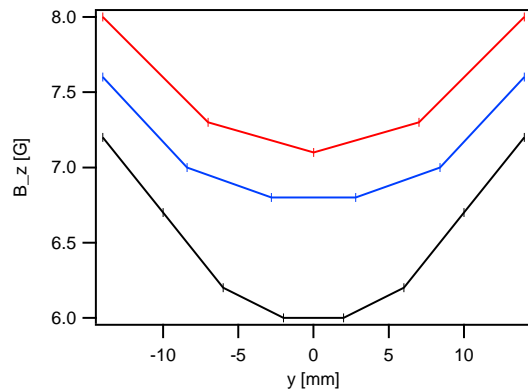


Fig. 40: Plot of field measurement inside iron rings placed successively in a row. The shieldings each had a length of 28mm and consisted of 5 rings (red curve), 6 rings (blue curve), and 8 rings (black curve).

The iron powder test was made with the shielding with 28mm length consisting of 8 rings, which is shown in Fig. 41. From this test the direction distortion of the field in dependence of position can be seen. It is not known how much these direction distortions may jeopardize adiabaticity, which also depends on the strength of the field, on the aperture of the neutron beam (the smaller the better), and on the position of the neutron beam, whose axis should ideally coincide with the axis of the shielding.

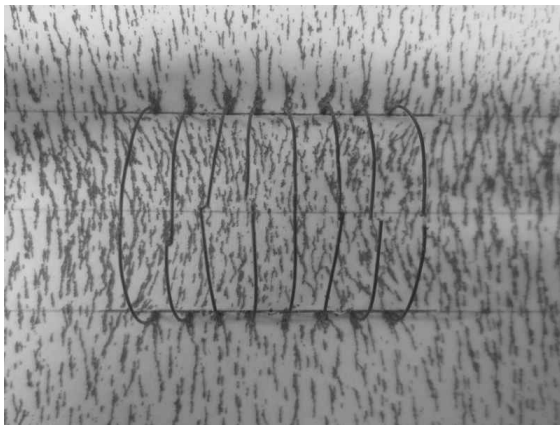


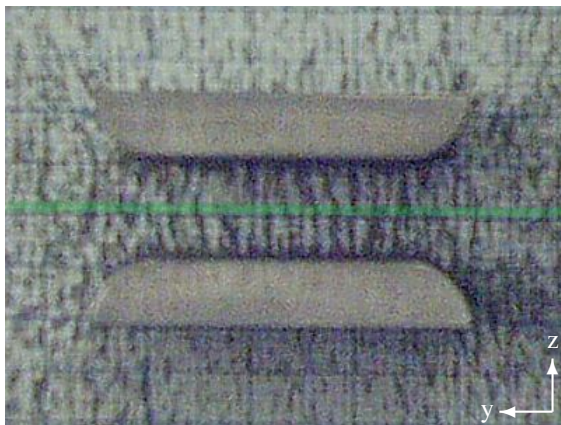
Fig. 41: Picture of the iron powder test of a 28mm long shielding consisting of 8 rings with 24mm diameter. The direction change of the field between two points can be seen, which, in consideration of further relevant parameters (field strength, beam aperture, etc.), may allow a rough estimation whether the beam would follow the field sufficiently adiabatically.

The adjustment of the shielding effect of the iron rings can be done similarly as in the case of the Mu-metal tube. The Larmor precession retardation can be adjusted by the number, diameter, and distance of the rings, which affect shielding similarly as length and diameter variations in case of the Mu-metal tube. Also in the case of the iron rings, the simplest method of final precession retardation adjustment in the experiment is the adjustment of the guide field strength, after the appropriate diameter, number, and

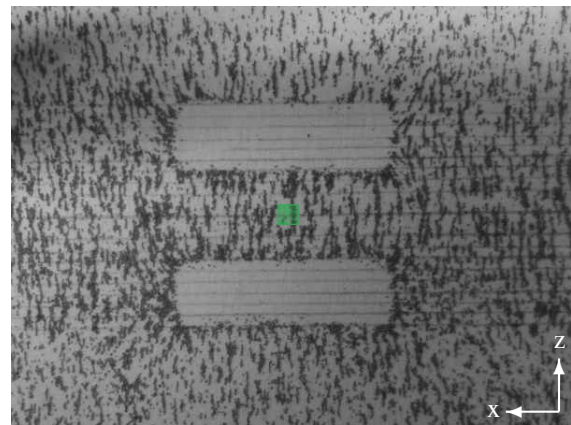
distance of the rings has been determined to yield the desired precession retardation in the range of the intended guide field strength. In principle, the precession retardation is linearly correlated with the strength of the guide field with coincidence of zero field strength and zero precession retardation (provided that the shielding material has no remanence magnetization and has not reached magnetic saturation). The 28mm long shielding made of 8 rings with 24mm diameter should achieve a precession retardation of π at a field strength of $\sim 20\text{G}$.

3.3.7. Iron pole pieces

Passive Larmor precession manipulators can not only be decelerators, but also accelerators can be realized with passive devices. A passive Larmor accelerator that is suitable for our purposes can be realized by two iron pole pieces placed parallel above and below the beam, as shown in Fig. 42. These pole pieces have no own magnetic field but gather the beam line guide field from their surrounding area and concentrate it in the gap between them, where the beam goes through, i.e., they increase the magnetic field in a region along the beam by weakening the field in a region where the beam does not pass.



(a) Side view.



(b) Front view (image plane perpendicular to beam).

Fig. 42: Iron pole pieces above and below the neutron beam axis. The beam axis is indicated by the green line in (a) and dot in (b). In these pictures the distortion of the guide field around the pole pieces is made visible by iron powder. The pictures show no obvious direction changes of the field in the middle region of the gap, which suggests that the field in the gap and at the entrances of the gap is sufficiently homogeneous.

For our tests we have chosen demagnetized cuboidal iron pieces with 6mm thickness in direction of the field and 20mm width in direction perpendicular to the field and the beam. These two parameters, together

with the distance between the two pole pieces, completely determine the amplification factor by which the field strength is increased between the pole pieces. The length of the pieces in direction of the beam can be varied without having effect on this amplification factor, because the relevant additional field in the gap between the pieces is gained and diverted from the region that goes parallel next to the beam. For distances of 8, 9, and 10mm between the pieces we have measured a field strength amplification factor of 1.53, 1.49, and 1.45, respectively. A typical field profile has been determined by measurement in a 10G field for two 50x20x6mm pieces with a 9mm gap between them, the results being plotted in Fig. 43. No changes in the field strength could be measured when the sensor was moved along the z-direction (direction of the field) in the gap between the two pieces from one piece to the other. This means that the beam aperture in the z-direction may practically fill out the whole gap (with rounded edges at the entrances of the pole pieces, by the way). In the horizontal direction perpendicular to the pole pieces' length axis in the first 5mm next to this axis the field is homogeneous within 0.7% (average of ten measurements), which allows for a beam aperture width of 10mm.

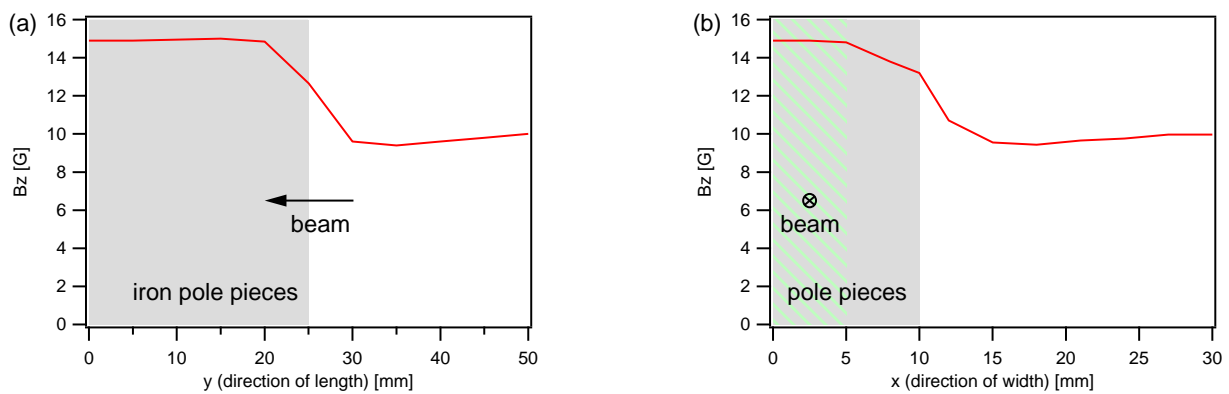


Fig. 43: Profiles of the field in the gap between the iron pole pieces. The 0-position is the corresponding symmetry plane of the pole pieces. Plot (a) shows the field profile in direction of the beam. The field amplification factor is 1.49. Plot (b) shows the field profile perpendicular to the beam and to the field. The 10mm-position marks the edges of the pieces on one side and the sufficiently homogeneous region of the field for the beam to go through is marked by the green dashed region.

At ILL we used iron pole pieces with size 34x20x6mm with a gap of 9mm between them and rounded off edges at the beam entrances. We analyzed the homogeneity of the field around these pole pieces with iron powder. The pictures are shown in Fig. 42. These results suggest that in the gap between the pole pieces and at their entrances there are no obvious direction changes of the field along the way of the beam. Sudden direction changes of the field are visible only in the vicinity of the pole pieces' edges, which direction

changes however could be smoothed by rounding off the edges, as has been done at the entrances.

Just as in the case of the other passive Larmor precession manipulators, also the correlation between the Larmor precession advance due to the iron pole pieces and the strength of the guide field is linear (saturation is certainly not reached at the field strengths we work with) with the precession advance being zero if the guide field is zero (provided the pole pieces have no remanence magnetization).

The pole pieces were also tested at the perfect-crystal neutron optics beam line S18 at ILL. The pole pieces were placed in path I of the IFM and the spin precession angle difference between path I and II was adjusted to be $(1.003 \pm 0.055)\pi$, which value sufficiently approximates π and was achieved at a measured guide field of 21.54G. The result of this measurement is plotted in Fig. 44. Also interferograms (phase shifter scans) were recorded: the average contrasts without and with the pole pieces were 0.7362 ± 0.0025 (average of 6 measurements) and 0.7388 ± 0.0095 (average of 14 measurements), respectively, i.e., the pole pieces caused no significant contrast loss.

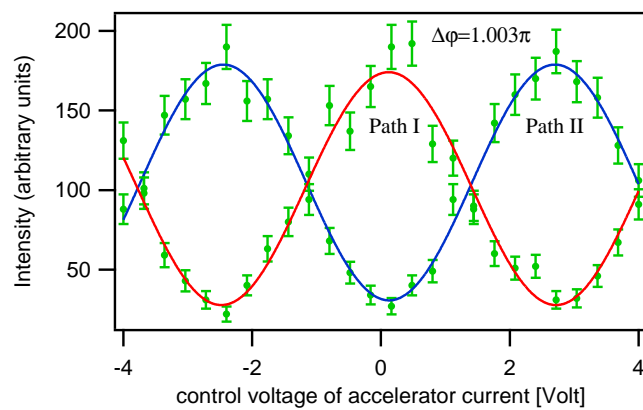


Fig. 44: Measurement of precession angle difference between path I and II in the IFM (with the iron pole pieces in path I) after adjustment to π {measured: $(1.003 \pm 0.055)\pi$ }.

4. EXPERIMENT 1: VIOLATION OF A BELL-LIKE INEQUALITY

4.1. Background of the study

It was Einstein, Podolsky, and Rosen (EPR) [Einstein et al., 1935] and afterwards Bell [Bell, 1964] who shed light on the non-local properties between subsystems in quantum mechanics. In particular, EPR argued that quantum mechanics is not a complete theory in the sense that it is not consistent with the joint assumption of locality and reality. Bell showed that local hidden variable theories (LHVTs) satisfy some inequalities that are violated by quantum mechanics: Bell's inequalities [Bell, 1964] are constraints imposed by LHVTs on the values of some specific linear combinations of the averages of the results of spacelike separated measurements. Experimental violations of Bell's inequalities on bipartite systems have been observed by using various quantum systems, e.g., photons [Aspect et al., 1981, Aspect et al., 1982a, Aspect et al., 1982b, Weihs et al., 1998], neutrons [Hasegawa et al., 2003], or atoms [Matsukevich et al., 2008], suggesting that LHVTs are not consistent with observations. LHVTs are a subset of a larger class of hidden-variable theories, known as noncontextual hidden-variable theories (NCHVTs) [Mermin, 1993, Basu et al., 2001]. By definition, NCHVTs assume that the result of a measurement of an observable is predetermined and independent of a previous or simultaneous measurement of any other compatible (i.e., commensurable) observable.

Quantum mechanical peculiarity is not limited to space-like separated systems, but is also found in measurements of a single-particle system. Since the first observation of neutron self-interference [Rauch et al., 1974], neutron optical experiments have been serving as an established method for investigating the foundations of quantum mechanics. In particular, neutron interferometry allows the observation of quantum mechanical phenomena on a macroscopic scale [Rauch and Werner, 2000]. While lots of experimental tests of the violation of Bell's inequalities have been made with correlated photon pairs, also a single-neutron system becomes a more and more interesting subject for such tests [Hasegawa et al., 2003, Sponar et al., 2010a,b]. In the following, we demonstrate the violation of a Bell-like inequality on the basis of a single-neutron interferometer (IFM) experiment that is an improved version of the previous experiment [Hasegawa et al., 2003]. The entanglement is accomplished between different degrees of freedom of the neutron, in this case between the spinor part and the spatial part of the neutron's wave function. Spin-1/2 particles, like neutrons, are described by a tensor product Hilbert space $H = H_s \otimes H_p$, where H_s and H_p are disconnected Hilbert spaces corresponding to the spinor and the spatial wave function, respectively. Observables of the spinor part commute with those of the spatial part, which justifies the derivation of a Bell-like inequality, according to the NCHVTs. The experiment consists of joint measurements of commuting observables of

single neutrons in an appropriately generated entangled (nonfactorizable) state. The new method to generate spin-path entanglement in an IFM, described in Sec. 3.3.3, and the newly developed Larmor decelerator, described in Sec. 3.3.5, lead to lower decoherence rate, resulting in higher contrast of the interference patterns: a larger violation than in the previous experiment [Hasegawa et al., 2003] has been observed.

4.2. Theory

In the IFM experiment described here with polarized neutrons the total wave function consists of the entanglement between the spatial part and the spinor part [Sakurai, 1994]. The normalized total wave function $|\Psi\rangle$ can be written as a Bell-like state $|\Psi\rangle = \frac{1}{\sqrt{2}}(|\downarrow\rangle \otimes |\text{I}\rangle + |\uparrow\rangle \otimes |\text{II}\rangle)$, where $|\uparrow\rangle$ and $|\downarrow\rangle$ denote the up- and down-spin states and $|\text{I}\rangle$ and $|\text{II}\rangle$ denote the two beam paths in the IFM.

The expectation value for the joint measurement of the spin state and the path is given by

$$E(\alpha, \chi) = \langle \Psi | \hat{P}^s(\alpha) \cdot \hat{P}^p(\chi) | \Psi \rangle = \langle \Psi | [\hat{P}_{\alpha;+1}^s - \hat{P}_{\alpha;-1}^s] \times [\hat{P}_{\chi;+1}^p - \hat{P}_{\chi;-1}^p] | \Psi \rangle, \quad (35)$$

where $\hat{P}^s(\alpha)$ and $\hat{P}^p(\chi)$ are observables for the spin and the path, respectively, and are decomposed by the projection operators $\hat{P}_{\alpha;\pm 1}^s$ and $\hat{P}_{\chi;\pm 1}^p$, which project the spin onto orthogonal spin states $\frac{1}{\sqrt{2}}(|\uparrow\rangle \pm e^{i\alpha}|\downarrow\rangle)$ and the path onto orthogonal path states $\frac{1}{\sqrt{2}}(|\text{I}\rangle \pm e^{i\chi}|\text{II}\rangle)$, respectively. (These projection operators and the above expectation value correspond to $P'_\pm(\mathbf{a})$, $P'_\pm(\mathbf{b})$, and $E'(\mathbf{a}, \mathbf{b})$ in the conventional EPR argument [Aspect, 1984]). It should be emphasized that \hat{P}^s and \hat{P}^p operate in different Hilbert spaces and therefore commute with each other. The parameters α and χ are experimentally varied by polarization analysis of the generated Bell-like state and by phase shift, respectively.

A Bell-like inequality for a single-neutron experiment is given in terms of expectation values $E(\alpha, \chi)$ by [Basu et al., 2001]:

$$-2 \leq S \leq 2, \quad \text{where } S := E(\alpha_1, \chi_1) + E(\alpha_1, \chi_2) + E(\alpha_2, \chi_1) - E(\alpha_2, \chi_2). \quad (36)$$

Expectation values $E(\alpha, \chi)$ in our experiment are determined from a combination of count rates (numbers of detected neutrons) at appropriate values of α and χ :

$$E(\alpha, \chi) = \frac{N(\alpha, \chi) + N(\alpha + \pi, \chi + \pi) - N(\alpha, \chi + \pi) - N(\alpha + \pi, \chi)}{N(\alpha, \chi) + N(\alpha + \pi, \chi + \pi) + N(\alpha, \chi + \pi) + N(\alpha + \pi, \chi)}, \quad (37)$$

where $N(\alpha_j, \chi_k) = \langle \Psi | \hat{P}_{\alpha_j;+1}^s \cdot \hat{P}_{\chi_k;+1}^p | \Psi \rangle$ is the count rate at spin rotation α_j and phase shift χ_k . The expectation values of joint measurements are yielded by count rates of successive measurements by one detector at different settings of α and χ .

Quantum theory predicts a sinusoidal behavior for the count rate, according to $N(\alpha, \chi) = \frac{1}{2}[1 + \cos(\alpha + \chi)]$, and a similar behavior is also shown by the resulting expectation value: $E(\alpha, \chi) =$

$\cos(\alpha + \chi)$. According to this relation of E with α and χ , a violation of the Bell-like inequality occurs for various sets of α and χ values. In particular, the theoretical maximum violation, given by $S = 2\sqrt{2} \approx 2.828 \not\leq 2$, is realized by the set $\alpha_1 = 0$, $\alpha_2 = \pi/2$, $\chi_1 = -\pi/4$, and $\chi_2 = \pi/4$.

In a real experiment there are always unavoidable misalignments of optical components, imperfect quality of polarization and interference, environmental disturbances and so on. All of these reduce the visibility of the sinusoidal behavior of N , which is characterized by the so-called contrast of the intensity oscillation. The measured value of S reduces in proportion to these contrasts. The mean contrast must exceed $\sqrt{2}/2$ ($\approx 70.7\%$) in order to demonstrate the violation of the Bell-like inequality.

Our experimental demonstration of the violation of a Bell-like inequality by means of interferometry with polarized neutrons consists of two steps: (i) generation of the Bell-like neutron state that we have already defined in Sec. 3.3.1 by

$$|\Psi\rangle = \frac{1}{\sqrt{2}} (|\leftarrow\rangle \otimes |\text{I}\rangle + |\rightarrow\rangle \otimes |\text{II}\rangle), \quad (38)$$

where $|\leftarrow\rangle = \frac{1}{\sqrt{2}} (|\uparrow\rangle + e^{i\alpha} |\downarrow\rangle)$ and $|\rightarrow\rangle = \frac{1}{\sqrt{2}} (|\uparrow\rangle - e^{i\alpha} |\downarrow\rangle)$, with $|\uparrow\rangle$ and $|\downarrow\rangle$ representing up and down spin states, respectively, which are parallel and anti-parallel to the vertical magnetic guide field, and (ii) manipulation of this state and subsequent projection, where the parameters α and χ are adjusted to select neutrons with certain properties for detection by polarization analysis in the O-beam to obtain correlation coefficients. A schematic view of the experimental setup is shown in Fig. 45, which we discuss in detail later.

4.3. Interferometer experiment to violate a Bell-like inequality

The violation of the Bell-like inequality (36) in interferometry with polarized neutrons requires the generation of a Bell-like neutron state (38) and manipulation of this state by adjusting α and χ to select neutrons with certain properties by polarization analysis for detection in the O-beam to obtain correlation coefficients.

The experiment [Hasegawa and Erdős, 2011] was carried out at the perfect-crystal neutron optics beam line S18 at the high flux reactor of the Institute Laue-Langevin (ILL) [Kroupa et al., 2000]. The setup is depicted in Fig. 45, photographs are shown in Fig. 46. By means of a silicon perfect-crystal monochromator a neutron beam with a mean wavelength of $\lambda_0 = 1.92\text{\AA}$ ($\Delta\lambda/\lambda_0 \approx 0.02$) was selected, corresponding to a neutron velocity of $\sim 2060\text{m/s}$. Then the beam was polarized vertically by magnetic-prism refractions. After this the beam, with an aperture of $3\times 3\text{mm}^2$, entered a triple-Laue (LLL) IFM, which was adjusted to employ a 220 reflection. A parallel-sided aluminium plate was used as a phase shifter, varying χ . A pair

of water-cooled Helmholtz coils produced a fairly uniform magnetic guide field $B_0\hat{z}$ over the region of the polarized neutron beam. A supermirror in the O-beam together with a DC spin flipper (DC2) movable along the beam axis (y-axis), to adjust α (when necessary), enabled the selection of neutrons in dependence of their polarization directions for detection.

In the experimental setup, shown in Fig. 45, we applied our new, two-step spin preparation method, introduced in Sec. 3.3.3, to generate the entangled state (38). After the polarizer (vertically polarizing the incident neutron beam), the spin up-polarized beam was manipulated by a $\pi/2$ DC spin flipper (DC1), which changed the spinor from $|\uparrow\rangle$ to $|\rightarrow\rangle$, before the beam entered a silicon perfect crystal triple-Laue (LLL) IFM, where it split into two beam paths I and II. In path I of the IFM the newly developed Mu-metal tube was inserted to decrease Larmor precession speed relative to that in path II, so that the spinor in path I was changed from $|\rightarrow\rangle$ to $|\leftarrow\rangle$. The so generated entangled state was then manipulated by a phase shifter, varying χ , and a DC spin flipper (DC2), adjusting the spinor rotation angle α so that neutrons with defined polarization direction were selected by a supermirror (spin-analyzer) in the O-beam for detection. The numbers of neutrons were counted, yielding $N(\alpha, \chi)$.

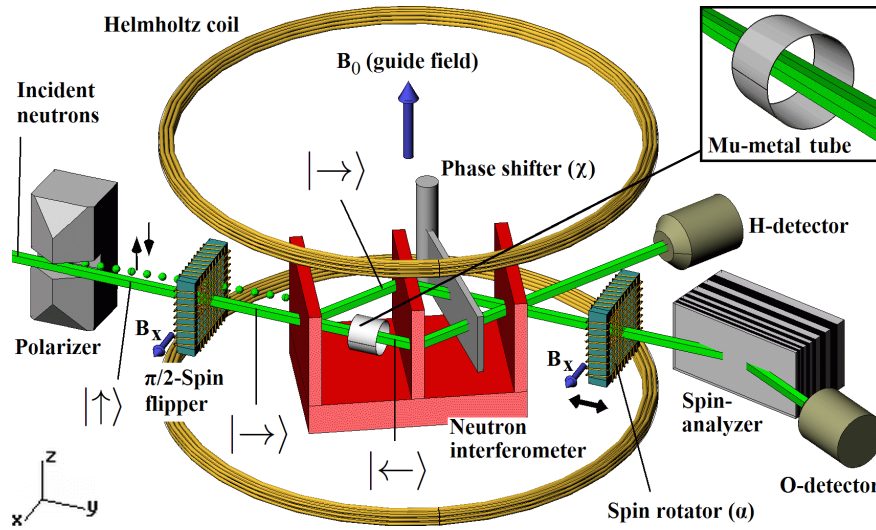


Fig. 45: Experimental setup for the improved measurement of the violation of a Bell-like inequality using the new, two-step spin preparation method described in Sec. 3.3.3 and the Mu-metal tube whose development was described in Sec. 3.3.5.

The innovation in this experiment [Hasegawa and Erdős, 2011] compared to the previous one [Hasegawa et al., 2003] was the decomposition of spin preparation (detailed description is given in Sec. 3.3.3) into (i) a $\pi/2$ spin flip before the IFM, requiring non-adiabatic direction changes of the mag-

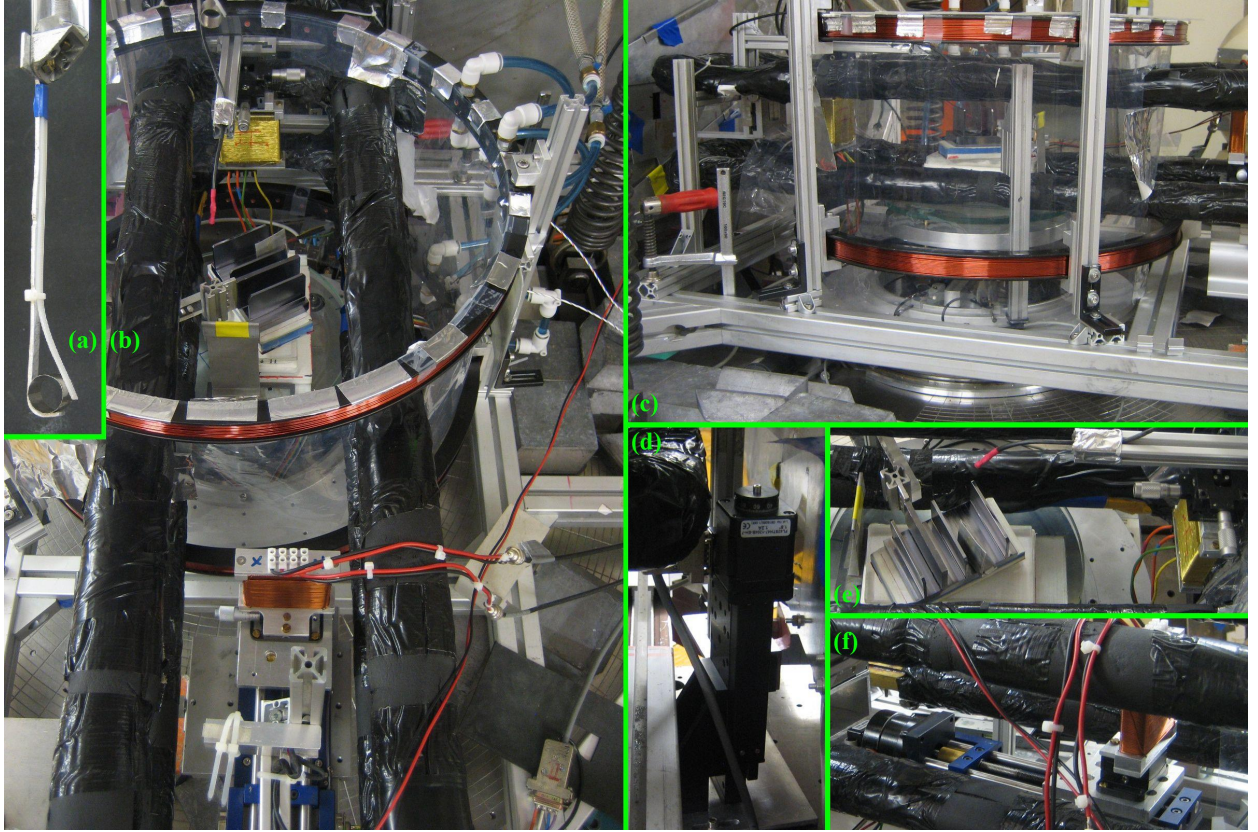


Fig. 46: Photographs of the experimental setup: (a) Mu-metal tube and its holder (lifted out of the IFM), (b) top view of beam line (beam goes from top to bottom), (c) side view of beam line (beam goes from left to right), (d) mechanism to adjust the aperture/beam position, (e) IFM, phase shifter, temperature sensor (red) above IFM, and DC1, and (f) DC2 together with mechanism for automated y-position adjustment.

netic field for the neutrons, and (ii) subsequent Larmor precession phase change by π of the two IFM paths relative to each other, so that no field direction changes were required in the IFM but only changes in the field strength while keeping adiabaticity. For step (i) we used a DC flipper made of aluminium wire to reduce small-angle scattering. For step (ii) of spin preparation a new optical element, the Mu-metal tube described in Sec. 3.3.5, was placed in path I of the IFM. The dimensions of the tube were $l = 13.0\text{mm}$ and $d = 15.5\text{mm}$ with wall thickness of 0.1mm . The azimuthal angle between the spins in path I and II after adjustment by means of the guide field's strength was measured to be $(0.985 \pm 0.047)\pi$. The guide field, whose value after adjustment was $B_0 = 21.9\text{G}$ around the IFM, was produced by the water cooled rectangular Helmholtz coils (while the circular Helmholtz coils did not operate). The distance for a full circle of Larmor precession was $\sim 32\text{mm}$, according to formula (34). After adjusting the beam cross section and the incident position of the IFM, we achieved a contrast of 87.2-89.5%. A typical interferogram is plotted in Fig. 47.

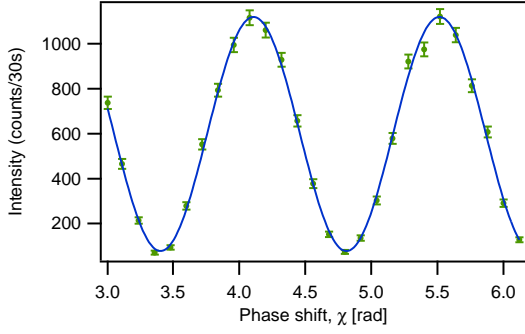


Fig. 47: Typical intensity oscillation obtained with the empty IFM. The contrast reached 87.2-89.5%.

4.3.1. Adjustments

The flip ratio of a DC spin flipper is determined by consecutive adjustments of the currents for the flipper's magnetic field along the x -axis and the z -axis until the spin of most neutrons is flipped and hence no significant changes of the currents are indicated by further scans. The flip ratio of DC1 was measured to be 22.8 and the x -current for the $\pi/2$ flip mode was found to be 0.72A, as shown in the plot in Fig. 48. ($\pi/2$ flip mode means that a fifty-fifty superposition of an up- and down-spin state is produced for each neutron). The flip ratio of DC2 was measured to be 22.1 and the x -currents for the π , $\pi/2$, and $-\pi/2$ flip modes were found at 1.21A, 0.63A, and -0.62A, respectively, as shown in the plot in Fig. 49.

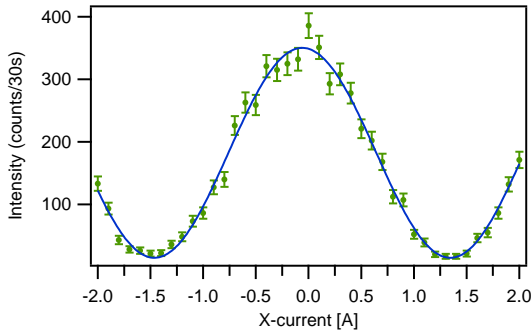


Fig. 48: X-current scan of DC1 after adjustment. The x -current for the $\pi/2$ flip mode was found at 0.72A.

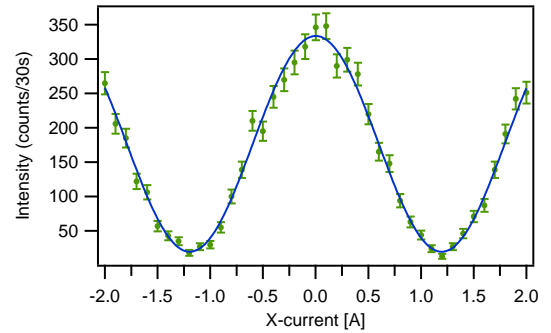


Fig. 49: X-current scan of DC2 after adjustment. The x -currents for the π , $\pi/2$, and $-\pi/2$ flip modes were 1.21A, 0.63A, and -0.62A, respectively.

Next, the Mu-metal tube was placed in path I of the IFM. For the position adjustment of the tube a cadmium aperture was attached to the tube's holder, letting the neutrons pass through at the tube's central axis. Then the phase difference in Larmor precession between the beam paths I and II due to the Mu-metal tube was adjusted. For this purpose both DC1 and DC2 were in $\pi/2$ -flip mode and the y -position of DC2

was varied, which in principle corresponds to the setup depicted in Fig. 28. Two consecutive such scans, one with beam path II one with path I blocked, indicated the phase difference of the two oscillations, which was adjusted to π . The final adjustment scans achieved $(0.985 \pm 0.047)\pi$. The measurements are plotted in Fig. 50. From the same data the total flip ratio of the beam line was determined to be ~ 12.5 , which is mainly due to the flip ratios of DC1 and DC2.

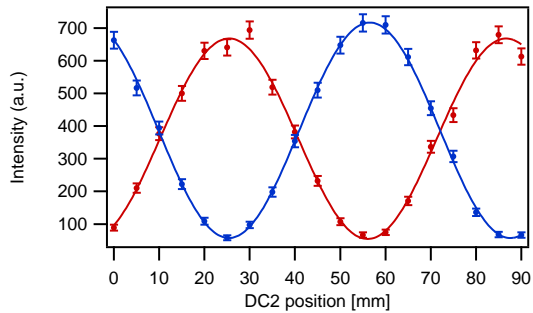


Fig. 50: Measurement of the phase difference in Larmor precession between path I (red curve) with the Mu-metal tube and path II (blue curve) after adjustment (DC2 was moved step-by-step away from the IFM). The phase difference was $(0.985 \pm 0.047)\pi$ (at $B_0 = 21.9\text{G}$).

There is a relation between the contrast in the O-beam and the y -position of DC2 if DC2 is in $\pi/2$ or $-\pi/2$ flip mode, namely, the O-contrast takes a maximum followed by a minimum, and so on, in accordance with Larmor precession in the beam line guide field, as the position of DC2 becomes further away from the IFM. This can be well seen with the measurements plotted in Fig. 51, where the contrast is plotted in dependence of the y -position of DC2. Unlike this, if DC2 performs a zero or a π flip, the contrast remains constant under variation of the y -position of DC2. Therefore, a position of DC2 had to be found at that the O-contrast takes a maximum for the half-integer- π flips. The plot in Fig. 51 gives an overview of the contrast over a region (of DC2's y -position) of 70mm, and Fig. 52 focuses around the maximum that we have chosen for DC2's final y -position. The results were fitted with a $|\sin|$ function. On the basis of these contrast scans, also a correlation with the intensity scans in Fig. 50 was found, namely, the curves of these two types of measurements are shifted relative to each other by $\pi/2$, i.e., the maxima of the O-contrast coincide with the points of inflection of the sine waves in Fig. 50, which correspond to the crossing points of the two waves (after offset and amplitude scaling). Since a direct scan of contrasts, as in Fig. 51, takes ~ 12 hours, while the intensity scans, as in Fig. 50, only take ~ 40 minutes, it seems to be more practicable to find a maximum of the O-contrast by means of the latter kind of measurements.

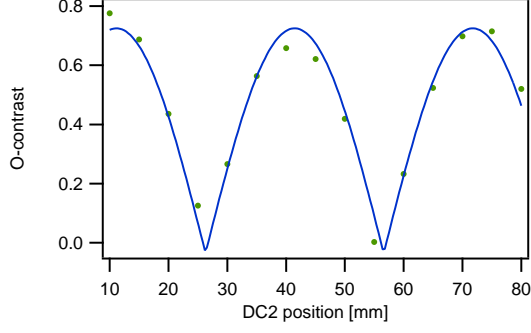


Fig. 51: O-contrast vs. y -position of DC2. This dependence of the O-contrast reflects the fact that the angle between the spin during precession in the guide field and the direction of spin analysis changes according to the position of DC2.

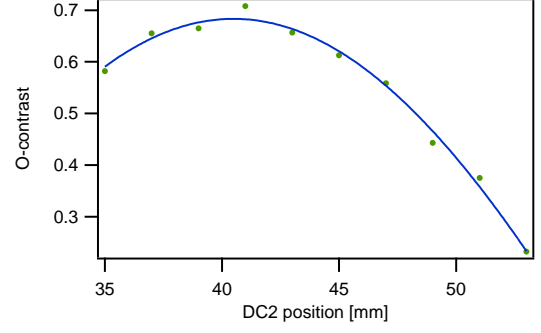


Fig. 52: O-contrast vs. y -position of DC2, scanned around the maximum we have chosen for DC2's final position.

Some factors degrading the experiment were (i) the small-angle scattering at DC1, which probably mainly caused the relatively low polarization of the beam line by partially mixing spin-up and spin-down neutrons previously separated by magnetic-prism refractions and (ii) the fact that the Mu-metal tube caused an inhomogeneity of the field in the neighboring beam path, which, according to the previous polarimeter measurements in Sec. 3.3.5, reduced the degree of polarization of the 3mm wide beam, expanded to ~ 5 mm after the first IFM plate, by a factor of $\sim \cos(0.05\pi)$, i.e., ~ 0.988 .

4.3.2. Measurement and data-analysis

The generated Bell-like state has to be manipulated appropriately before its detection. In this stage the relative phase χ between paths I and II in the IFM and the spinor angle α , selecting neutrons with certain polarization, are tuned. A maximum violation of the Bell-like inequality is expected for $\alpha = 0, \pi, \pi/2$, and $-\pi/2$ (equivalent to $\pi/2 + \pi$). We repeated the same measurements seven times to reduce statistical errors, which gave seven sets of four contrast (phase shifter) scans. The mean contrasts for these α values, under variation of the relative phase shift χ , were 0.8149 ± 0.0052 , 0.8597 ± 0.0050 , 0.7168 ± 0.0050 , and 0.7279 ± 0.0049 , respectively. At $\alpha = \pi/2$ and $\alpha = -\pi/2$ the contrasts were significantly lower than at $\alpha = 0$ and $\alpha = \pi$, which is mainly due to the depolarizing effect of DC1. We achieved an overall mean contrast of 0.7784 ± 0.0025 , which significantly exceeds the one achieved in the previous experiment [Hasegawa et al., 2003]. After fitting the measured count rates to sinusoidal dependence by the least squares method,

the obtained fit parameters served as the basis to calculate the expectation values according to Eq. (37). A typical set of the measured intensity oscillations is shown in Fig. 53.

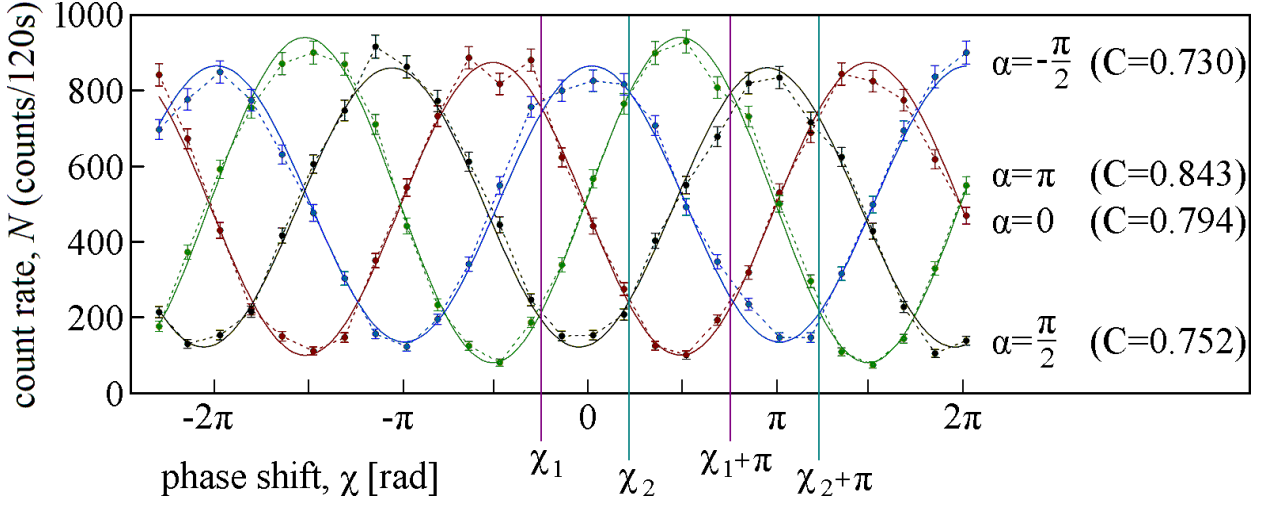


Fig. 53: Typical set of sinusoidal intensity oscillations of the count rates $N(\alpha, \chi)$ at spinor rotation angles $\alpha = 0, \pi, \pi/2$, and $-\pi/2$ with indication of the corresponding contrasts C under variation of χ . The maximum value of S was found for this set at $\chi_1 = -0.25\pi$ and $\chi_2 = 0.22\pi$, indicated by the vertical lines at these and the corresponding π -shifted values. Based on seven such count rate sets, our final maximum value for S is $2.2025 \pm 0.0071 \not\leq 2$, which clearly violates the Bell-like inequality.

For each oscillation curve the raw data was fitted with the sinusoidal function $A + B \sin(cx + D)$. In the first round of fitting, the mean value of c for each set was determined. The four c values of the curves of a set differ by not more than $\sim 1\%$, and the errors of the mean values for c are not larger than 0.78% . With the mean values of c fixed, in the second fitting round the other fit parameters were obtained. These parameters and the contrasts together with their errors are given for each oscillation set in Tab. II. (Simultaneous fitting of all four oscillation curves of a set, with a common parameter for c , would have been disproportionately demanding, compared to the potential benefit for the result, e.g., by reducing the errors of the fit parameters, therefore we decided to accept the insignificant loss of accuracy due to our method of fitting).

α	A	B	D	O-contr.	H-contr.
0	444.51 ± 4.21	373.67 ± 5.20	3.5505 ± 0.0132	0.8406 ± 0.0142	0.0204 ± 0.0027
π	472.78 ± 4.13	414.05 ± 5.02	0.2190 ± 0.0127	0.8758 ± 0.0131	0.0205 ± 0.0027
$\pi/2$	451.59 ± 3.99	308.73 ± 5.21	1.7692 ± 0.0182	0.6836 ± 0.0130	0.0228 ± 0.0027
$-\pi/2$	469.63 ± 4.33	343.54 ± 5.49	5.2155 ± 0.0157	0.7315 ± 0.0135	0.0211 ± 0.0027
0	433.13 ± 4.18	370.24 ± 5.04	3.7335 ± 0.0133	0.8548 ± 0.0143	0.0247 ± 0.0027
π	464.18 ± 4.06	409.89 ± 4.94	0.3845 ± 0.0126	0.8830 ± 0.0132	0.0237 ± 0.0027
$\pi/2$	446.24 ± 3.98	302.04 ± 5.29	1.9520 ± 0.0182	0.6768 ± 0.0133	0.0226 ± 0.0027
$-\pi/2$	462.04 ± 4.28	343.06 ± 5.45	5.3400 ± 0.0155	0.7425 ± 0.0137	0.0163 ± 0.0027
0	432.15 ± 4.15	359.09 ± 5.13	3.6281 ± 0.0137	0.8309 ± 0.0143	0.0182 ± 0.0027
π	456.65 ± 4.05	395.39 ± 4.00	0.2391 ± 0.0130	0.8658 ± 0.0134	0.0161 ± 0.0027
$\pi/2$	442.64 ± 3.96	294.52 ± 5.21	1.8257 ± 0.0189	0.6654 ± 0.0132	0.0182 ± 0.0027
$-\pi/2$	456.54 ± 4.26	339.76 ± 5.43	5.2795 ± 0.0155	0.7442 ± 0.0138	0.0198 ± 0.0027
0	467.84 ± 4.15	367.20 ± 5.41	2.5784 ± 0.0143	0.7849 ± 0.0135	0.0204 ± 0.0025
π	520.99 ± 4.51	436.09 ± 5.64	5.6226 ± 0.0123	0.8370 ± 0.0130	0.0191 ± 0.0025
$\pi/2$	503.06 ± 4.53	380.00 ± 5.58	4.2596 ± 0.0147	0.7574 ± 0.0130	0.0254 ± 0.0025
$-\pi/2$	483.28 ± 4.12	345.67 ± 5.32	0.8655 ± 0.0167	0.7153 ± 0.0126	0.0219 ± 0.0025
0	476.68 ± 4.14	377.00 ± 5.30	2.2706 ± 0.0145	0.7909 ± 0.0131	0.0046 ± 0.0025
π	522.09 ± 4.55	449.36 ± 5.56	5.3937 ± 0.0119	0.8607 ± 0.0130	0.0132 ± 0.0025
$\pi/2$	493.39 ± 4.45	368.85 ± 5.59	3.9514 ± 0.0150	0.7479 ± 0.0132	0.0050 ± 0.0025
$-\pi/2$	491.37 ± 4.18	356.42 ± 5.41	0.6156 ± 0.0161	0.7254 ± 0.0126	0.0121 ± 0.0025
0	484.15 ± 4.18	391.16 ± 5.36	2.3802 ± 0.0138	0.8079 ± 0.0131	0.0098 ± 0.0025
π	502.65 ± 4.46	428.65 ± 5.48	5.4677 ± 0.0122	0.8528 ± 0.0133	0.0076 ± 0.0025
$\pi/2$	490.79 ± 4.47	360.63 ± 5.61	4.0454 ± 0.0153	0.7348 ± 0.0132	0.0102 ± 0.0025
$-\pi/2$	491.31 ± 4.17	347.31 ± 5.41	0.7069 ± 0.0167	0.7069 ± 0.0125	0.0100 ± 0.0025
0	486.72 ± 4.21	386.67 ± 5.44	2.4664 ± 0.0139	0.7944 ± 0.0131	0.0185 ± 0.0025
π	509.89 ± 4.45	429.60 ± 5.57	5.6115 ± 0.0123	0.8425 ± 0.0132	0.0115 ± 0.0025
$\pi/2$	490.28 ± 4.44	368.81 ± 5.51	4.1643 ± 0.0151	0.7522 ± 0.0131	0.0103 ± 0.0025
$-\pi/2$	499.62 ± 4.20	364.69 ± 5.40	0.8076 ± 0.0160	0.7299 ± 0.0124	0.0095 ± 0.0025

TABLE II: Sets 1-7 (from top to bottom) of fit parameters and contrasts and their errors on basis of the measurement data. Set 7 is illustrated in Fig. 53. The average values for the fit parameter c of each set were 0.006042 ± 0.000046 , 0.006056 ± 0.000045 , 0.006006 ± 0.000046 , 0.006026 ± 0.000044 , 0.005988 ± 0.000043 , 0.006092 ± 0.000043 , 0.005925 ± 0.000043 , respectively.

The maximum value of S in Eq. (36) was calculated for each oscillation set from the fit parameters in Tab. II with Mathematica (by use of the command FindMaximum). The count rates $N(\alpha_j, \chi_k)$, which yield the expectation values according to Eq. (37), were taken from the four oscillation curves of a set: $N(\alpha_1, \dots)$ from the curve for $\alpha = 0$, $N(\alpha_1 + \pi, \dots)$ from the curve for $\alpha = \pi$, $N(\alpha_2, \dots)$ from the curve for $\alpha = \pi/2$, and $N(\alpha_2 + \pi, \dots)$ from the curve for $\alpha = -\pi/2$. The error of S was calculated by using the standard error-propagation formula

$$S^{\text{Err}} = \left[\left(\frac{\partial S}{\partial A_0} A_0^{\text{Err}} \right)^2 + \dots \right]^{1/2}. \quad (39)$$

For each intensity oscillation set the maximum value of S , the mean values of the O- and H-contrasts, and the difference of the relative phase shifts $|\chi_2 - \chi_1| = \Delta\chi$ at the maximum S value are represented in Tab. III.

set	S	$\Delta\chi$	average O-contr.	average H-contr.
1	2.2090 ± 0.0190	0.437π	0.7813 ± 0.0067	0.0212 ± 0.0013
2	2.2310 ± 0.0192	0.435π	0.7882 ± 0.0068	0.0218 ± 0.0014
3	2.1854 ± 0.0193	0.440π	0.7745 ± 0.0068	0.0181 ± 0.0014
4	2.1836 ± 0.0184	0.467π	0.7724 ± 0.0065	0.0217 ± 0.0013
5	2.2105 ± 0.0184	0.462π	0.7804 ± 0.0065	0.0086 ± 0.0012
6	2.1946 ± 0.0185	0.454π	0.7738 ± 0.0065	0.0094 ± 0.0012
7	2.2031 ± 0.0183	0.466π	0.7783 ± 0.0065	0.0124 ± 0.0012

TABLE III: The maximum value of S , difference of the relative phase shifts $\Delta\chi$, and mean values of the O- and H-contrasts for each oscillation set on basis of the parameters in Tab. II.

Our final value for S is given by the arithmetic mean of the seven maximum values from table III and the final error was calculated by the standard error-propagation formula from the errors of the seven S -values. (This error is to be preferred over the standard deviation of our seven S -values, because it is larger than the latter, namely 0.0071 vs. 0.0062 [Gränicher, 1996]). We obtained for $S \equiv E(\alpha_1, \chi_1) + E(\alpha_1, \chi_2) + E(\alpha_2, \chi_1) - E(\alpha_2, \chi_2)$ in the Bell-like inequality (36) a value of

$$S = 2.2025 \pm 0.0071 \not\leq 2, \quad (40)$$

where the mean value of the difference of the relative phase shifts $\Delta\chi$ was measured to be 0.451π . This violates the Bell-like inequality by ~ 29 standard deviations and so clearly confirms quantum contextuality. The deviation of our maximum value for S from the theoretical maximum value is mainly due to the lower than 100% contrast of the IFM, but also inaccuracies in the adjustment of optical elements and statistical errors reduced our maximum S -value. This experiment is reported in [Hasegawa and Erdős, 2011].

5. EXPERIMENT 2: GENERATION OF GHZ- AND W-LIKE NEUTRON STATES IN INTERFEROMETRY

5.1. Background of the study

Entanglement has been found in many distinct physical systems, e.g., photons, atoms, ions, neutrons, and even in quark-antiquark systems of the second and third generation (e.g. [Hiesmayr et al., 2012]). The simplest entanglement is achieved with a bipartite system, while multipartite entanglement can, e.g., be used for the study of quantum contextuality [Kochen and Specker, 1967, Peres, 1990, Mermin, 1990, Mermin, 1993]. A single-neutron system provides a well controllable three qubit system and therefore is perfectly suited to study the properties of tripartite entangled systems of matter-waves. We demonstrate multipartite entanglement by means of this system and open up a path to high precision tests of three qubit Hilbert spaces.

Most physical implementations of multipartite entangled systems explore only one kind of internal degree of freedom that is entangled to the same internal degree of freedom of other physically disjoint systems at different locations. Entanglement purely between degrees of freedom in a single quantum system is extensively studied by using neutron optical techniques in particular neutron interferometry [Rauch and Werner, 2000]. For tests of fundamental properties of quantum mechanics, intra-particle entanglement serves well.

5.2. Theory

Two famous examples of genuine multipartite entanglement, which have been shown to be very different in their nature (e.g. [Horodecki et al., 2001, Acin et al., 2001, Wocjan et al., 2005, Seevinck et al., 2008, Hiesmayr et al., 2009]), are the GHZ-state and the W-state (introduced in [Greenberger et al., 1989, Greenberger et al., 1990, Dür et al., 2000]). For three degrees of freedom these states are expressed by $|GHZ\rangle = \frac{1}{\sqrt{2}}(|000\rangle + |111\rangle)$ and $|W\rangle = \frac{1}{\sqrt{3}}(|100\rangle + |010\rangle + |001\rangle)$, both of them being non-biseparable. The difference between these two states is, e.g., their behavior under loss of one qubit: the remaining two qubits of the W-state are still entangled, whereas the GHZ-state becomes fully separable. Therefore, the W-state is considered to be more robust against decoherence than the GHZ-state. For these two states we present the experimental demonstration of production in the tripartite entangled neutron system via multipartite detection criteria. To detect multipartite entanglement, we adapt a specific technique from [Gabriel et al., 2010, Gühne and Seevinck, 2010, Huber et al., 2010]. In computational notation the GHZ- and W-states

read (a, b, c, d, e, \dots amplitudes to be determined)

$$|W\rangle = a \underbrace{|101\rangle}_{:=|w_1\rangle} + b e^{i\pi/2} \underbrace{|011\rangle}_{:=|w_2\rangle} + c \underbrace{|002\rangle}_{:=|w_3\rangle}, \quad (41)$$

$$|GHZ\rangle = d e^{i\pi/2} \underbrace{|101\rangle}_{:=|v_1\rangle} + e \underbrace{|010\rangle}_{:=|v_2\rangle}, \quad (42)$$

where the three subsystems in kets denote three different degrees of freedom of single neutrons. The first subsystem denotes the path in the interferometer (path degree of freedom), which we also denote as path I ($|I\rangle = |0\rangle$) and II ($|II\rangle = |1\rangle$), the second denotes the spin of the neutron (which can take the two values $\pm \frac{\hbar}{2}$ and we denote as $|\downarrow\rangle = |0\rangle$ and $|\uparrow\rangle = |1\rangle$) and the third subsystem refers to the total energy (potential energy in an applied magnetic field plus kinetic energy) of the neutron. The neutron can be at different total energy levels, denoted as $|E_0\rangle = |0\rangle$, $|E_0 - \hbar\omega\rangle = |1\rangle$ and $|E_0 - 2\hbar\omega\rangle = |2\rangle$.

A measure for the precision of state generation is provided by the fidelity [Uhlmann, 1976, Jozsa, 1994, Miszczak et al., 2009]

$$F = \left(\text{Tr} \sqrt{\sqrt{\rho_0} \rho \sqrt{\rho_0}} \right)^2, \quad (43)$$

where ρ_0 is the density matrix of the ideal state and ρ is the density matrix obtained in the experiment. The fidelity shows how close the generated state is to the ideal state, where in the case of perfect state generation $F = 1$. (Just to mention, there is also a definition of fidelity without the square [Nielsen and Chuang, 2000, Uhlmann, 2000]. With formula (43) we will obtain values between 0.95 and 0.99, which with the latter definition would be 0.97-0.99.)

For the detection of the two states we also employ two distinct nonlinear entanglement witnesses, which are optimally suited to detect GHZ- and W-like entanglement. The GHZ witness inequality employs a permutation operator Π_i , permuting the i^{th} subspace of the two copy Hilbert space, and reads

$$I_{GHZ} := |\langle v_2 | \rho | v_1 \rangle| - \sum_{i=1}^3 \sqrt{\langle v_2 v_1 | \Pi_i \rho^{\otimes 2} \Pi_i | v_2 v_1 \rangle} \leq 0. \quad (44)$$

This relation is satisfied for all biseparable states and maximally violated for the above defined GHZ-state (the value of maximal violation is 0.5). For the W-state we have the witness inequality

$$I_W := \sum_{i \neq j} |\langle w_i | \rho | w_j \rangle| - \sum_{i,j=1}^3 \sqrt{\langle w_i w_j | \Pi_i \rho^{\otimes 2} \Pi_i | w_i w_j \rangle} \leq 0. \quad (45)$$

This relation is again satisfied for all biseparable states and maximally violated for the above defined W-state (with $|w_i\rangle$ as defined in (41)); again the value of maximum violation is 0.5. Thus any violation of any of these two inequalities is a clear proof of the presence of genuine multipartite entanglement within the

system. To detect k -separability, we employ the following inequality, which is satisfied by all k -separable states [Gabriel et al., 2010]:

$$I_{k-sep}[\rho] := \sqrt{\langle \Phi | \rho^{\otimes 2} P_{total} | \Phi \rangle} - \sum_{\{\alpha\}} \left(\prod_{i=1}^k \langle \Phi | P_{\alpha_i}^\dagger \rho^{\otimes 2} P_{\alpha_i} | \Phi \rangle \right)^{\frac{1}{2k}} \leq 0, \quad (46)$$

where $|\Phi\rangle = |\phi_1\rangle \otimes |\phi_2\rangle$ is an arbitrary fully separable state, P_{α_i} is a permutation operator permuting the α_i -th elements of $|\phi_1\rangle$ and $|\phi_2\rangle$, P_{total} wholly permutes the $|\phi_i\rangle$, and the sum runs over all k -partitions $\{\alpha\}$.

5.3. Experimental generation of W- and GHZ-like states

The experiment of Erdős et al. [Erdős et al., 2013] was carried out at the perfect-crystal neutron optics beam line S18 at the high flux reactor of the Institute Laue-Langevin (ILL) [Kroupa et al., 2000]. The setup is depicted in Fig. 54. We used the newly developed RF spin flipper equipped with mini guide field in the water box, described in Sec. 3.2.

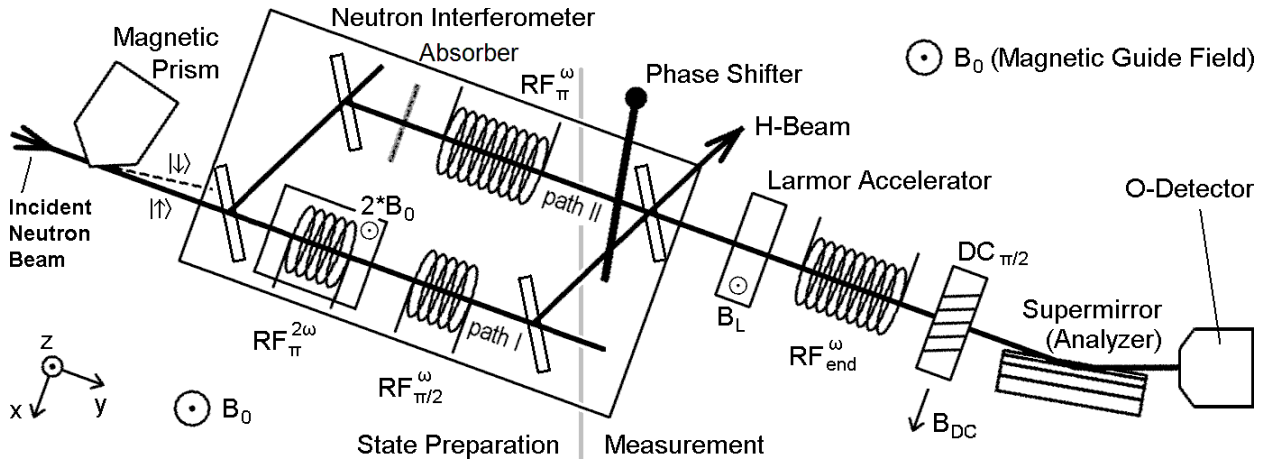


Fig. 54: Experimental setup to generate W- and GHZ-like states. The setup contains four RF and one DC spin flipper. For the generation of the W-state all three RF flippers in the IFM operated, whereas for the generation of the GHZ-state only the RF coil in path II did.

By means of a silicon perfect-crystal monochromator, a neutron beam with a mean wavelength of $\lambda_0 = 1.92\text{\AA}$ ($\Delta\lambda/\lambda_0 \approx 0.02$) was selected. Then the beam was polarized vertically by magnetic-prism refractions. Because of the angular separation of the two sub-beams, only up-spin neutrons $|\uparrow\rangle$ met the Bragg condition at the first interferometer plate. After this the beam, with an aperture of $4 \times 8 \text{mm}^2$ (width x height), entered the skew-symmetric Si perfect crystal neutron interferometer (IFM) shown in Fig. 2, which was adjusted to employ a 220 reflection, thus coherently splitting the incident beam into the two spatially separated paths I

and II at the first IFM plate. A parallel-sided aluminium plate was used as a phase shifter to vary the relative phase χ for the path degree of freedom prior to the coherent recombination of the two paths at the last IFM plate. A pair of water-cooled Helmholtz coils produced a fairly uniform magnetic guide field $B_0\hat{z}$ of 2.3mT over the region of the polarized neutron beam. This field also defined a potential energy (Zeeman energy) of the neutrons, while the total energy of a neutron is equal to the sum of its potential energy and kinetic energy. Our energy degree of freedom is the total energy, as already utilized in our previous experiment [Sponar et al., 2008]. To manipulate the neutrons, we used radio-frequency (RF) spin flippers, which change both the spin and the total energy, and a direct current (DC) spin flipper, which changes the spin without changing the total energy. The change in total energy involved by a flip from spin-up to spin-down due to an RF coil operating at frequency ω is given by $-\hbar\omega$. By a π flip we mean a flip at that most neutrons' spins are flipped (according to the efficiency of the spin flipping device), whereas a $\pi/2$ flip produces a fifty-fifty superposition of up- and down-spin states. Each time a neutron suffers a spin flip, it also suffers a phase shift $e^{i\pi/2}$. In path I of the IFM two RF spin flippers were placed in a row, the first one $\text{RF}_{\pi}^{2\omega}$ operating at double frequency 2ω and performing a π flip, the second one $\text{RF}_{\pi/2}^{\omega}$ operating at the frequency ω and performing a $\pi/2$ flip, whereas in path II one RF flipper RF_{π}^{ω} was placed, operating at the frequency ω and performing a π flip. $\text{RF}_{\pi}^{2\omega}$ was equipped with its own Helmholtz coil pair, the newly developed miniGF described in Sec. 3.2, which enabled it to operate at double frequency. All coils in the IFM were integrated in our new water-box, shown in Fig. 55, whose development was also described in Sec. 3.2. Due to this new coil cooling system, thermal disturbances from the coils in the IFM were negligible.

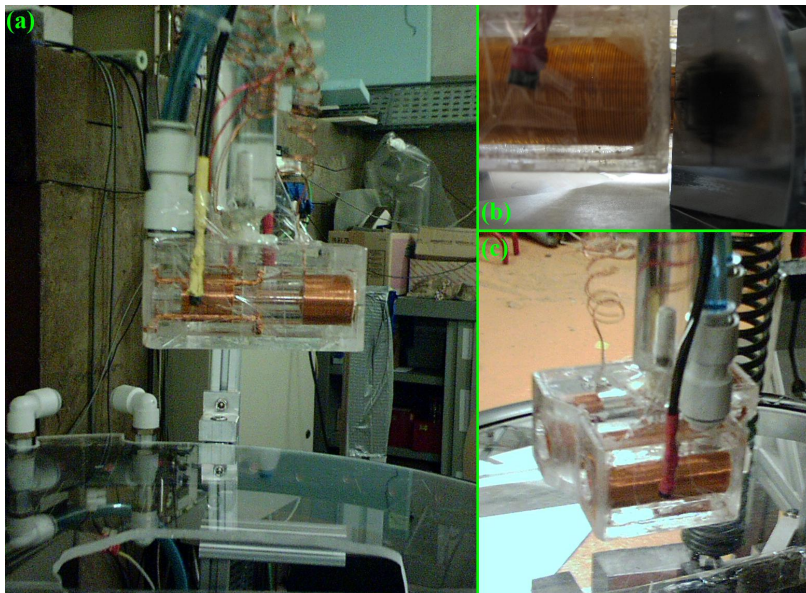


Fig. 55: Photographs of the experimental setup, with focus on the water-box with three RF coils, one equipped with the miniGF developed in Sec. 3.2. In (a) we see a side view of the water-box, (b) shows the box in the IFM, focusing on the distance between the box and an IFM plate, and (c) shows a general view of the box.

For the W- and the GHZ-like state we entangled the path, spin, and energy degrees of freedom of single

neutrons. For both states the spin-up polarized neutron beam $|\uparrow 0\rangle$ entered the IFM and split into two partial beams $\frac{1}{\sqrt{2}}|\text{I}\uparrow 0\rangle$ and $\frac{1}{\sqrt{2}}|\text{II}\uparrow 0\rangle$. The W-like state was then generated as follows: In the ideal case, $\text{RF}_{\pi}^{2\omega}$ changes $\frac{1}{\sqrt{2}}|\text{I}\uparrow 0\rangle$ to $\frac{1}{\sqrt{2}}e^{i\pi/2}|\text{I}\downarrow -2\hbar\omega\rangle$, which then the subsequent $\text{RF}_{\pi/2}^{\omega}$ changes to $\frac{1}{\sqrt{4}}e^{i\pi/2}|\text{I}\downarrow -2\hbar\omega\rangle + \frac{1}{\sqrt{4}}e^{i\pi}|\text{I}\uparrow -\hbar\omega\rangle$, while RF_{π}^{ω} changes $\frac{1}{\sqrt{2}}|\text{II}\uparrow 0\rangle$ to $\frac{1}{\sqrt{2}}e^{i\pi/2}|\text{II}\downarrow -\hbar\omega\rangle$. For the symmetric (i.e., balanced) W-state ($|W_{sym}\rangle$), with theoretical nominal coefficients $a_0 = b_0 = c_0 = \frac{1}{\sqrt{3}}$, a 50% stochastic absorber was placed in path II, whereas without the absorber an asymmetric (i.e., unbalanced) W-like state ($|W_{asym}\rangle$) was generated with nominal coefficients $a_0 = \frac{1}{\sqrt{2}}$ and $b_0 = c_0 = \frac{1}{\sqrt{4}}$. The absorber was made of 3 layers of an indium foil with 0.25mm thickness, having a measured transmission coefficient of 0.4974 ± 0.0016 , which sufficiently approximates the target value of 0.5. For the preparation of the GHZ-like state we expect nominal coefficients $d_0 = e_0 = \frac{1}{\sqrt{2}}$. Here, only RF_{π}^{ω} was switched on for state preparation while $\text{RF}_{\pi}^{2\omega}$ and $\text{RF}_{\pi/2}^{\omega}$ did not operate. Schematic views of state generation together with energy diagrams are shown in Fig. 56.

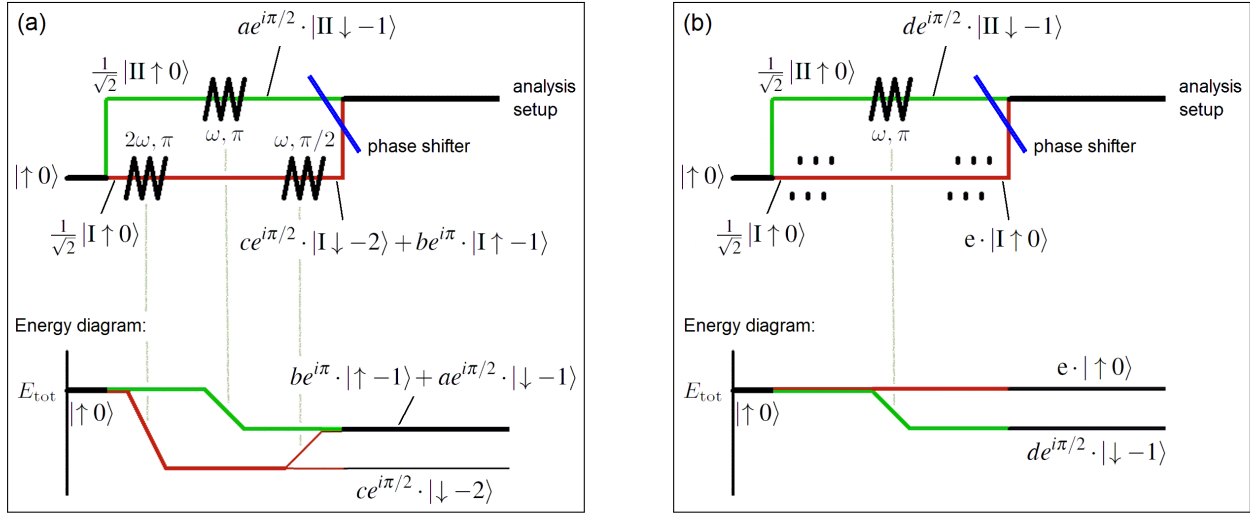


Fig. 56: Schematic view of state generation with energy diagram for (a) the W-like state and (b) the GHZ-like state. The red and green lines highlight path I and II in the IFM, respectively.

5.4. Measurement and data-analysis

Only the O-beam (the interfering beam in forward direction) was used for the measurements. The neutrons were selected for detection in dependence of their polarization and their energy. This was accomplished by a spin analyzing supermirror (transmitting up-spin neutrons only) together with a Larmor accelerator, an RF flipper $\text{RF}_{\text{end}}^{\omega}$ that operated at the frequency ω , and a DC flipper $\text{DC}_{\pi/2}$ that performed a $\pi/2$ flip. Neutrons with the selected spin properties were counted in the subsequent O-detector.

A full tomography of the generated states would have been too complex and partly even infeasible. Fortunately, the entanglement witnesses (44) and (45) do not require a full state tomography and provide enough information on each entanglement: this is a big advantage.

For the W-state in Eq. (41) the terms $\langle 101|\rho|101\rangle$, $\langle 011|\rho|011\rangle$, $\langle 002|\rho|002\rangle$, $|\langle 011|\rho|101\rangle|$, $|\langle 002|\rho|101\rangle|$, and $|\langle 002|\rho|011\rangle|$ were determined. The terms $\langle 101|\rho|101\rangle$, $\langle 011|\rho|011\rangle$, and $\langle 002|\rho|002\rangle$ were determined by intensity measurements while blocking one path in the IFM (with the Larmor accelerator and $\text{DC}_{\pi/2}$ not in operation). For the measurement of $\langle 101|\rho|101\rangle$, path I of the IFM was blocked while in path II the beam was manipulated by RF_{π}^{ω} , and the analysis setup only consisted of the super-mirror. The reference measurement was obtained while RF_{π}^{ω} was switched off. For the measurement of $\langle 011|\rho|011\rangle$ and $\langle 002|\rho|002\rangle$, path II of the IFM was blocked while the beam in path I was manipulated by $\text{RF}_{\pi}^{2\omega}$ and $\text{RF}_{\pi/2}^{\omega}$. Spin-up, spin-down and a reference measurement were made. For the spin-down measurement, $\text{RF}_{\text{end}}^{\omega}$ performed a π flip, while at the two other measurements it was switched off and for the reference measurement also $\text{RF}_{\pi}^{2\omega}$ and $\text{RF}_{\pi/2}^{\omega}$ were switched off. Each measurement was carried out ten times in order to reduce statistical errors.

In the experimental setups for the determination of the cross terms $|\langle 011|\rho|101\rangle|$, $|\langle 002|\rho|101\rangle|$, and $|\langle 002|\rho|011\rangle|$ both paths of the IFM were open. We determined these terms by means of the contrasts C of three sinusoidal interference oscillations while varying the relative phase between any two of the three (coherent) terms of the W-state in Eq. (41). These interferences between each two terms of Eq. (41) were accomplished by three different analysis setups. The determination of $|\langle 011|\rho|101\rangle|$ and $|\langle 002|\rho|101\rangle|$ requires the interference of terms that are generated in different paths of the IFM, therefore contrast scans were made by successively turning the phase shifter to successively change the relative phase χ between the respective two terms. The two terms for $|\langle 011|\rho|101\rangle|$ have the same energy but different spins, therefore in the analysis setup $\text{DC}_{\pi/2}$ was switched on, so that the two resulting spin-up terms could interfere [Sponar et al., 2008]. For the measurement of $|\langle 002|\rho|101\rangle|$ two terms have to interfere that also have an energy difference of $\hbar\omega$. Therefore also $\text{RF}_{\text{end}}^{\omega}$ performed a $\pi/2$ flip, which transformed the two terms in question into energetically equal and after $\text{DC}_{\pi/2}$ into interfering ones. Parallel to these contrast measurements also reference contrasts C^{ref} were recorded, where the three RF flippers in the IFM were switched off (the average of the reference contrasts amounted to 0.455). The contrasts were normalized by the corresponding reference contrasts in the measurement evaluation. The components of $|\langle 002|\rho|011\rangle|$ were generated in the same IFM path and had different energies, therefore it was determined by changing the components' relative phase ϕ by successively changing the strength of the magnetic field in the Larmor accelerator. Then the components were brought to interference by $\text{RF}_{\text{end}}^{\omega}$ performing a $\pi/2$ flip. Each measurement was carried out four times in order to reduce statistical errors and the contrasts and their errors were determined from

least squares fits. Typical intensity modulations are plotted in Fig. 57.

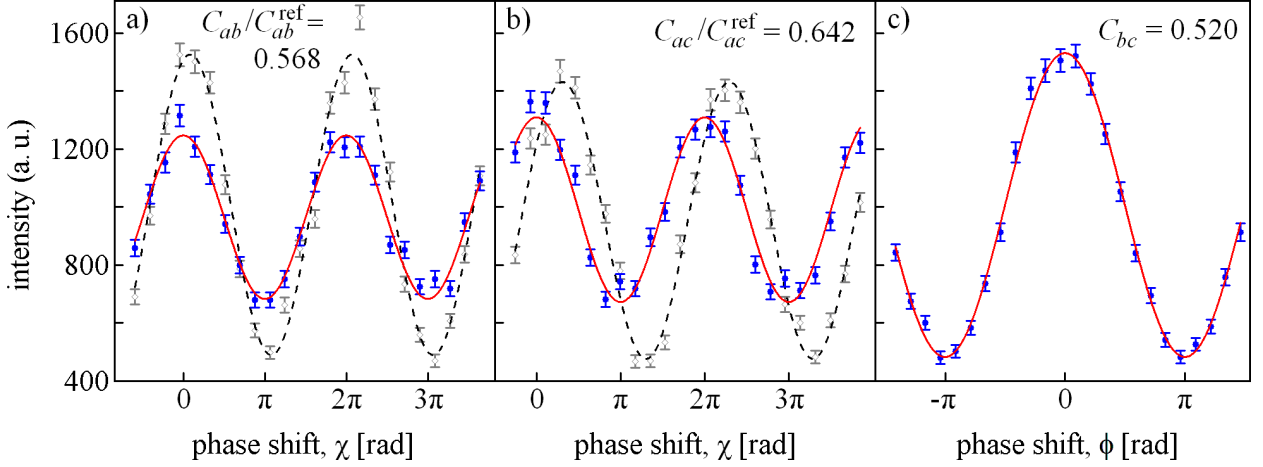


Fig. 57: Typical sinusoidal intensity oscillations of the count rates by tuning the relative phase χ or ϕ : the contrast scans in a) and b) are used to determine $|\langle 011|\rho|101\rangle|$ and $|\langle 002|\rho|101\rangle|$, respectively, (the dashed curves are reference oscillations with all RF coils in the IFM being switched off) and c) illustrates a contrast scan for $|\langle 002|\rho|011\rangle|$.

We carried out these measurements without and with the 50% stochastic absorber made of indium in path II, yielding the asymmetric and the symmetric W-like state, respectively. In the first case, each point was measured for 60s, whereas in the latter case for 80s, to compensate for the total intensity loss due to the absorber. For the GHZ-like state in Eq. (42) the terms $\langle 101|\rho|101\rangle$, $\langle 010|\rho|010\rangle$, and $|\langle 101|\rho|010\rangle|$ were measured. The determinations of these terms are analogous to those described above.

We also tested the robustness of the generated W-states. For this purpose, the above measurements for the W-state were repeated under controlled degrading of coherence between the beams in path I and II. The loss of coherence was accomplished by a shift of the wave packets relative to each other. This relative shift was achieved by placing a parallel-sided aluminium plate in path II. With this method we could accurately control the shift of the wave packet and thus the amount of the interference effect in the IFM. Accordingly, we generated a degraded, i.e., partially decohered, symmetric W-state $|W_{sym}^{deco}\rangle$ and a degraded asymmetric W-state $|W_{asym}^{deco}\rangle$.

5.5. Relations between the measured contrasts/intensities and the coefficients for the W-state

When generated in experiment, the W-state given by Eq. (41) gets a non-interfering background term:

$$|\Psi_W\rangle = ce^{i\pi/2} \cdot |I\downarrow -2\rangle + be^{i\pi} \cdot |I\uparrow -1\rangle + ae^{i\pi/2} \cdot |II\downarrow -1\rangle + \sqrt{1 - |c|^2 - |b|^2 - |a|^2} \cdot |\bullet\rangle, \quad (47)$$

where $|\bullet\rangle$ denotes the wave function of the background term, which does not contribute to the interference, and the phase factors are due to the spin flips by the RF-coils in the IFM, each flip involving a phase shift given by the factor $e^{i\pi/2}$. In the following, we describe how the values of $|\langle 011|\rho|101\rangle| = |ab|$, $|\langle 002|\rho|101\rangle| = |ac|$, and $|\langle 002|\rho|011\rangle| = |bc|$ are determined from the related contrast measurements. In each case we describe the manipulations of the wave function in the analysis setup. Finally, the relations between the coefficients and the measured contrasts C are obtained according to

$$|\langle \Psi|\Psi\rangle| = \frac{1}{2} [1 + C \cos(x)]. \quad (48)$$

The determination of $\langle 101|\rho|101\rangle = |a|^2$, $\langle 011|\rho|011\rangle = |b|^2$, and $\langle 002|\rho|002\rangle = |c|^2$ require direct intensity measurements by blocking one path in the IFM, which are subsequently described.

5.5.1. Determination of $|ab|$

$|ab|$ is determined by a phase shifter scan, i.e., a contrast scan, together with measuring a reference contrast. A schematic drawing of the state-evolution in the experiment is depicted in Fig. 58.

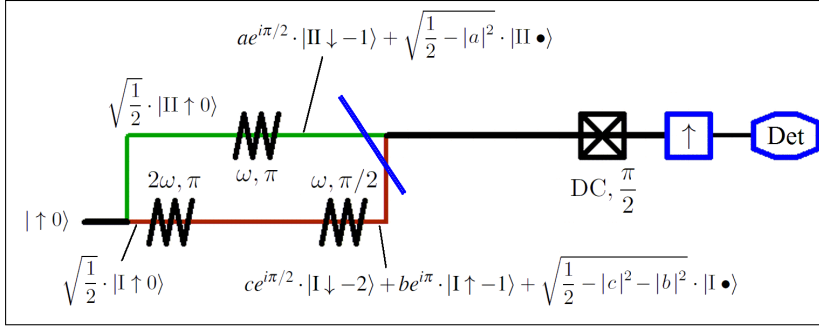


Fig. 58: Design of the experimental setup for the measurement of $|ab|$.

After the phase shifter, the wave function evolves into

$$|\Psi\rangle = ce^{i\pi/2} \cdot |\downarrow -2\rangle + be^{i\pi} \cdot |\uparrow -1\rangle + ae^{i\chi} e^{i\pi/2} \cdot |\downarrow -1\rangle + \sqrt{1 - |c|^2 - |b|^2 - |a|^2} \cdot |\bullet\rangle, \quad (49)$$

and in the subsequent analysis after the IFM, in this case after the DC $\pi/2$ -flip and the supermirror, into

$$|\Psi\rangle = \frac{c}{\sqrt{2}} e^{i\pi} \cdot |\uparrow -2\rangle + \frac{b}{\sqrt{2}} e^{i\pi} \cdot |\uparrow -1\rangle + \frac{a}{\sqrt{2}} e^{i\chi} e^{i\pi} \cdot |\uparrow -1\rangle + \sqrt{\frac{1}{2} - \frac{|c|^2}{2} - \frac{|b|^2}{2} - \frac{|a|^2}{2}} \cdot |\bullet\rangle. \quad (50)$$

According to Eq. (48), the relation between $|ab|$ and the measured contrast C_{ab} and reference contrast C_{ab}^{ref} can be taken from

$$\begin{aligned} |\langle \Psi|\Psi\rangle| &= \frac{|c|^2}{2} + \frac{|b|^2}{2} + \frac{|a|^2}{2} + \frac{b^* a e^{i\chi} + b a^* e^{-i\chi}}{2} + \frac{1}{2} - \frac{|c|^2}{2} - \frac{|b|^2}{2} - \frac{|a|^2}{2} \\ &= \frac{1}{2} [1 + 2\Re(abe^{i\chi})] = \frac{1}{2} [1 + 2\Re(|ab|e^{i\delta_{ab}}e^{i\chi})] \\ &= \frac{1}{2} [1 + 2|ab|\Re(e^{i(\chi + \delta_{ab})})] = \frac{1}{2} [1 + 2|ab|\cos(\chi + \delta_{ab})], \end{aligned} \quad (51)$$

with the result

$$|ab| = \frac{C_{ab}/C_{ab}^{\text{ref}}}{2}. \quad (52)$$

This describes how the cross term $|ab|$ relates to the measured contrasts.

5.5.2. Determination of $|ac|$

$|ac|$ is determined by a phase shifter scan, i.e., a contrast scan, together with measuring a reference contrast. A schematic drawing of the state-evolution in the experiment is depicted in Fig. 59.

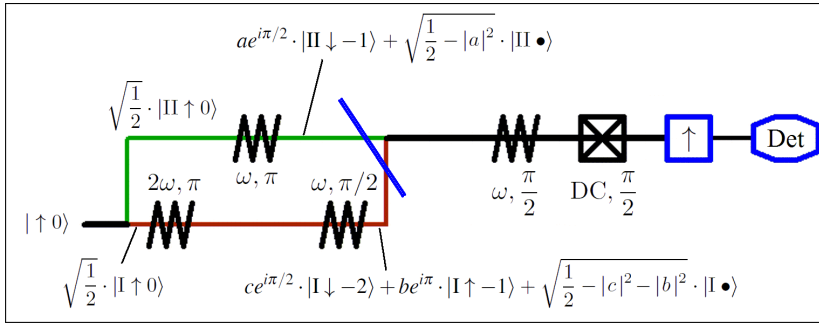


Fig. 59: Design of the experimental setup for the measurement of $|ac|$.

The wave function after the phase shifter is given by Eq. (49), which is subject to the subsequent analysis, where after the RF $\pi/2$ -flip it becomes to

$$|\Psi\rangle = \frac{c}{\sqrt{2}} \cdot (e^{i\pi/2} |\downarrow -2\rangle + e^{i\pi} |\uparrow -1\rangle) + \frac{b}{\sqrt{2}} \cdot (e^{3i\pi/2} |\downarrow -2\rangle + e^{i\pi} |\uparrow -1\rangle) + \frac{a}{\sqrt{2}} e^{i\chi} \cdot (e^{i\pi} |\uparrow 0\rangle + e^{i\pi/2} |\downarrow -1\rangle) + \sqrt{1 - |c|^2 - |b|^2 - |a|^2} \cdot |\bullet\rangle. \quad (53)$$

Then, after the subsequent DC $\pi/2$ -flip and the supermirror, it evolves into

$$|\Psi\rangle = \frac{c}{2} \cdot (e^{i\pi} |\uparrow -2\rangle + e^{i\pi} |\uparrow -1\rangle) + \frac{b}{2} \cdot (|\uparrow -2\rangle + e^{i\pi} |\uparrow -1\rangle) + \frac{a}{2} e^{i\chi} \cdot (e^{i\pi} |\uparrow 0\rangle + e^{i\pi} |\uparrow -1\rangle) + \sqrt{\frac{1}{2} - \frac{|c|^2}{2} - \frac{|b|^2}{2} - \frac{|a|^2}{2}} \cdot |\bullet\rangle, \quad (54)$$

where we considered that the spin flips due to RF- and DC-coils also involve a phase shift given by the factor $e^{i\pi/2}$. According to Eq. (48), the relation between $|ac|$ and the measured contrast C_{ac} and reference

contrast C_{ac}^{ref} can be taken from

$$\begin{aligned}
|\langle \Psi | \Psi \rangle| &= \left(\frac{|c|^2}{4} + \frac{|b|^2}{4} - \frac{|bc|}{2} \cos \delta_{bc} \right) \langle \uparrow -2 | \uparrow -2 \rangle \\
&+ \left[\frac{|c|^2}{4} + \frac{|b|^2}{4} + \frac{|a|^2}{4} + \frac{|bc|}{2} \cos \delta_{bc} + \frac{|(b+c)a|}{2} \cos(\chi + \delta_{(b+c)a}) \right] \langle \uparrow -1 | \uparrow -1 \rangle \\
&+ \frac{|a|^2}{4} \langle \uparrow 0 | \uparrow 0 \rangle + \left(\frac{1}{2} - \frac{|c|^2}{2} - \frac{|b|^2}{2} - \frac{|a|^2}{2} \right) \langle \bullet | \bullet \rangle \\
&= \left(-\frac{|bc|}{2} + \frac{|bc|}{2} \right) \cos \delta_{bc} + \frac{1}{2} + \frac{|(b+c)a|}{2} \cos(\chi + \delta_{(b+c)a}) \\
&= \frac{1}{2} (1 + (|ac + ab|) \cos(\chi + \delta_{(b+c)a})), \tag{55}
\end{aligned}$$

with the result $|ac + ab| = C_{ac}/C_{ac}^{\text{ref}}$, where $e^{i\delta_{bc}} = 1$, which yields:

$$|ac| = C_{ac}/C_{ac}^{\text{ref}} - |ab| = C_{ac}/C_{ac}^{\text{ref}} - \frac{C_{ab}/C_{ab}^{\text{ref}}}{2}. \tag{56}$$

This describes how the cross term $|ac|$ relates to the measured contrasts.

5.5.3. Determination of $|bc|$

$|bc|$ is determined by a Larmor accelerator scan, which yields a contrast. The analysis setup is shown in Fig. 60. Here no reference contrast is needed, since both terms of interest are generated in the same path of the IFM.

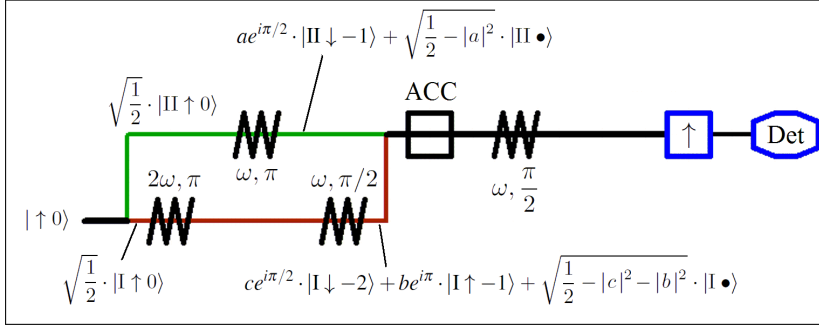


Fig. 60: Design of the experimental setup for the measurement of $|bc|$.

After the Larmor accelerator, the wave function in Eq. (47) evolves into

$$|\Psi\rangle = ce^{i\pi/2} \cdot |\downarrow -2\rangle + be^{i\pi} e^{i\phi} \cdot |\uparrow -1\rangle + ae^{i\pi/2} e^{i\phi} \cdot |\downarrow -1\rangle + \sqrt{1 - |c|^2 - |b|^2 - |a|^2} \cdot |\bullet\rangle, \tag{57}$$

and after the subsequent RF $\pi/2$ -flip and the supermirror into

$$|\Psi\rangle = \frac{c}{\sqrt{2}} e^{i\pi} \cdot |\uparrow -1\rangle + \frac{b}{\sqrt{2}} e^{i\pi} e^{i\phi} \cdot |\uparrow -1\rangle + \frac{a}{\sqrt{2}} e^{i\pi} e^{i\phi} \cdot |\uparrow 0\rangle + \sqrt{\frac{1}{2} - \frac{|c|^2}{2} - \frac{|b|^2}{2} - \frac{|a|^2}{2}} \cdot |\bullet\rangle. \tag{58}$$

According to (48), the relation between $|bc|$ and the measured contrast C_{bc} can be taken from

$$|\langle \Psi | \Psi \rangle| = \frac{|c|^2}{2} + \frac{|b|^2}{2} + \frac{|a|^2}{2} + |bc| \Re(e^{i(\phi + \delta_{bc})}) + \frac{1}{2} - \frac{|c|^2}{2} - \frac{|b|^2}{2} - \frac{|a|^2}{2} = \frac{1}{2} [1 + 2|bc| \cos(\phi + \delta_{bc})], \quad (59)$$

with the result

$$|bc| = \frac{C_{bc}}{2}. \quad (60)$$

This describes how the cross term $|bc|$ relates to the measured contrasts.

5.5.4. Determination of $|a|^2$

$|a|^2$ is determined by intensity measurements by blocking path I of the IFM. The analysis setup is shown in Fig. 61.

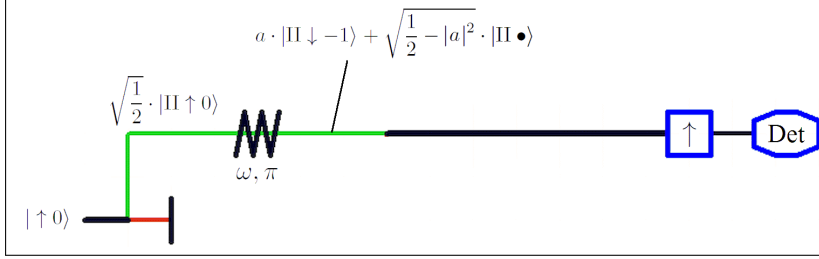


Fig. 61: Design of the experimental setup for the measurement of $|a|^2$. The green color highlights the region of the IFM.

With the beam blocker in path I, the wave function evolves into

$$|\Psi\rangle = a \cdot |\text{II} \downarrow -1\rangle + \sqrt{\frac{1}{2} - |a|^2} \cdot |\bullet\rangle, \quad (61)$$

where the first term on the right hand side vanishes after subsequent up-spin analysis by the supermirror. Accordingly, the measured intensity is

$$I_{aa} = |\langle \Psi | \Psi \rangle| = \frac{1}{2} - |a|^2, \quad (62)$$

from which we obtain $|a|^2$.

5.5.5. Determination of $|b|^2$ and $|c|^2$

$|b|^2$ and $|c|^2$ are determined by intensity measurements by blocking path II of the IFM. The analysis setups are shown in Figs. 62 and 63. With the beam blocker in path II, the wave function evolves into

$$|\Psi\rangle = c \cdot |\text{I} \downarrow -2\rangle + b \cdot |\text{I} \uparrow -1\rangle + \sqrt{\frac{1}{2} - |c|^2 - |b|^2} \cdot |\bullet\rangle. \quad (63)$$

$|c|^2$ is determined by spin-up analysis by the supermirror, according to

$$I_{cc} = |b|^2 + \frac{1}{2} - |c|^2 - |b|^2 = \frac{1}{2} - |c|^2. \quad (64)$$

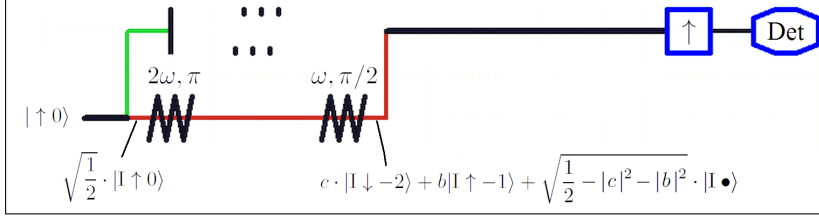


Fig. 62: Design of the experimental setup for the measurement of $|c|^2$ by spin-up analysis. The red color shows the region of the IFM.

$|b|^2$ is determined by spin-down analysis, applying a π -flip by the RF coil in the analysis setup before the supermirror, which makes (63) to

$$|\Psi\rangle = c \cdot |\uparrow -1\rangle + b \cdot |\downarrow -2\rangle + \sqrt{\frac{1}{2} - |c|^2 - |b|^2} \cdot |\bullet\rangle. \quad (65)$$

so that the measured intensity after the supermirror is

$$I_{bb} = |c|^2 + \frac{1}{2} - |c|^2 - |b|^2 = \frac{1}{2} - |b|^2. \quad (66)$$

From this we obtain $|b|^2$.

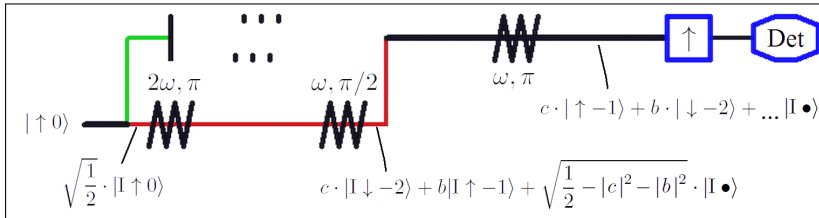


Fig. 63: Design of the experimental setup for the measurement of $|b|^2$ by spin-down analysis. The red color shows the region of the IFM.

5.6. Relations between the measured contrasts/intensities and the coefficients for the GHZ-state

Just as the W-state in Eq. (47), also the GHZ-state given by Eq. (42) gets a non-interfering background term when generated in experiment:

$$|\Psi_{GHZ}\rangle = e \cdot |I \uparrow 0\rangle + d e^{i\pi/2} \cdot |II \downarrow -1\rangle + \sqrt{1 - |e|^2 - |d|^2} \cdot |\bullet\rangle. \quad (67)$$

The relations of $\langle 101|\rho|101\rangle = |d|^2$, $\langle 010|\rho|010\rangle = |e|^2$, and $|\langle 101|\rho|010\rangle| = |de|$ with the contrast and intensity measurements are derived in the following, where in each case we describe the manipulations of the wave function in the analysis setup.

5.6.1. Determination of $|de|$, $|e|^2$, and $|d|^2$

$|de|$ is determined by a phase shifter scan, i.e., a contrast scan, together with measuring a reference contrast. A schematic drawing of the state-evolution in the experiment is depicted in Fig. 64.

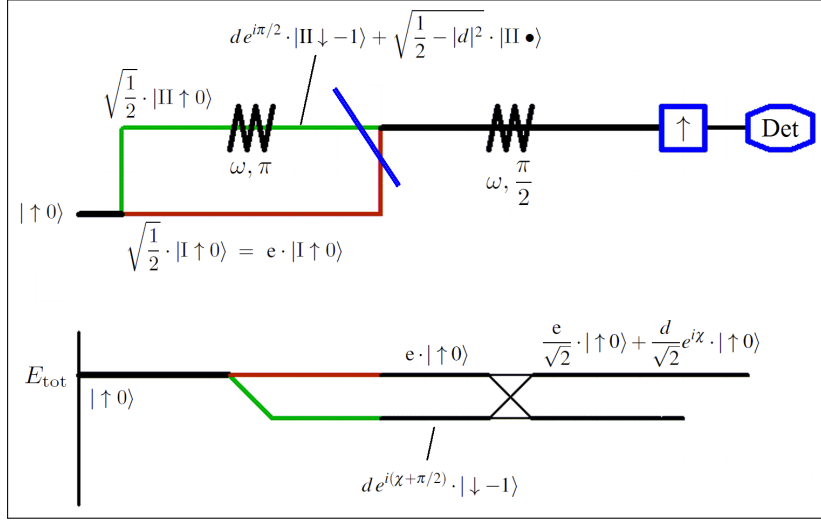


Fig. 64: Design of the experimental setup for the measurement of $|de|$ with energy diagram.

After the phase shifter, the wave function evolves into

$$|\Psi\rangle = e \cdot |\uparrow 0\rangle + d e^{i(\chi+\pi/2)} \cdot |\downarrow -1\rangle + \sqrt{1 - |e|^2 - |d|^2} \cdot |\bullet\rangle, \quad (68)$$

and after the subsequent RF $\pi/2$ -flip and the supermirror into

$$|\Psi\rangle = \frac{e}{\sqrt{2}} \cdot |\uparrow 0\rangle + \frac{d}{\sqrt{2}} e^{i\chi} \cdot |\uparrow 0\rangle + \sqrt{\frac{1}{2} - \frac{|e|^2}{2} - \frac{|d|^2}{2}} \cdot |\bullet\rangle. \quad (69)$$

According to Eq. (48), the relation between $|de|$ and the measured contrast C_{de} and reference contrast C_{de}^{ref} we can take from

$$|\langle\Psi|\Psi\rangle| = \frac{|e|^2}{2} + \frac{|d|^2}{2} + |de| \cos \chi + \frac{1}{2} - \frac{|e|^2}{2} - \frac{|d|^2}{2} = \frac{1}{2} (1 + 2|de| \cos \chi), \quad (70)$$

which yields

$$|de| = \frac{C_{de}/C_{de}^{\text{ref}}}{2} \quad (71)$$

$|e|^2$ and $|d|^2$ are determined by intensity measurements by blocking path II and I, respectively, of the IFM, as shown in Figs. 65 and 66. With the beam blocker in path II and I, the wave function given by Eq. (67) becomes to

$$|\Psi_I\rangle = e \cdot |\text{I} \uparrow 0\rangle + 0 \cdot |\bullet\rangle = \sqrt{\frac{1}{2}} \cdot |\text{I} \uparrow 0\rangle, \quad (72)$$

$$|\Psi_{II}\rangle = d \cdot |\text{II} \downarrow -1\rangle + \sqrt{\frac{1}{2} - |d|^2} \cdot |\bullet\rangle, \quad (73)$$

respectively, and after the subsequent supermirror the respective measured intensities are

$$I_I = |e|^2 = \frac{1}{2}, \quad (74)$$

$$I_{II} = \frac{1}{2} - |d|^2, \quad (75)$$

where the trivial result for $|e|^2$ we obtain due to the fact that no RF coil is involved, which would cause a background. The last equation describes how $|d|^2$ relates to the measured intensity.

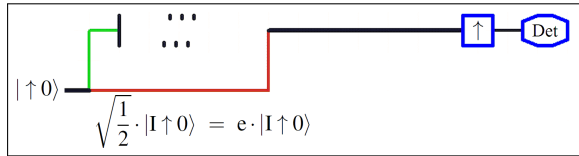


Fig. 65: Design of the experimental setup for the measurement of $|e|^2$. The red color shows the region of the IFM.

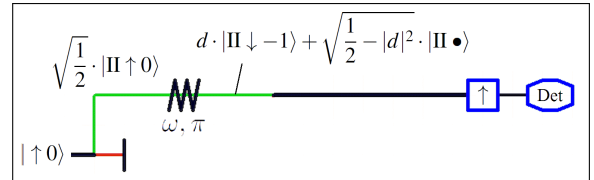


Fig. 66: Design of the experimental setup for the measurement of $|d|^2$. The green color shows the region of the IFM.

5.7. Adjustments of the spin flippers

The flip ratios of the three RF spin flippers ($\text{RF}_{\pi}^{2\omega}$, $\text{RF}_{\pi/2}^{\omega}$, and RF_{π}^{ω}) in the water box (for operation in the IFM) were previously measured at the 1.99Å polarimeter beam line of the TRIGA research reactor of the Atominstut in Vienna, the results being described below. The operation frequencies were fixed at 64935Hz (this is the frequency at that the FPGA signal generator at the S18 will operate) and the guide field was adjusted to this frequency (with a result of $\sim 21.6\text{G}$). The length of RF_{π}^{ω} (for operation in path II of the IFM) was 51.3mm, with a flip ratio of 99.9. The result of flip ratio measurement is plotted in Fig. 67. The two coils for path I each had lengths of 19.8mm, one of them equipped with the mini guide field (miniGF). These RF coils each had flip ratios of ~ 44 , the results of measurement being plotted in Figs. 68. The different flip ratios (99.9 vs. ~ 44) are mainly due to the different lengths of the coils (51.3 vs. 19.8mm).

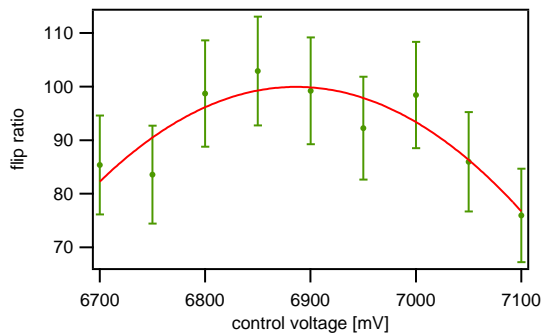


Fig. 67: Measurement of the flip ratio of RF_{π}^{ω} as a function of control voltage at the polarimeter beam line in Vienna: the maximum flip ratio reached 99.9. The length of this RF coil was 51.3mm.

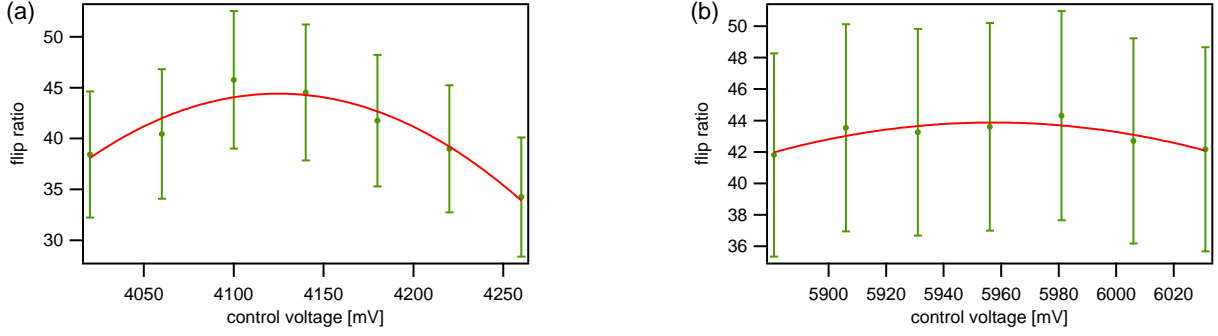


Fig. 68: Measurement of the flip ratio of (a) $RF_{\pi}^{2\omega}$ and (b) $RF_{\pi/2}^{\omega}$ as a function of control voltage at the polarimeter beam line in Vienna while the miniGF did not operate. The maximum flip ratios reached 44.4 and 43.9, respectively. Each coil's length was 19.8mm.

In the interferometric setup at S18 at ILL the flip ratios of $RF_{\pi}^{2\omega}$, $RF_{\pi/2}^{\omega}$, and RF_{π}^{ω} were considerably lower due to (i) the lower degree of polarization of the beam and (ii) the operation of the miniGF, which was placed over $RF_{\pi}^{2\omega}$ whereas RF_{π}^{ω} and mainly $RF_{\pi/2}^{\omega}$ were subject to its stray field. The flip ratios measured in the interferometric setup are given in Tab. IV. The RF coils were operated by the FPGA signal generator with 4 output channels to achieve perfect synchronization of the sinusoidal signals. Such synchronization failed in previous attempts with two commercial, triggered signal generators, each having 2 output signals. $RF_{\pi}^{2\omega}$, equipped with the miniGF, was operated at 129870Hz. Adjustment was carried out by means of adjusting the guide fields and spin flipper currents. At first, RF_{end}^{ω} was adjusted by adjusting the current of the rectangular guide field, which ranges over the whole beam line, yielding 8.64A as a result. Then RF_{π}^{ω} was adjusted by means of the circular guide field, which only ranges over the IFM, adjustment resulting in a current of -0.16A . Next, $RF_{\pi}^{2\omega}$ was adjusted by means of the miniGF, resulting in a miniGF current of 3.61A. Finally, $RF_{\pi/2}^{\omega}$ was adjusted for a $\pi/2$ -flip, by performing two RF current scans while $RF_{\pi}^{2\omega}$ is once switched off and once on and the two curves' point of intersection gives the operating current of $RF_{\pi/2}^{\omega}$. This adjustment of $RF_{\pi/2}^{\omega}$ for a $\pi/2$ -flip is plotted in Fig. 69. The currents through the RF coils were determined by a clamp-on amperemeter.

coil	flip ratio	contrast	(peak) RF-/DC-current [mA]
$\text{RF}_{\pi}^{2\omega}$	32.2	0.9398	688
$\text{RF}_{\pi/2}^{\omega}$	15.8	0.8812	824
RF_{π}^{ω}	49.6	0.9605	240
$\text{RF}_{\text{end}}^{\omega}$	57.1	0.9656	810
$\text{DC}_{\pi/2}$	33.4	0.9418	$I_Z = -1355, I_X = 1416$

TABLE IV: Flip ratios, the corresponding contrasts, and peak RF-currents (or DC-currents) in π -flip mode of the spin flippers in the interferometric setup. The very low flip ratio of $\text{RF}_{\pi/2}^{\omega}$ is due to its placement in the stray field of the miniGF, which cannot be avoided. This however is unproblematic, because this RF coil merely needs to perform a $\pi/2$ -flip.

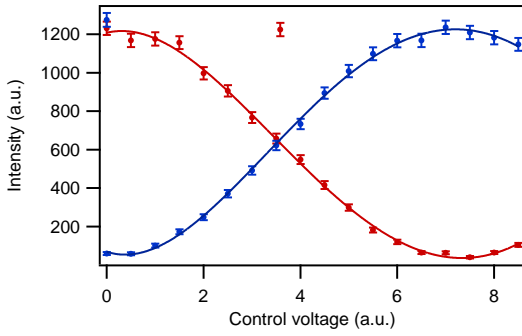


Fig. 69: Measurement to adjust $\text{RF}_{\pi/2}^{\omega}$ to give a $\pi/2$ -flip. $\text{RF}_{\pi}^{2\omega}$ once operated (blue curve) and once was switched off (red curve). The ideal (peak) current, at which $\text{RF}_{\pi/2}^{\omega}$ performs a $\pi/2$ -flip, coincides with the two curves' intersection and amounts to 364mA. The two separate points at the top, which are not part of the fits, represent reference measurements (e.g., used in determining the flip ratio).

The degree of polarization P of the beam was measured by using the two RF coils with the highest flip ratio, i.e., RF_{π}^{ω} and $\text{RF}_{\text{end}}^{\omega}$. Four intensities were recorded: with both RFs being switched off (I_0), with only RF_{π}^{ω} operating (I_1), with only $\text{RF}_{\text{end}}^{\omega}$ operating (I_2), and with both RF coils operating (I_3):

$$P = \sqrt{\frac{(I_0 - I_1)(I_0 - I_2)}{I_0 I_3 - I_1 I_2}} = \sqrt{\frac{(r-1)(r'-1)}{rr' I_3 / I_0 - 1}}, \quad (76)$$

where r and r' are the respective flip ratios of the two RF coils. The measured values were $I_0 = 7931 \pm 89.056$, $I_1 = 159.997 \pm 53.750$, $I_2 = 138.849 \pm 25.353$, and $I_3 = 8022 \pm 89.566$, where I_0 and I_3 represent actual count rates while I_1 and I_2 are normalized to I_0 . Inserting these values in the above formula, we obtain: $P = 0.9757 \pm 0.0087$.

5.8. Results: determination of entanglement witness

Obtained values for the coefficients on basis of the contrast and intensity measurements are given for the asymmetric and the symmetric W-like states, also with controlled decoherence, in Tab. V. The coefficients for the GHZ state are given in Tab. VI.

coeff.	$ W_{asym}\rangle$	$ W_{sym}\rangle$	$ W_{asym}^{deco}\rangle$	$ W_{sym}^{deco}\rangle$
$ ab\rangle$	$(0.7790 \pm 0.0160)/(2\sqrt{2})$	$(0.7881 \pm 0.0181)/3$	$(0.2704 \pm 0.0138)/(2\sqrt{2})$	$(0.2754 \pm 0.0174)/3$
$ ac\rangle$	$(1.0968 \pm 0.0357)/(2\sqrt{2})$	$(1.3270 \pm 0.0461)/3$	$(0.2425 \pm 0.0305)/(2\sqrt{2})$	$(0.2689 \pm 0.0404)/3$
$ bc\rangle$	$(0.9270 \pm 0.0101)/4$	$(0.8620 \pm 0.0075)/3$	$(0.9661 \pm 0.0102)/4$	$(0.8942 \pm 0.0077)/3$
$ a ^2$	$(0.9729 \pm 0.0055)/2$	$(0.9586 \pm 0.0100)/3$	$(0.9679 \pm 0.0064)/2$	$(0.9668 \pm 0.0091)/3$
$ b ^2$	$(0.9217 \pm 0.0564)/4$	$(0.9667 \pm 0.0543)/3$	$(0.9217 \pm 0.0564)/4$	$(0.9667 \pm 0.0543)/3$
$ c ^2$	$(1.0024 \pm 0.0535)/4$	$(1.0077 \pm 0.0528)/3$	$(1.0024 \pm 0.0535)/4$	$(1.0077 \pm 0.0528)/3$

TABLE V: Experimentally determined coefficients for the W-like states. The numbers given are the arithmetic means of several measurements (four measurements for each $|ab\rangle$, $|ac\rangle$, and $|bc\rangle$ and ten measurements for each $|a|^2$, $|b|^2$, and $|c|^2$).

coeff.	$ GHZ\rangle$
$ de\rangle$	$(0.9814 \pm 0.0140)/2$
$ d ^2$	$(0.9786 \pm 0.0047)/2$
$ e ^2$	$(1 \pm 0.0097)/2$

TABLE VI: Experimentally determined coefficients for the GHZ-like state. The numbers given are the arithmetic means of several measurements (four measurements for $|de\rangle$ and ten measurements for each $|d|^2$ and $|e|^2$).

From the coefficients in Tabs. V and VI the fidelities for the GHZ-like state, the symmetric and asymmetric W-like states, and the respective degraded (partially decohered) W-like states were determined, according to formula (43). The achieved fidelity values are listed in Tab. VII. These values can be mainly attributed to the efficiencies of the spin flippers. The values for the criteria expressed in the inequalities (44) and (45) are listed in Tab. VIII, clearly demonstrating the presence of genuine multipartite entanglement.

state	noiseless	with noise
$ GHZ\rangle$	$F = 0.9853 \pm 0.0212$	NA
$ W_{sym}\rangle$	$F = 0.9874 \pm 0.0289$	$F = 0.6465 \pm 0.0275$
$ W_{asym}\rangle$	$F = 0.9483 \pm 0.0224$	$F = 0.6112 \pm 0.0208$

TABLE VII: Fidelities of the generated GHZ-like state, symmetric and asymmetric W-like states, and respective W-states with controlled decoherence (noise). The high fidelity values of the three noiseless states demonstrate the high quality of state generation made possible by our new RF spin flippers for the IFM.

state	noiseless	with noise
$ GHZ\rangle$	$I_{GHZ} = 0.49 \pm 0.01$	NA
$ W_{sym}\rangle$	$I_W = 0.47 \pm 0.03$	$I_W = -0.04 \pm 0.02$
$ W_{asym}\rangle$	$I_W = 0.46 \pm 0.02$	$I_W = -0.01 \pm 0.01$

TABLE VIII: The almost maximal violation clearly indicates multipartite entanglement and thus demonstrates the high amount of control in neutron state preparation (maximal violation is given by 0.5). In the presence of noise (degrading of coherence) no multipartite entanglement is detectable.

Studying the influence of noise can indicate the robustness of each entanglement against decoherence. A wave-packet shifter (parallel-sided aluminium plate) was employed for this study: the shift of the wave packets was accurately controlled so that we could control the amount of the interference effect in the IFM. The situation where all genuine multipartite entanglement is lost with retaining bipartite entanglement in the system was accomplished and investigated. The analysis was done via inequalities $I_{k-sep}[\rho] \leq 0$, given by Eq. (46), which are satisfied for any k -separable state derived in [Gabriel et al., 2010]. Thus these inequalities enable us to reveal more refined structures. For example, if one finds a violation of the inequality $I_{3-sep}[\rho]$ for a tripartite state ρ , then the state is not fully separable, namely, entangled. However, it may still be “only” bipartite entangled, while a violation of I_{2-sep} shows that the state is genuine multipartite entangled (while the criteria I_{GHZ} and I_W are optimized to detect the different types of genuine multipartite entanglement). The results are listed in Tab. IX. The obtained values are greater than 0 and thus the non full-separability is confirmed, even in the noisy case. (The fidelities also prove inseparability in these systems, albeit with a smaller experimental significance).

state	noiseless	with noise
$ GHZ\rangle$	$I_{3-sep} = 0.49 \pm 0.01$	NA
$ W_{sym}\rangle$	$I_{3-sep} = 0.65 \pm 0.02$	$I_{3-sep} = 0.31 \pm 0.01$
$ W_{asym}\rangle$	$I_{3-sep} = 0.45 \pm 0.01$	$I_{3-sep} = 0.11 \pm 0.01$

TABLE IX: Despite the strong noise and (potential) loss of genuine multipartite entanglement, the data show that the states are not fully separable. This can also be seen in the fidelity witness in this specific case.

To conclude, in the present neutron interferometer experiment specific tripartite-entangled states, i.e., W- and GHZ-states, have been successfully generated with high fidelity by using substantially improved RF spin flippers. The entanglement content of these states was quantified using nonlinear witnesses. It was demonstrated that different types of multipartite entanglement can be shown to be present in a single-neutron system even by measuring only few matrix elements. Moreover, via the control of the system under investigation we induced partial decoherence in some components of the system and thus demonstrated the loss of multipartite entanglement while inseparability is still kept. This gives a basis for studies on the mixture and transition between these states and the totally decohered state, by which characteristic properties of tripartite entanglement can be demonstrated. In such studies, influences of various kinds of decoherence on entanglement can be investigated: in particular, a method involving more sophisticated controllable decoherence mechanisms (e.g. like in experiment [Sulyok et al., 2010]) could play an important role.

6. CONCLUSIONS AND OUTLOOK

The main focus of this thesis has been the development of new spin and energy manipulating devices; more exactly, RF spin flippers and Larmor precession manipulators for the use in an interferometer have been developed that cause significantly lower degrading of the interference contrast than our previous devices. With the new devices certain experiments are made possible, e.g., the generation of a W-state could be realized [Erdős et al., 2013] due to RF spin flippers equipped with our newly developed mini guide field together with our new coil cooling method that uses a water-box, which have been described in Sec. 3.2. Also, previous experiments, e.g., violation of a Bell-like inequality, can be repeated with higher precision [Hasegawa and Erdős, 2011]. Neutron interferometric investigations on the Bell-like inequality have been described in Sec. 4, for which entanglement between degrees of freedom in a single-neutron system has been exploited. A Bell-like state comprising spin-path entanglement has been generated by using a new, two-step spin preparation scheme and a new Larmor precession manipulator (which have been described in Sec. 3.3), more exactly a Mu-metal tube, where the beam did not go through any material, resulting in less decoherence and higher fidelity of the generated Bell-like state. The obtained result exhibits considerably more significant violation of the Bell-like inequality than the previous measurement [Hasegawa et al., 2003], thus confirming quantum contextuality with higher precision. Using substantially improved RF spin flippers equipped with mini guide field, we have succeeded in generating tripartite entangled W-like state families and a GHZ-like state with high fidelity within neutron interferometry, as has been described in Sec. 5. Genuine tripartite entanglement of these states was analyzed by proper nonlinear witnesses. It was demonstrated that, only by measuring few matrix elements, different types of multipartite entanglement can be shown to be present in a single-neutron system. The substructure of an entangled single-neutron system and high controllability, which are revealed in our experiments, open the possibility for testing more fundamental and sophisticated properties of neutrons via exploring just this substructure, e.g., its relation to topological phases [Bertlmann et al., 2004, Filipp et al., 2009, Sponar et al., 2010b] or to the effect of a gravitational field [Zych et al., 2011]. The new spin preparation scheme and the new method of mini guide fields with water-box have also been used in further neutron interferometer experiments, such as weak measurements [Sponar et al., 2014] and a quantum Cheshire Cat experiment [Denkmayr et al., 2014].

Bibliography

- [Acin et al., 2001] A. Acin, D. Bruß, M. Lewenstein, and A. Sanpera, *Classification of mixed three-qubit states*, Phys. Rev. Lett. **87**, 040401 (2001).
- [Arndt, 1999] M. Arndt, O. Nairz, J. Voss-Andreae, C. Keller, G. van der Zouw, and A. Zeilinger, *Wave-particle duality of C60 molecules*, Nature **401**, 680 (1999).
- [Aspect et al., 1981] A. Aspect, P. Grangier, and G. Roger, *Experimental tests of realistic local theories via Bell's theorem*, Phys. Rev. Lett. **47**, 460 (1981).
- [Aspect et al., 1982a] A. Aspect, J. Dalibard, and G. Roger, *Experimental test of Bell's inequalities using time-varying analyzers*, Phys. Rev. Lett. **49**, 1804 (1982).
- [Aspect et al., 1982b] A. Aspect, P. Grangier, and G. Roger, *Experimental realization of Einstein-Podolsky-Rosen-Bohm gedankenexperiment: A new violation of Bell's inequalities*, Phys. Rev. Lett. **49**, 91 (1982).
- [Aspect, 1984] A. Aspect, in *The Wave-Particle Dualism*, edited by S. Diner, D. Fargue, G. Lochak, and F. Selleri, D. Reidel Publishing Company, Dordrecht (1984), pp. 377.
- [Aspect, 1999] A. Aspect, *Bell's inequality test: more ideal than ever*, Nature (London) **398**, 189 (1999).
- [Badurek et al., 1983] G. Badurek, H. Rauch, and J. Summhammer, *Time-dependent superposition of spinors*, Phys. Rev. Lett. **51**, 1015 (1983).
- [Badurek et al., 1986] G. Badurek, H. Rauch, and D. Tuppinger, *Neutron interferometric double-resonance experiment*, Phys. Rev. A **34**, 2600 (1986).
- [Bartosik et al., 2009] H. Bartosik, J. Klepp, C. Schmitzer, S. Sponar, A. Cabello, H. Rauch, and Y. Hasegawa, *Experimental test of quantum contextuality in neutron interferometry*, Phys. Rev. Lett. **103**, 040403 (2009).
- [Basu et al., 2001] S. Basu, S. Bandyopadhyay, G. Kar, and D. Home, *Bell's inequality for a single spin-1/2 particle and quantum contextuality*, Phys. Lett. A **279**, 281 (2001); arXiv:quant-ph/9907030.
- [Bell, 1964] J. S. Bell, *On the Einstein-Podolsky-Rosen paradox*, Physics **1**, 195 (1964).

- [Bell, 1966] J. S. Bell, *On the problem of hidden variables in quantum mechanics*, Rev. Mod. Phys. **38**, 447 (1966).
- [Berman, 1997] P. Berman (ed.), *Atom interferometry*, Academic Press, New York (1997).
- [Bertlmann and Zeilinger, 2002] R. A. Bertlmann and A. Zeilinger, *Quantum [Un]speakables, from Bell to quantum information*, Springer Verlag, Heidelberg (2002).
- [Bertlmann et al., 2004] R. A. Bertlmann, K. Durstberger, Y. Hasegawa, and B. C. Hiesmayr, *Berry phase in entangled systems: A proposed experiment with single neutrons*, Phys. Rev. A **69**, 032112 (2004).
- [Bohm, 1951] D. Bohm, *Quantum theory*, Prentice-Hall, Englewood Cliffs N.J. (1951).
- [Bonse and Hart, 1965] U. Bonse and M. Hart, *An X-ray interferometer*, Appl. Phys. Lett. **6**, 155 (1965).
- [Bouwmeester et al., 1999] D. Bouwmeester, J.-W. Pan, M. Daniell, H. Weinfurter, and A. Zeilinger, *Observation of three-photon Greenberger-Horne-Zeilinger entanglement*, Phys. Rev. Lett. **82**, 1345 (1999).
- [Cabello et al., 2008a] A. Cabello, S. Filipp, H. Rauch, and Y. Hasegawa, *Proposed Experiment for Testing Quantum Contextuality with Neutrons*, Phys. Rev. Lett. **100**, 130404 (2008).
- [Cabello, 2008b] A. Cabello, *Experimentally Testable State-Independent Quantum Contextuality*, Phys. Rev. Lett. **101**, 210401 (2008).
- [Cimmino et al., 1989] A. Cimmino, G. I. Opat, A. G. Klein, H. Kaiser, S. A. Werner, M. Arif, and R. Clothier, *Observation of the topological Aharonov-Casher phase shift by neutron interferometry*, Phys. Rev. Lett. **63**, 380 (1989).
- [Clauser et al., 1969] J. F. Clauser, M. A. Horne, A. Shimony, and R. A. Holt, *Proposed experiment to test local hidden-variable theories*, Phys. Rev. Lett. **3**, 880 (1969).
- [Clauser, 1976] J. F. Clauser, *Experimental investigation of a polarization correlation anomaly*, Phys. Rev. Lett. **36**, 1223 (1976).
- [Colella et al., 1975] R. Colella, A. W. Overhauser, and S. A. Werner, *Observation of gravitationally induced quantum interference*, Phys. Rev. Lett. **34**, 1472 (1975).

- [Denkmayr et al., 2014] T. Denkmayr, H. Geppert, S. Sponar, H. Lemmel, A. Matzkin, J. Tollaksen, and Y. Hasegawa, *Observation of a quantum Cheshire Cat in a matter-wave interferometer experiment*, Nat. Commun. **5**, 4492 (2014); arXiv:1312.3775.
- [Dür et al., 2000] W. Dür, G. Vidal, and J. I. Cirac, *Three qubits can be entangled in two inequivalent ways*, Phys. Rev. A **62**, 062314 (2000).
- [Einstein et al., 1935] A. Einstein, B. Podolsky, and N. Rosen, *Can quantum mechanical description of physical reality be considered complete?*, Phys. Rev. **47**, 777 (1935).
- [Erdős et al., 2013] D. Erdős, M. Huber, B. C. Hiesmayr, and Y. Hasegawa, *Proving the Generation of Genuine Multipartite Entanglement in a Single-Neutron Interferometer Experiment*, New J. Phys. **15**, 023033 (2013).
- [Filipp et al., 2009] S. Filipp, J. Klepp, Y. Hasegawa, C. Plonka-Spehr, U. Schmidt, P. Geltenbort, and H. Rauch, *Experimental Demonstration of the Stability of Berry's Phase for a Spin-1/2 Particle*, Phys. Rev. Lett. **102**, 030404 (2009).
- [Freedman and Clauser, 1972] S. J. Freedman and J. F. Clauser, *Experimental test of local hidden-variable theories*, Phys. Rev. Lett. **28**, 938 (1972).
- [Fry and Thompson, 1976] E. S. Fry and R. C. Thompson, *Experimental test of local hidden-variable theories*, Phys. Rev. Lett. **37**, 465 (1976).
- [Gühne and Seevinck, 2010] O. Gühne and M. Seevinck, *Separability criteria for genuine multipartite entanglement*, New J. Phys. **12**, 053002 (2010).
- [Gabriel et al., 2010] A. Gabriel, B. C. Hiesmayr, and M. Huber, Quantum Inform. Comput. **10**, 0829-0836 (2010).
- [Garg and Mermin, 1987] A. Garg and N. D. Mermin, *Detector inefficiencies in the Einstein-Podolsky-Rosen experiment*, Phys. Rev. D **35**, 3831 (1987).
- [Geppert et al., 2014] H. Geppert, T. Denkmayr, S. Sponar, H. Lemmel, Y. Hasegawa, *Improvement of the polarized neutron interferometer setup demonstrating violation of a Bell-like inequality*, Nuclear Instruments and Methods in Physics Research A **763**, 417 (2014); arXiv:1404.3512.
- [Grangier, 2001] P. Grangier, *Count them all*, Nature (London) **409**, 774 (2001).

- [Gränicher, 1996] W. H. Heini Gränicher, *Messung beendet - was nun?*, 2., überarb. Aufl., Hochschulverl. AG an der ETH Zürich, Zürich (1996), Kap. 6.2.2.
- [Greenberger et al., 1989] D. M. Greenberger, M. A. Horne, and A. Zeilinger, in *Bell's Theorem, Quantum Theory and Conceptions of the Universe*, edited by M. Kafatos (Kluwer Academics, Dordrecht, The Netherlands, 1989), pp. 73-76.
- [Greenberger et al., 1990] D. M. Greenberger, A. Shimony, M. A. Horne, and A. Zeilinger, *Bell's theorem without inequalities*, Am. J. Phys. **58**, 1131 (1990).
- [Hasegawa and Erdős, 2011] Y. Hasegawa and D. Erdős, *Spin-path entanglement in single-neutron interferometer experiments*, AIP Conf. Proc. **1384**, 214-217 (2011).
- [Hasegawa et al., 2003] Y. Hasegawa, R. Loidl, G. Badurek, M. Baron, and H. Rauch, *Violation of a Bell-like inequality in single-neutron interferometry*, Nature (London) **425**, 45 (2003).
- [Hasegawa et al., 2006] Y. Hasegawa, R. Loidl, G. Badurek, M. Baron, and H. Rauch, *Quantum contextuality in a single-neutron optical experiment*, Phys. Rev. Lett. **97**, 230401 (2006).
- [Hasegawa et al., 2007] Y. Hasegawa, R. Loidl, G. Badurek, S. Filipp, J. Klepp, and H. Rauch, *Evidence for entanglement and full tomographic analysis of Bell states in a single-neutron system*, Phys. Rev. A **76**, 052108 (2007).
- [Hasegawa et al., 2010] Y. Hasegawa, R. Loidl, G. Badurek, K. Durstberger-Rennhofer, S. Sponar and H. Rauch, *Engineering of triply entangled states in a single-neutron system*, Phys. Rev. A **81**, 032121 (2010).
- [Häffner et al., 2005] H. Häffner, W. Hänsel, C. F. Roos, J. Benhelm, D. C. al kar, M. Chwalla, T. Körber, U. D. Rapol, M. Riebe, P. O. Schmidt, C. Becher, O. Gühne, W. Dür, and R. Blatt, *Scalable multiparticle entanglement of trapped ions*, Nature (London) **438**, 643 (2005).
- [Heisenberg, 1927] W. Heisenberg, *Über den anschaulichen Inhalt der quantentheoretischen Kinematik und Mechanik*, Z. Phys. **43**, 172 (1927).
- [Hiesmayr et al., 2009] B. C. Hiesmayr, M. Huber, and Ph. Krammer, *Two computable sets of multipartite entanglement measures*, Phys. Rev. A. **79**, 062308 (2009).

- [Hiesmayr et al., 2012] B. C. Hiesmayr, A. Di Domenico, C. Curceanu, A. Gabriel, M. Huber, J.-Å. Larsson, P. Moskal, *Revealing Bell's Nonlocality for Unstable Systems in High Energy Physics*, Eur. Phys. J. C **72**, 1856 (2012) and references therein.
- [Home and Sengupta, 1984] D. Home and S. Sengupta, *Bell's inequality and noncontextual dispersion-free states*, Phys. Lett. A **102**, 159 (1984).
- [Horodecki et al., 2001] M. Horodecki, P. Horodecki, and R. Horodecki, *Separability of n -particle mixed states: necessary and sufficient conditions in terms of linear maps*, Phys. Lett. A **283**, 1 (2001).
- [Huber et al., 2010] M. Huber, F. Mintert, A. Gabriel, and B. C. Hiesmayr, *Detection of High-Dimensional Genuine Multipartite Entanglement of Mixed States*, Phys. Rev. Lett. **104**, 210501 (2010).
- [Jozsa, 1994] R. Jozsa, *Fidelity for Mixed Quantum States*, J. Mod. Opt. **41**(12), 2315 (1994).
- [Kirchmair, 2009] G. Kirchmair, F. Zähringer, R. Gerritsma, M. Kleinmann, O. Gühne, A. Cabello, R. Blatt, and C. F. Roos, *State-independent experimental test of quantum contextuality*, Nature Letters **460**, 494 (2009).
- [Kochen and Specker, 1967] S. Kochen and E. P. Specker, *The Problem of Hidden Variables in Quantum Mechanics*, J. Math. Mech. **17**, 59-87 (1967).
- [Kraan et al., 2003] W. H. Kraan, S.V. Grigoriev, M.Th. Rekveldt, H. Fredrikze, C.F. de Vroege, and J. Plomp, *Test of adiabatic spin flippers for application at pulsed neutron sources*, Nucl. Instr. and Meth. A **510**, 334 (2003).
- [Kroupa et al., 2000] G. Kroupa, G. Bruckner, O. Bolik, M. Zawisky, M. Hainbuchner, G. Badurek, R.J. Buchelt, A. Schricker, and H. Rauch, *Basic features of the upgraded S18 neutron interferometer set-up at ILL*, Nucl. Instr. and Meth. A **440**, 604 (2000).
- [Kwiat et al., 1995] P. G. Kwiat, K. Mattle, H. Weinfurter, A. Zeilinger, A. V. Sergienko, and Y. Shih, *New high-intensity source of polarization-entangled photon pairs*, Phys. Rev. Lett. **75**, 4337 (1995).
- [Larsson, 1998] J.-Å. Larsson, *Bell's inequality and detector inefficiency*, Phys. Rev. A **57**, 3304 (1998).

- [Leibfried et al., 2005] D. Leibfried, E. Knill, S. Seidelin, J. Britton, R. B. Blakestad, J. Chiaverini, D. B. Hume, W. M. Itano, J. D. Jost, C. Langer, R. Ozeri, R. Reichle, and D. J. Wineland, *Creation of a six-atom 'Schrödinger cat' state*, Nature (London) **438**, 639 (2005).
- [Lu et al., 2007] C.-Y. Lu, X.-Q. Zhou, O. Gühne, W.-B. Gao, J. Zhang, Z.-S. Yuan, A. Goebel, T. Yang, and J.-W. Pan, *Experimental entanglement of six photons in graph states*, Nature Physics **3**, 91 (2007).
- [Mach, 1892] L. Mach, *Über einen Interferenzrefraktor*, Zeitschrift für Instrumentenkunde **12**, 89 (1892).
- [Marton et al., 1953] L. Marton, J. A. Simpson, and J. A. Suddeth, *Electron beam interferometer*, Phys. Rev. **90**, 490 (1953).
- [Matsukevich et al., 2008] D. N. Matsukevich, P. Maunz, D. L. Moehring, S. Olmschenk, and C. Monroe, *Bell inequality violation with two remote atomic qubits*, Phys. Rev. Lett. **100**, 150404 (2008).
- [Mermin, 1990] N. D. Mermin, *Simple unified form for the major no-hidden-variables theorems*, Phys. Rev. Lett. **65**, 3373 (1990).
- [Mermin, 1993] N. D. Mermin, *Hidden variables and the two theorems of John Bell*, Rev. Mod. Phys. **65**, 803 (1993).
- [Miszczak et al., 2009] J. A. Miszczak, Z. Puchala, P. Horodecki, A. Uhlmann, and K. Życzkowski, *Sub- and Super-Fidelity as Bounds for Quantum Fidelity*, Quantum Inf. Comput. **9**(1&2), 103 (2009).
- [Moehring et al., 2004] D. L. Moehring, M. J. Madsen, B. B. Blinov, and C. Monroe, *Experimental Bell inequality violation with an atom and a photon*, Phys. Rev. Lett. **93**, 090410 (2004).
- [Möllenstedt, 1959] G. Möllenstedt and C. Jönsson, *Elektronen-Mehrfachinterferenzen an regelmässig hergestellten Feinspalten*, Z. Phys. **155**, 472 (1959).
- [Nielsen and Chuang, 2000] M. A. Nielsen and I. L. Chuang, *Quantum Computation and Quantum Information*, Cambridge University Press, Cambridge (2000).
- [Pan et al., 2000] J.-W. Pan, D. Bouwmeester, M. Daniell, H. Weinfurter, and A. Zeilinger, *Observation of three-photon Greenberger-Horne-Zeilinger entanglement*, Nature (London) **403**, 515 (2000).

- [Peres, 1990] A. Peres, *Incompatible results of quantum measurements*, Phys. Lett. A **151**, 107 (1990).
- [Pipkin, 1978] F. Pipkin, *Atomic physics tests of the basic concepts in quantum mechanics*, in “Advances in Atomic and Molecular Physics”, D.R. Bates and B. Bederson, ed., Academic (1978).
- [Rauch et al., 1974] H. Rauch, W. Treimer, and U. Bonse, *Test of a single crystal neutron interferometer*, Phys. Lett. A **47**, 369 (1974).
- [Rauch et al., 1975] H. Rauch, A. Zeilinger, G. Badurek, A. Wilfing, W. Bauspiess, and U. Bonse, *Verification of coherent spinor rotation of fermions*, Phys. Lett. A **54**, 425 (1975).
- [Rauch and Petrascheck, 1976a] H. Rauch and D. Petrascheck, *Grundlagen für ein Laue-Neutroneninterferometer - Teil 1: Dynamische Beugung*, AIAU 74405b, Atominstitut der Österreichischen Universitäten (1976).
- [Rauch and Petrascheck, 1976b] H. Rauch and D. Petrascheck, *Grundlagen für ein Laue-Neutroneninterferometer - Teil 2: Theorie des Interferometers*, AIAU 76401, Atominstitut der Österreichischen Universitäten (1976).
- [Rauch and Petrascheck, 1978] H. Rauch and D. Petrascheck, In: *Neutron Diffraction* (ed. by H. Dachs), Top. Curr. Phys. **6**, 303, Springer, Heidelberg (1978).
- [Rauch and Werner, 2000] H. Rauch and S. A. Werner, *Neutron interferometry*, Clarendon Press, Oxford (2000).
- [Rowe et al., 2001] M. A. Rowe, D. Kielpinski, V. Meyer, C. A. Sackett, W. Itano, C. Monroe, and D. J. Wineland, *Experimental violation of a Bell's inequality with efficient detection*, Nature (London) **409**, 791 (2001).
- [Sakai et al., 2006] H. Sakai, T. Saito, T. Ikeda, K. Itoh, T. Kawabata, H. Kuboki, Y. Maeda, N. Matsui, C. Rangacharyulu, M. Sasano, Y. Satou, K. Sekiguchi, K. Suda, A. Tamii, T. Uesaka, and K. Yako, *Spin correlations of strongly interacting massive fermion pairs as a test of Bell's inequality*, Phys. Rev. Lett. **97**, 150405 (2006).
- [Sakurai, 1994] J.J. Sakurai, *Modern Quantum Mechanics*, Addison-Wesley, Reading, Massachusetts (1994), pp. 203.

- [Seevinck et al., 2008] M. Seevinck and J. Uffink, *Partial separability and entanglement criteria for multiqubit quantum states*, Phys. Rev. A **78**, 032101 (2008).
- [Simon et al., 2000] C. Simon, M. Żukowski, H. Weinfurter, and A. Zeilinger, *Feasible “Kochen-Specker” experiment with single particles*, Phys. Rev. Lett. **85**, 1783 (2000).
- [Sponar et al., 2008] S. Sponar, J. Klepp, R. Loidl, S. Filipp, G. Badurek, Y. Hasegawa, and H. Rauch, *Coherent energy manipulation in single-neutron interferometry*, Phys. Rev. A **78**, 061604(R) (2008).
- [Sponar et al., 2010a] S. Sponar, J. Klepp, C. Zeiner, G. Badurek, and Y. Hasegawa, *Violation of Bell-like Inequality for spin-energy entanglement in neutron polarimetry*, Phys. Lett. A **374**, 431 (2010); arXiv:quant-ph/09074654.
- [Sponar et al., 2010b] S. Sponar, J. Klepp, R. Loidl, S. Filipp, K. Durstberger-Rennhofer, R.A. Bertlmann, G. Badurek, Y. Hasegawa, and H. Rauch, *Geometric Phase in Entangled Systems: A Single-Neutron Interferometer Experiment*, Phys. Rev. A **81**, 042113 (2010); arXiv:quant-ph/09074909.
- [Sponar, 2011] S. Sponar, *Multi-Entanglement in Neutron Interferometric and Polarimetric Experiments*, Dissertation, Vienna University of Technology (2011).
- [Sponar et al., 2014] S. Sponar, T. Denkmayr, H. Geppert, H. Lemmel, A. Matzkin, and Y. Hasegawa, *General complex Spin Weak Values obtained in Matter-Wave Interferometer Experiments*, arXiv:1404.2125.
- [Suda, 2006] M. Suda, *Quantum Interferometry in Phase Space. Theory and Applications*, Springer-Verlag, Berlin Heidelberg, Germany (2006).
- [Sulyok et al., 2010] G. Sulyok, Y. Hasegawa, J. Klepp, H. Lemmel, and H. Rauch, *Noise-induced dephasing in neutron interferometry*, Phys. Rev. A **81**, 053609 (2010).
- [Summhammer et al., 1983] J. Summhammer, G. Badurek, H. Rauch, U. Kischko, and A. Zeilinger, *Direct observation of fermion spin superposition by neutron interferometry*, Phys. Rev. A **27**, 2523 (1983).
- [Tapster et al., 1994] P. R. Tapster, J. G. Rarity, and P. C. M. Owens, *Violation of Bell’s inequality over 4 km of optical fiber*, Phys. Rev. Lett. **73**, 1923 (1994).

- [Tittel et al., 1998] W. Tittel, J. Brendel, H. Zbinden, and N. Gisin, *Violation of Bell inequalities by photons more than 10 km apart*, Phys. Rev. Lett. **81**, 3563 (1998).
- [Uhlmann, 1976] A. Uhlmann, *The “Transition Probability” in the State Space of a *-Algebra*, Rep. Math. Phys. **9**, 273 (1976).
- [Uhlmann, 2000] A. Uhlmann, *Fidelity and concurrence of conjugated states*, Phys. Rev. A **62**, 032307 (2000); arXiv:quant-ph/9909060.
- [von Neumann, 1932] J. von Neumann, *Mathematische Grundlagen der Quantenmechanik*, Springer, Berlin (1932).
- [Walther et al., 2005] P. Walther, K. Resch, T. Rudolph, E. Schenck, H. Weinfurter, V. Vedral, M. Aspelmeyer, and A. Zeilinger, *Experimental one-way quantum computing*, Nature (London) **434**, 169 (2005).
- [Weihs et al., 1998] G. Weihs, T. Jennewein, C. Simon, H. Weinfurter, and A. Zeilinger, *Violation of Bell’s inequality under strict Einstein locality conditions*, Phys. Rev. Lett. **81**, 5039 (1998).
- [Williams, 1988] W. G. Williams, *Polarized Neutrons*, Clarendon Press, Oxford (1988).
- [Wocjan et al., 2005] P. Wocjan and M. Horodecki, *Characterization of combinatorially independent permutation separability criteria*, Open Syst. Inf. Dyn. **12**, 331 (2005).
- [Zehnder, 1891] L. Zehnder, *Ein neuer Interferenzrefraktor*, Zeitschrift für Instrumentenkunde **11**, 275 (1891).
- [Zeilinger, 1986] A. Zeilinger, *Testing Bell’s inequalities with periodic switching*, Phys. Lett. A **118**, 1 (1986).
- [Zhao et al., 2004] Z. Zhao, Y. Chen, A. Zhang, T. Yang, H. J. Briegel, and J. W. Pan, *Experimental demonstration of five-photon entanglement and open-destination teleportation*, Nature (London) **430**, 54 (2004).
- [Zych et al., 2011] M. Zych, F. Costa, I. Pikovski, Č. Brukner, *Quantum interferometric visibility as a witness of general relativistic proper time*, Nat. Commun. **2**, 505 (2011).

Curriculum Vitae

Name: Daniel Erdösi
Address: A-1190, Vienna , Probusgasse 5/3
E-Mail: danielerdosi@gmail.com

Date of birth: Dec. 28, 1977 in Nyíregyháza
Nationality: Hungarian
Marital status: unmarried, no children

Education

2009 – 2015 PhD-Studies, Vienna University of Technology, Atominstitut
PhD thesis: *Double and Triple Entanglement in a Single Neutron System*

1997 – 2007 University studies of technical physics, Vienna University of Technology
Main focus: methods and technologies
Diploma thesis (Department of solid-state Electronics): *Electrical and structural characterization of living cells on microstructured solid-state electrodes*

1993 – 1997 Realgymnasium Billroth, 1190 Wien

Employment history

2014 – to date Scientist at the Austrian Excellence Center for Tribology

2009 – 2013 Project assistant at the Atominstitut TU Vienna

2005 – 2009 Project assistant at the Department of solid-state Electronics TU Vienna

Scientific Publications

Unaffiliated:

- D. Erdösi, *Curvature of the Universe*, Physics Essays **17**(3), 390 (2004).
- D. Erdösi, *Energy Transfer Between Arbitrarily Moving Point Particles*, under peer review.

In team:

- D. Erdösi, M. Huber, B.C. Hiesmayr, Y. Hasegawa, *Proving the generation of genuine multipartite entanglement in a single-neutron interferometer experiment*, New Journal of Physics **15**, 023033 (2013).
- Y. Hasegawa and D. Erdösi, *Spin-path entanglement in single-neutron interferometer experiments*, AIP Conf. Proc. **1384**, 213-222 (2011).
- H. Wanzenböck, K. Dominizi, D. Erdösi, E. Bertagnolli, *Precision structured surfaces as functional carriers for in-vitro cultures of living cells*, euspen Conf. Proc. Vol. II, 377 (2006).

Language skills

German and Hungarian: native
English: good

Further skills

EDV-proficiency: LabView, LaTeX, HTML, CSS, MS-Office
Driver's license: B
Miscellaneous: National diploma in real estate trust (in Hungary, 2001)
Supernumerary at the Volksooper Wien (2002)
Private teaching in mathematics and descriptive geometry (2003 - 2005)

Vienna, February 2015